Probing the Strongly Correlated Quantum Materials with Advanced Scanning Tunneling Microscopy/Spectroscopy

by

He Zhao

A dissertation submitted in partial satisfaction of the
requirements for the degree of
Doctor of Philosophy
in Physics

Boston College
Morrissey College of Arts and Sciences
Graduate School

September 2020

Abstract

We used spectroscopic-imaging scanning tunneling microscopy (SI-STM) and spin-polarized STM (SP-STM) to unveil new electronic phenomena in several different quantum systems. We explored: (1) a potential topological superconductor heterostructure Bi_2Te_3/Fe(Te, Se), (2) high-T_c superconductors − $Bi_2Sr_2CaCu_2O_{8+x}$ and Fe(Te, Se), and (3) doped spin-orbit Mott insulators Sr_2IrO_4 and $Sr_3Ir_2O_7$. In Bi_2Te_3/Fe(Te, Se), we observed superconductivity (SC) on the surface of Bi_2Te_3 thin film, induced by the iron-based superconductor substrate. By annealing the optimally-doped cuprate superconductor $Bi_2Sr_2CaCu_2O_{8+x}$, we drastically lowered the surface hole doping concentration to detect a unidirectional charge stripe order, the first reported charge order on an insulating (defined by the spectral gap with zero conductance spanning the Fermi level) cuprates surface. In the high-T_c SC Fe(Te, Se) single crystal, we found local regions of electronic nematicity, characterized by C_2 quasiparticle interference (QPI) induced by Fermi surface anisotropy and inequivalent spectral weight of d_{yz} and d_{xz} orbitals near Fermi level. Interestingly, the nematic order is locally strongly anti-correlated with superconductivity. Finally, utilizing SP-STM, we observed a short-range antiferromagnetic (AF) order near the insulator-metal transition (IMT) in spin-orbital Mott insulators Sr_2IrO_4 and $Sr_3Ir_2O_7$. The AF order inhomogeneity is found not to be strongly correlated with the charge gap. Interestingly, the AF order in the bi-layered $Sr_3Ir_2O_7$ shows residual memory behavior with temperature cycling. Overall, our work revealed new phenomena in a range of today's most intriguing materials, and set the stage for using SP-STM in other complex oxides.

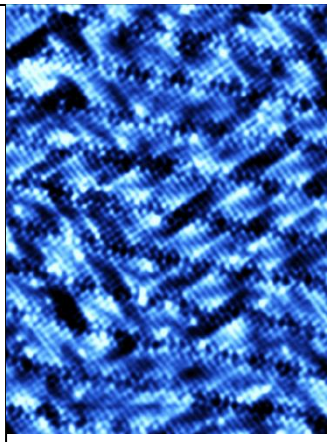

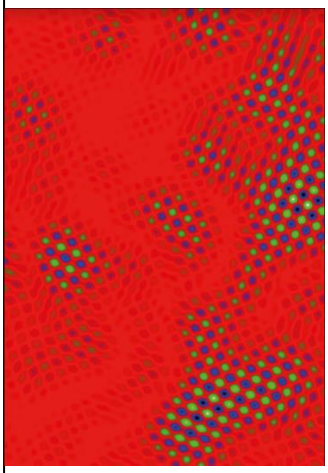

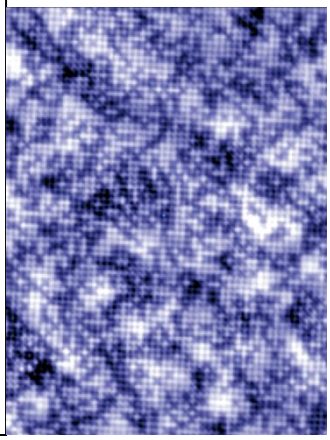

To my family

Contents

1 INTRODUCTION

1.1 SUPERCONDUCTING PROXIMITY EFFECT (SPE)

When a superconductor is contacted with a normal metal material, one can be able to detect the induced superconductivity behavior on the metal material which is due to the leakout of Cooper pairs from the superconductor into the metal. Such a phenomenon, called superconducting proximity effect (SPE), was discovered around the 1960s[1]. As **Figure 1. 1. 1** illustrates, the superconducting pairing potential Δ equals Δ_0, which is the potential of the bulk far away from the S/N interface, and vanishes on the normal metal side. The proximity effect clearly shows up near the interface, though the Δ is weakened crossing from the superconductor to the normal metal.

With the proposals that topological insulator/S-wave superconductor heterostructure theoretically can form a topological superconductor (TSC)[2] coming out in 2008, the interest in SPE has been reignited, attracting significant attention due to that it's building a platform to engineer Majorana-based qubit for topological quantum computation.

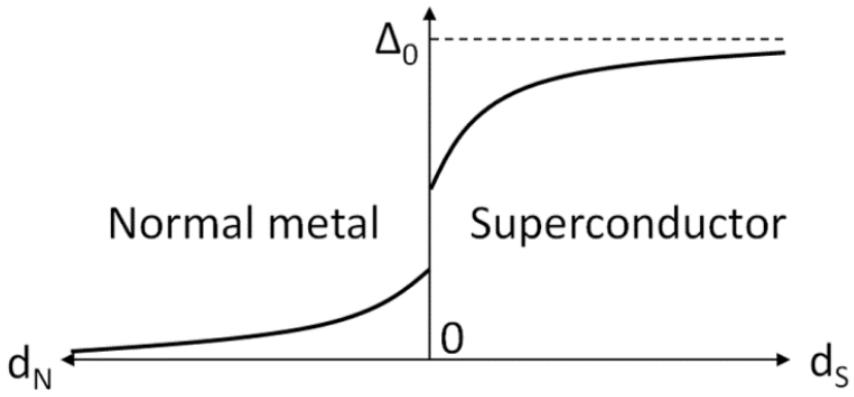

Figure 1. 1. 1 Evolution of the pairing potential Δ from bulk superconductor to the contacted normal metal through the S/N interface.

1.2 CU-BASED HIGH-T_C SUPERCONDUCTOR

The Cu-based high high-T_c superconductor is one of the biggest families in the unconventional superconductors. Since their common constituents are the copper oxide planes within the layer structure so they are also called 'Cuprate'. These Cu-O planes always interact between two inert ionic layers so that they can provide electron or hole carriers to dope the Cu-O planes. Each Cu-O plaquette contains two O atoms and one Cu atom. And each Cu contributes a singly occupied $3d_{x2-y2}$ orbital. The O atom along x/y direction contributes a doubly occupied $2p_x$ or $2p_y$ orbitals, respectively, as shown in **Figure. 1. 2. 1**.

Due to the large on-site repulsion coulomb interaction energy cost (7~10eV)[3] for a typical $3d_{x^2-y^2}$ orbital, the electron hopping from one Cu site to a neighbor site will be prohibited such that we will get a so-called 'Mott Hubbard' insulator as shown in **Figure. 1. 2. 2.** However, Cuprate is not the 'Mott Hubbard' case, instead, the electrons hopping is from Oxygen 2p orbital to Cu site 3d orbital, and the energy cost during this process is

smaller than the Coulomb interaction in the 'Mott Hubbard' scenario, which is called 'Charge transfer' insulator as demonstrated in **Figure. 1. 2. 2.** Almost one order of magnitude is smaller than the Coulomb interaction, the so-called 'charge transfer gap' scales around ~ 0.5eV[4].

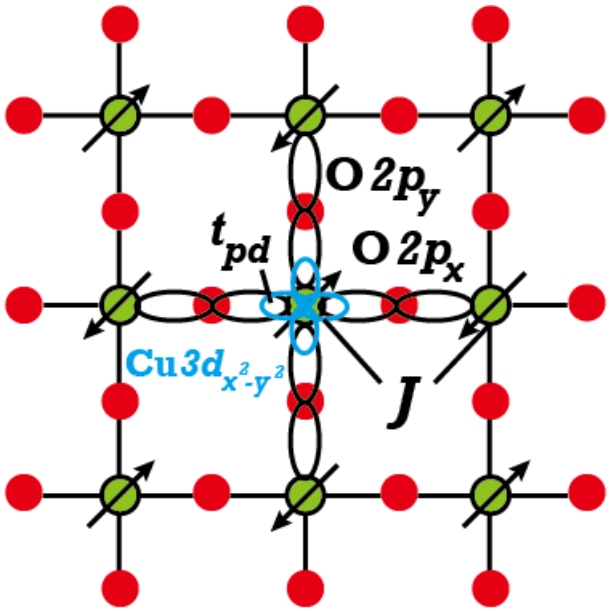

Figure. 1. 2. 1. The Cu-O plane from the top view. The arrows represent the antiferromagnetic order on the plane.

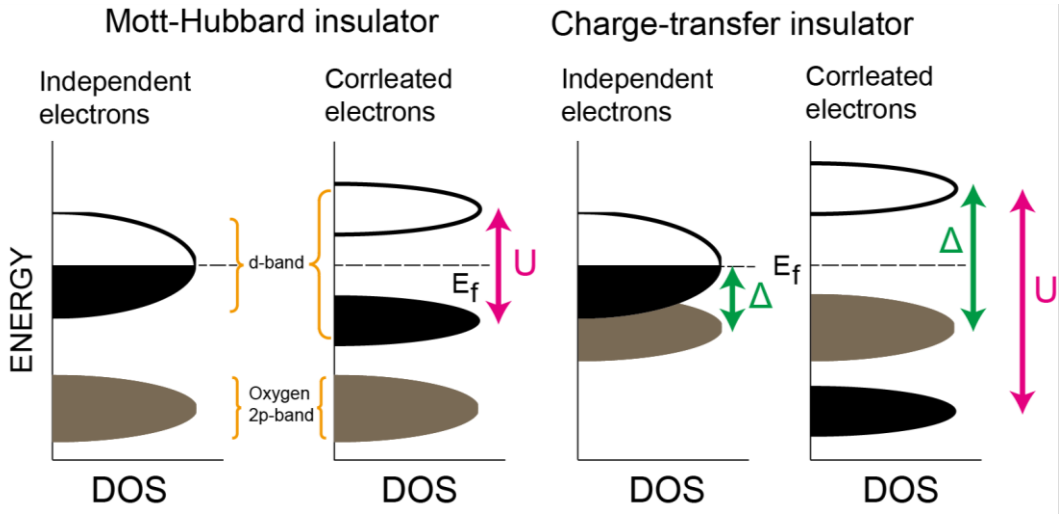

Figure. 1. 2. 2. Schematics of band structures for different types of insulators. U represents the repulsion coulomb interaction energy, Δ is the charge transfer gap between the oxygen band and copper band.

1.2.1 The phase diagram of Cuprate

As we have introduced that the parent phase of cuprate is a Mott insulator, which is always accompanied by antiferromagnetic (AF) order, doping electrons or holes can induce various phases other than the AF-insulator (AFI) phases-superconducting (SC) phase and pseudogap phase (PG). SC phase has been studied mostly since the first time when people observed superconductivity in cuprates. For example, SC can be measured in $Bi_2Sr_2CaCu_2O_{8+x}$ when hole doping x is approximately 0.6 to 0.25, and the T_c can reach ~91k at optimal doping level at x~0.16. Both ARPES[5] and STM[6] showed that cuprates have an anisotropic d-wave SC gap instead of isotropic s-wave. Besides the attractive SC phase, substantial measurements showed the existence of a pseudogap (PG) phase, which can open a gap on the fermi surface even when $T_c<T<T^*$ and people tried to explain the single-value gap at every momentum around the Fermi surface that always

persists at antinode region accompanied with a gapless Fermi arc around the SC nodes[7]. This PG phase can even coexist partially with the SC phase, and the relation between SC and PG is still under debate. Though both the SC gap and PG can show anisotropic performance spatially, lots of experimental evidence showed that SC and PG are possibly competing. From the phase diagram in **Figure. 1. 2. *3***, we can see that the PG size increases while the SC gap and T_c increase with doping level decreasing when it's below the optimal level.

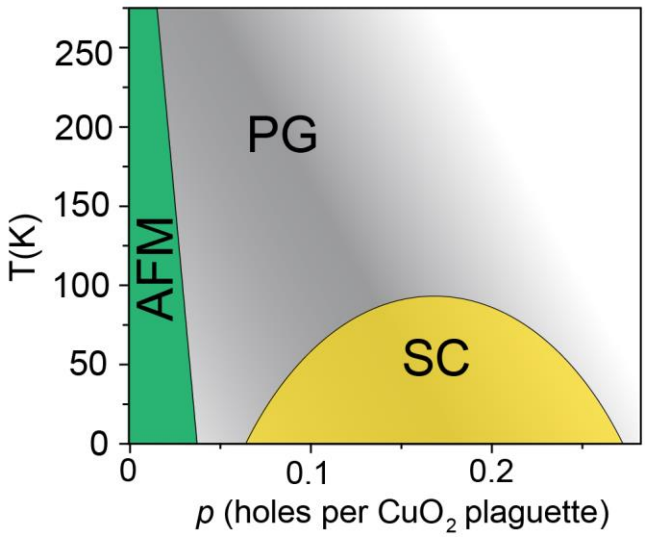

Figure. 1. 2. 3. The phase diagram of a typical hole-doped Cuprates.

1.2.2 Unconventional charge order in Cuprate

Charge order is a common phenomenon found in all types of cuprates, which is considered as an intrinsic property of the Cu-O plane. In 1995, charge order and spin order were first observed on $La_{1.48}Nd_{0.4}Sr_{0.12}CuO_4$ (LNSCO) by Tranquada et al.[8] with neutron scattering at Q_{co}=(0, 2 ± 0.25, 0) and Q_{so} = (0.5, 0.5±0.125, 0), respectively. Another interesting thing caught by the experimentalist is that the max intensity of the

charge order stripe always happened at doping x~1/8, which provides some support that the order should have some relation with superconductivity. In real space with atomic resolution, the first time STM detected the charge order along Cu-O direction was 7 years later since the La-based cuprates. Hoffman et al.[9] observed the 2D short-range charge density wave within vortices after applying the magnetic field on the top of $Bi_2Sr_2CaCu_2O_{8+\delta}$(Bi-2212), which is a layered cuprate with BiO-SrO-CuO_2-Ca-CuO_2-SrO-BiO crystallographic planes. Within the vortices, superconducting weight suppressed strongly, so the appearance of charge order further provides evidence that the superconductivity competes with charge order, in analogy to La-cuprates[10]. Discovery of quasiparticle interference (QPI) by Jenny Hoffman. et al.[11] intrigues further understanding and study of the charge order in cuprates. Hanaguri et al.[12] observed the 2D CDW, the so-called 'checkerboard', in Ca-based $Ca_{2-x}Na_xCuO_2Cl_2$(CCOC) doped by Na as shown in **Figure. 1. 2. 5**. As **Figure. 1. 2. 4(c)** shows, Hanaguri et al.[12], Vershinin et al.[13] and Wise et al.[14] found the periodicity of this type of short-range charge order is independent over biases when the cuprates (Vershinin et al. studied Bi-2212, Wise et al. measured Bi-2201) are in non-superconducting phase, i.e. T is higher than T_c. Wise et al. found the wavevector of the checkerboard can match the scattered DOS very well around the antinode region measured by ARPES[15]. And the Fermi surface nesting varies with the doping level, so do the checkerboard peak positions in the q-space. This was also supported by da Silva Neto et al.[16] STM study on Bi-2212.

The Y-based cuprates- $YBa_2Cu_3O_{6+x}$ can also observe the charge order. Leyraud et al.[17] found the hint of charge order which appeared as by the use of quantum oscillation. They

saw a low-frequency oscillation which might be due to the small electron pocket on the fermi surface of the specific $YBa_2Cu_3O_{6+x}$.

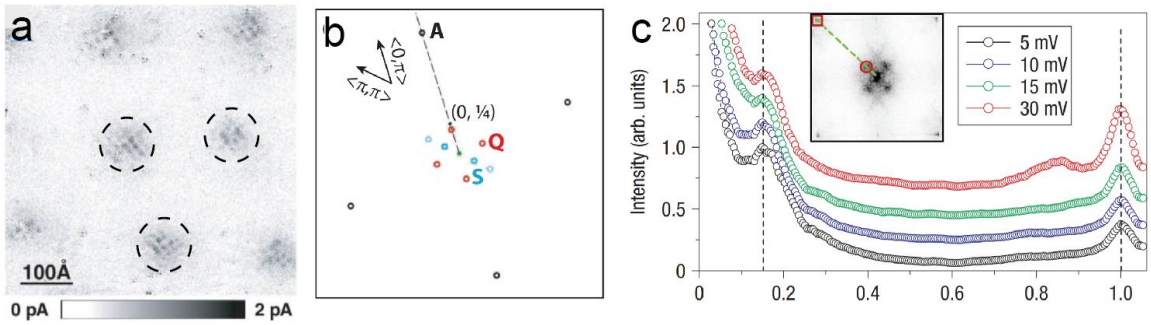

Figure. 1. 2. 4. The charge order observed in and out of the magnetic field. (a) dI/dV map on Bi-2212 showing 2D short-range charge order in vortices. Dashed circles indicate the vortices region in real space. (b) Schematic of Fourier transformed (FT) image of (a). The (0,1/4) red circled where the charge order sits and one will see a 4a0 modulation in real space. (c)The linecuts along center to brag peaks in FT of dI/dV images, as shown in the inset, at different biases detected without B on top of Bi-2201. The red squared the Brag peaks. (a) is adapted from Ref. 9 and (b) is adapted from Ref. 14.

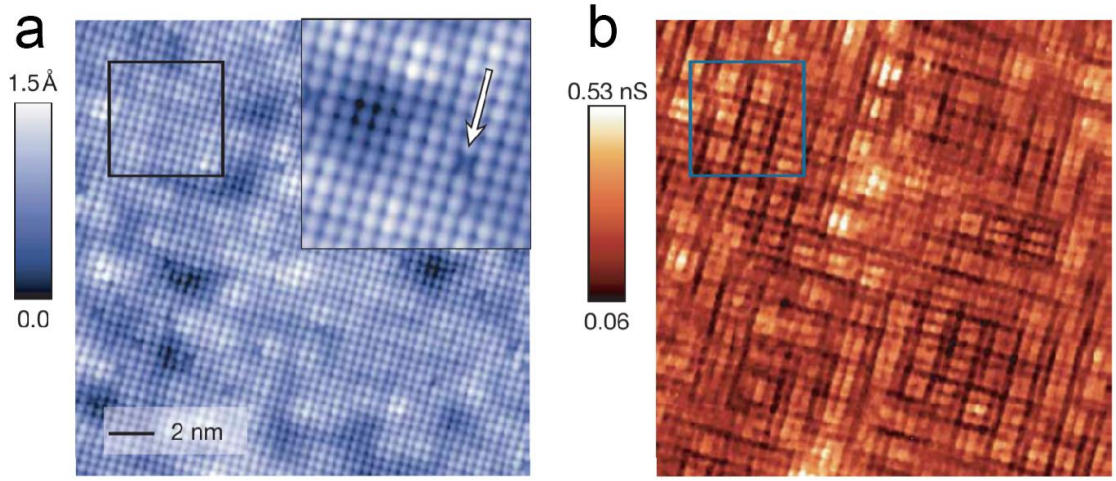

Figure. 1. 2. 5. 2D checkerboard on CCOC. (a) Typical topograph of CCOC. Inset is the zoom-in of the square area. (b) *dI/dV* in the same region as (a). Blue squared the same atomic inset area of (a). Those ~4a0 modulation is the checkerboard charge order. Reprinted from Ref. 18.

1.3 IRON-BASED SUPERCONDUCTOR

In 2008, Kamihara et al. observed superconductivity in La[$O_{1-x}F_x$]FeAs with the highest T_c = 26K, representing the iron-based superconductor era begins. Soon after that, the Tc was raised above 40K within the same material but by substituting different elements. The highest T_c in the bulk iron-based SC is around 55K in SmO_{1-x} F_xFeAs discovered by Ren et al. As shown in **Figure. 1. 3. 1**, there are four classes of iron-based SC have been investigated a lot, which classified by the crystalline features[19]:11 (i.e. iron-chalcogenides, simply FeSe including vacancy, sulfur, tellurium, and oxygen doping), 111 (mainly AFeAs, A=Li, and Na), 122 (mainly $AeFe_2As_2$ and $A_xFe_{2-y}Se_2$, the only single layer of separating space atoms between Fe_2As_2, Ae=Ca, Sr, Ba, Eu, K, etc, A=K, Rb, Cs, TI/K, and TI/Rb)[20] and 1111(mainly AeFFeAs, Ae=Ca, Sr and Ba, and LnFeAsO system, Ln= La, Nd, Sm, Gd). Recently, the superconductivity observed in single layer FeSe/SrTiO3 [21] has surpassed the bulk material. Jianfen Ge et al.[22] even observed T_c above 100K in the monolayer FeSe/$SrTiO_3$.

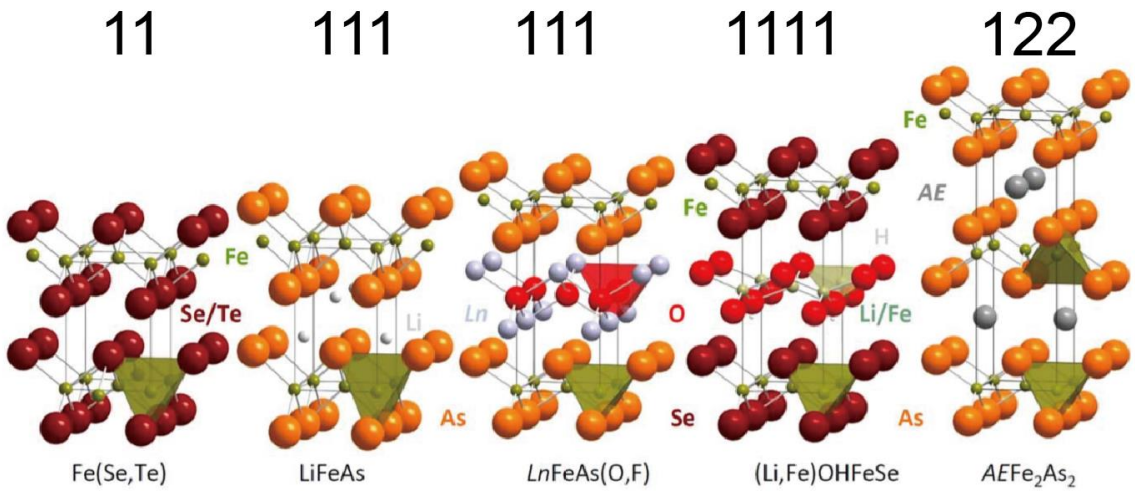

Figure. 1. 3. 1. Schematic crystal structures of the four Fe-based superconductor classes. It's adapted from Ref. 23.

Iron-based superconductivity shares enormous similarities with Cuprates: both of them are nonconventional superconductors in the way that phonon cannot be able to explain the SC mechanism and both of them are quasi-2D SC approximate to the antiferromagnetism (AF)[20] as shown in **Figure. 1. 3. 2**. However, there are also differences between the two: parent Fe-based SC is in the AF semimetallic phase while parent Cu-based SC is AF Mott insulator (AFI)[24] due to the strong on-site Coulomb interaction, cuprates electronic properties can be described by single band[25] crossing fermi level while Fe-based should have 3 orbitals got involved and the pairing symmetry of the two types of high T_c SC are also no the same, Cu-based SC is d-wave while Fe-based SC pairing symmetry is still under debate, though lots of experimental results could be explained by $S_{\pm}$-wave, as shown in **Figure. 1. 3. 3**[26, 27, 28, 29, 30].

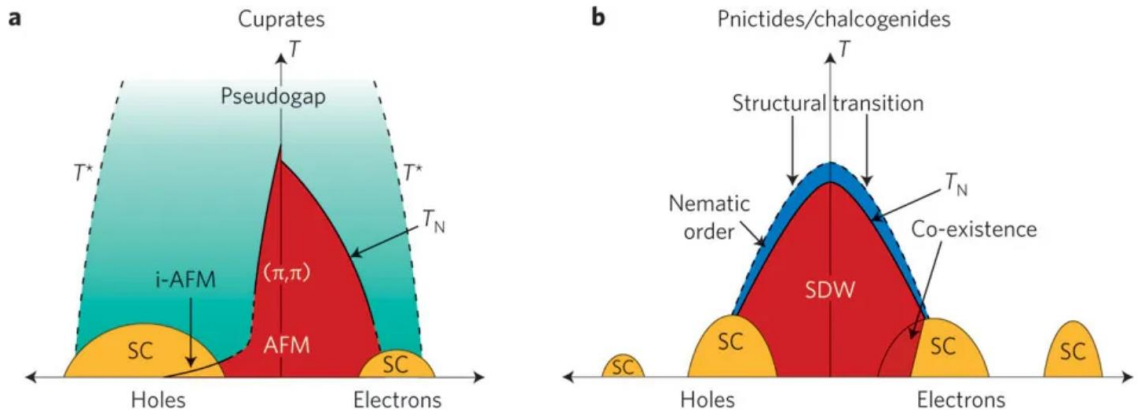

Figure. 1. 3. 2. Phase diagrams of Cu-based SC and Fe-based SC. (a) is for cuprates, (b) is iron-based SC. Reprinted from ref. 31.

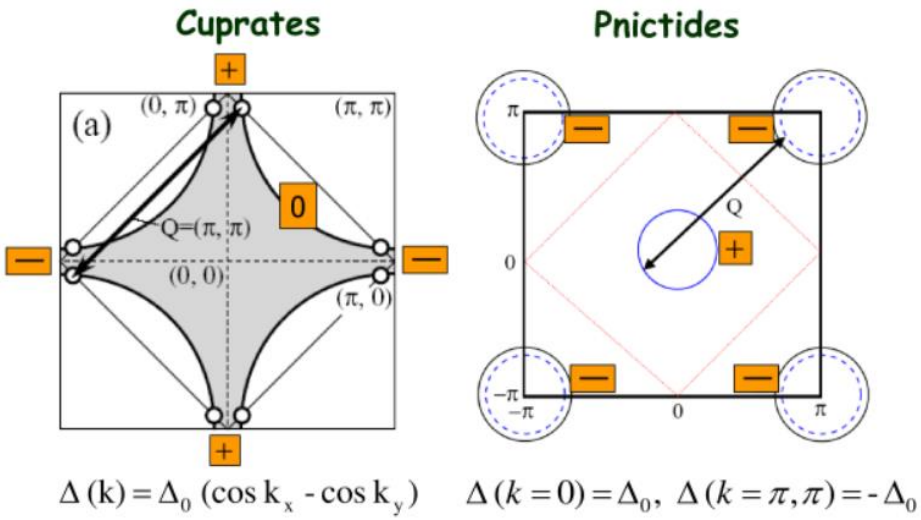

Figure. 1. 3. 3. The comparison of the pairing state from spin-fluctuation exchange in cuprate SCs and in FeSCs. Reprinted from ref. 32.

1.4 RUDDLESDEN-POPPER IRIDATES: $Sr_{N+1}Ir_NO_{3N+1}$(N=1, 2, AND ∞)

Over the past few years, the Ruddlesden-Popper Iridates, one of the 5d transition metal oxides (TMD) families, have attracted the interests of people and especially $Sr_{n+1}Ir_nO_{3n+1}$(n=1, 2, and ∞)(**Figure. 1. 4. 1**), within which the physics phenomena analogy to cuprates have been found especially when n=1[33, 34, 35, 36]. Electronic physics of cuprates high T_c SC can be well described by single-band spin-1/2 Heisenberg AF on a 2D lattice, with strong exchange coupling. To our best knowledge, iridate is the first material outside this family that can realize the condition[37].

Identifying the hierarchy of energy scales associated with multiple interacting degrees of freedom is the starting point for understanding the TMD. As we have mentioned in the cuprates section above, the cuprates are 3d oxides and the onsite electron-electron

Coulomb repulsion (U) is quite dominant so that cuprate is a strongly correlated system with very localized orbitals. When the band width (W) is way smaller than U, we will obtain a Mott insulator due to the suppressed charge motion by strong U. In the opposite situation ($W>U$), we will see an insulator-metal transition (MIT) and get a metal. What if we have a 4d system? 4d orbital is more extended than 3d and there will be a higher overlap between 4d orbital and neighboring Oxygen 2p orbital. The charge mobility between atoms increases then we could expect that the on-site Coulomb interaction weakens hugely than the cuprate case. Further down the periodic table, the 5d orbital TMDs have even more extended orbital than 4d. Hence, the Coulomb interaction will be more insignificant and the charge is more nonlocalized. The larger overlap between orbitals will induce a wider band. It would be directly predicted that the 5*d* system will be more metallic. However, experimental results showed that it's not that case. Though the interactions energy scales we considered change a lot with atom becoming larger, there is another intermediate interaction joining the competition. As the charge on the nucleus (Z) increases, the spin-orbital coupling (λ_{SO}) also grows because $\lambda_{SO} \sim Z^4$, and the spin and orbital degree of freedom will get entangled. Now that λ_{SO} (0.1~1eV) energy scale is comparable with U (~0.6eV) (in cuprates, λ_{SO} is three orders smaller than U), we should take λ_{SO} into account. Due to this strong interaction competing with crystal field and electron hopping, a new kind of insulator from the conventional one appears in iridates. For example, in another section of this thesis, we will talk about a material from R-P iridates family: Sr_2IrO_4. In Sr_2IrO_4, λ_{SO} splits the t_{2g} band into $J_{eff=3/2}$ and $J_{eff=1/2}$, the fermi level resides in the latter band. Coulomb interaction will further split the narrow half-filled $J_{eff=1/2}$ band to open an insulating gap. This will cause a novel Mott insulating which

relies on the strong spin-orbit coupling and of course the magnetism also changes because of that. Another very interesting thing in iridates, maybe the most attractive part in the very beginning, is that SC could in principle exist after electron doping in analogy to the hole-doped cuprates La_2CuO_4 because they share too many similarities: crystal structure, electronic structure, and magnetic coupling constants.

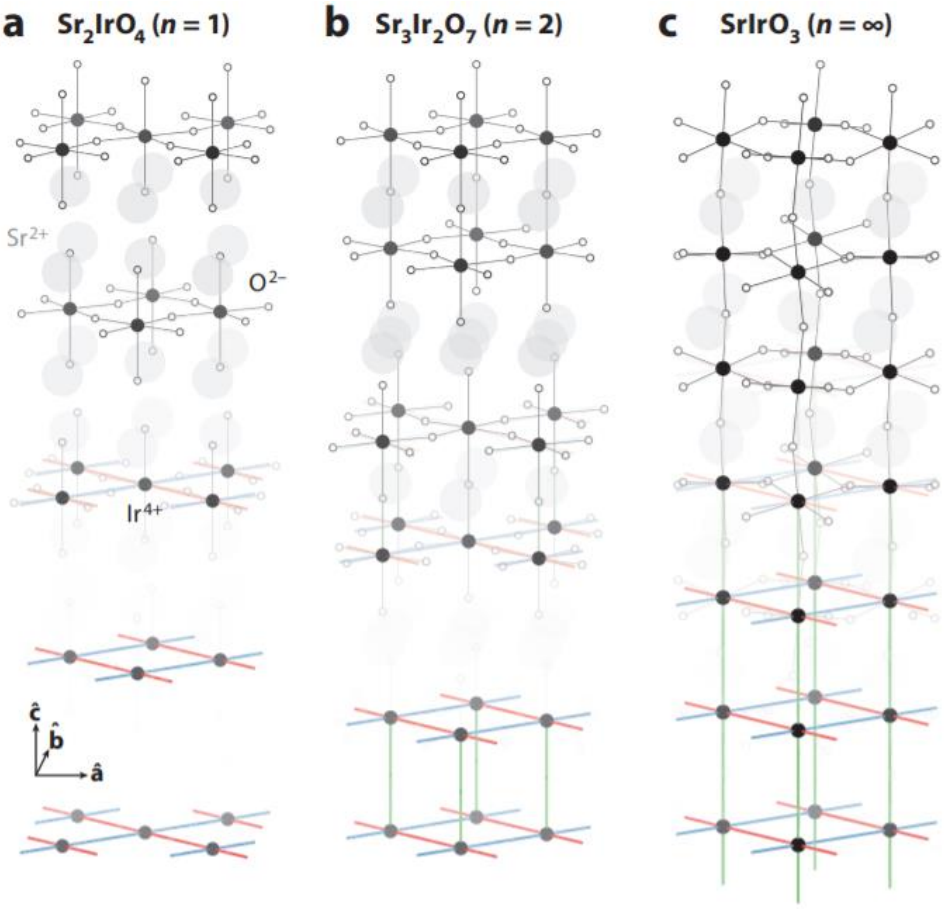

Figure. 1. 4. 1. Crystal structure of the Ruddlesden-Popper series $Sr_{n+1}Ir_nO_{3n+1}$(n=1, 2, and ∞). Reprinted from ref. 38.

1.5 STRUCTURE OF THE THESIS

In this thesis, I will discuss the physics properties of some representative materials from different families: Cuprates high T_c SC, Fe-based high T_c SC, Ruddlesden-Popper iridates $Sr_{n+1}Ir_nO_{3n+1}$(n=1, 2, and ∞), and SC proximity effect. As a result of the doping tuned electron correlation, these compounds exhibit quite exciting properties. Especially when doping approximates to MIT, the new phenomena we detected with a new technique developed, may help us understand the SC mechanism inside those complicated strongly correlated systems.

This thesis includes 7 chapters, a brief introduction to SC proximity effect, cuprates high T_c SC, Fe-based high T_c SC, and Ruddlesden-Popper iridates $Sr_{n+1}Ir_nO_{3n+1}$(n=1, 2, and ∞) are given in chapter 1. An introduction to the experimental technique-Scanning Tunneling Microscope/Spectroscopy (STM/S), including a new method based on which we developed, the Spin-Polarized STM (SP-STM), is demonstrated in chapter 2. Chapter 3 will present the SC proximity effect we observed on the surface of thin-film heterostructure Bi_2Te_3/Fe(Te, Se) grown by our home-built Molecular Beam Epitaxy (MBE), we observe a thickness-dependent gapped topological surface state due to the superconductivity leaked from high T_c SC substrate Fe(Te, Se). Chapter 4 will focus on the vacuum annealing induced dopants deduction of optimally doped T_c ~ 91K Bi-2212 which 'pushes' this cuprate into an AF insulator phase, and within this phase, a phenomenon called charge stripe predicted two decades ago is detected. In chapter 5 we will show our SP-STM experimental results about $(La_xSr_{1-x})_2IrO_4$ at different doping levels and found that the AF order starts melting near the MIT and there is no strong

correlation between AF and the local charge gap which indicates that the charge gap might result from a hidden order. Chapter 6 will present the ongoing project about bi-layered $(La_xSr_{1-x})_3(Ir_{1-y}Ru_y)_2O_7$, the cousin of single-layered Sr_2IrO_4(chapter 5). Utilizing SP-STM to investigate the AF order evolution with La and Ru doping, we found that the long-range AF order melts near IMT upon electron doping, which is consistent with the observation on Sr_2IrO_4(chapter 5), and interestingly, the morphology of such granular magnetic texture is robust to the thermal erasure. The last chapter (chapter 7) will present the short-range nematic criticality fluctuation due to the local strain near the quantum critical point in an iron-based SC, $FeTe_{0.55}Se_{0.45}$, and such short-range nematicity caused a strong suppression of local SC.

2 (SPIN-POLARIZED) SCANNING TUNNELING MICROSCOPY/SPECTROSCOPY

2.1 SPECTROSCOPIC IMAGING-SCANNING TUNNELING MICROSCOPY

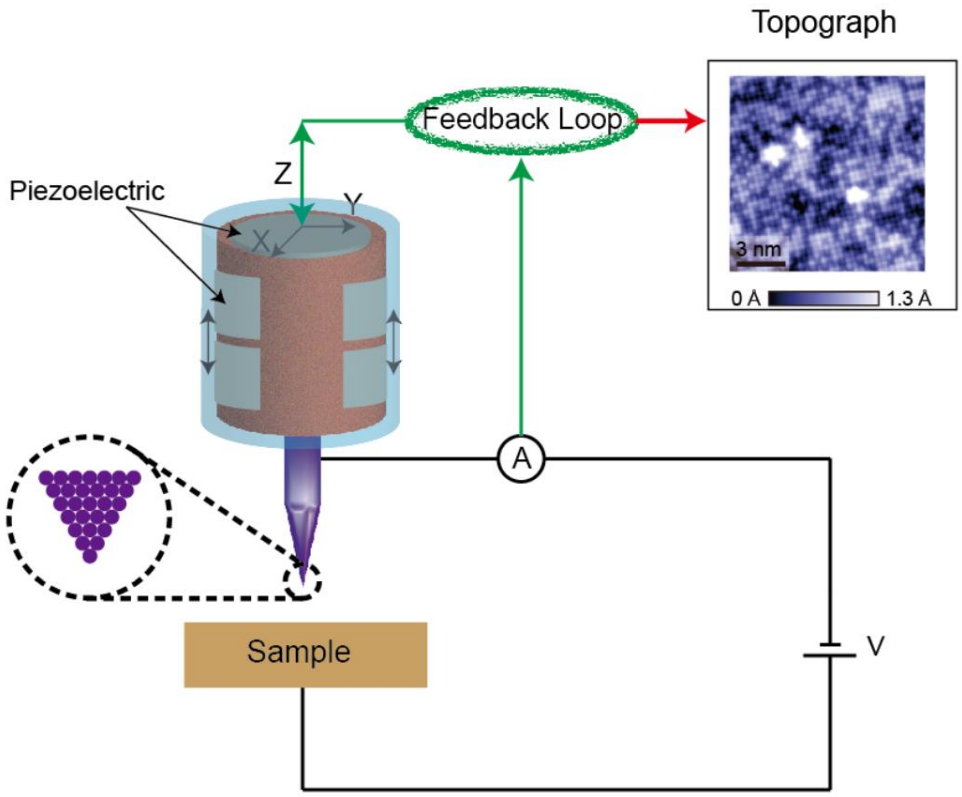

Figure. 2. 1. 1. Schematic representation of STM. A voltage is applied between tip and sample. The tip rasters across the sample surface in the X/Y direction and the height change along Z will be tuned by the piezoelectric scanner through a feedback loop. The 3D signal output will be recorded as a topograph.

Scanning tunneling microscopy (STM) was invented by Binnig and Rohrerin[39], and they shared the Nobel prize in 1982 for their contribution to physics. STM is mainly used to measure the local density of states (LDOS) of a solid. It's composed of the atomic sharp tip and the sample of interest and between the two is around a few Å thick vacuum space acting as a quantum barrier as shown in **Figure. 2. 1. 1**. The tip holder sits on a piezoelectric scanner so that the tip can move as small as pm per step along either parallel to the sample surface or vertical. Electrons can tunnel from either sample-to-tip or tip-to-sample through the quantum barrier after applying a voltage between tip and sample. The tip height is controlled by a feedback circuit if we are at constant current mode, the tip-sample separation will be smaller if we have lower conductance and vice versa. Generally, the current tunneling through the junction can be calculated by time-dependent perturbation theory. As shown in **Figure. 2. 1. 2**, when there is no bias applied between tip and sample, they two have the same fermi energy, but if a -*V* is applied to the sample, the tip's fermi level has a relative *eV* shifting down from the sample's fermi energy and the electron from occupied states of the sample will tunnel to the unoccupied states of tip elastically. The current of electrons tunneling from the occupied sample to tip is:

$$I_{sample->tip} = 2e\cdot\frac{2\pi}{\hbar}|M|^2\left(\rho_s(\varepsilon)\cdot f(\varepsilon)\right)\cdot(\rho_t(\varepsilon+eV)\cdot[1-f(\varepsilon+eV)]) \qquad (2.1.)$$

Where factor 2 is for two types of spin, up and down, $\frac{2\pi}{\hbar}$is from time-dependent perturbation, $|M|^2$is the tunneling matrix element, $\rho_{s(t)}(\varepsilon)$ is the DOS of the sample (tip) and $f(\varepsilon)$ is the Fermi distribution function:

$$f(\varepsilon) = \frac{1}{1+e^{\varepsilon/k_BT}} \qquad (2.2.)$$

There is still smaller current tunneling from tip to sample:

$$I_{tip->sample} = -2e\cdot\frac{2\pi}{\hbar}|M|^2(\rho_t(\varepsilon+eV)\cdot f(\varepsilon+eV))\cdot(\rho_s(\varepsilon)\cdot[1-f(\varepsilon)]) \qquad (2.3.)$$

If we sum them two up, we will get the total current tunneling from sample to tip after integrating of all energies ε:

$$I = -\frac{4e\pi}{\hbar}|M|^2\left(\int_{E_F}^{E_F+eV}\rho_s(\varepsilon)\rho_t(\varepsilon+eV)\{f(\varepsilon)[1-f(\varepsilon+eV)]-[1-f(\varepsilon)]f(\varepsilon+eV)\}d\varepsilon\right.$$

$$(2.4.)$$

We can approximately get $f(\varepsilon)\sim 1$ because of the thermal broadening at T=4K (the working temperature of our STM), then the total current tunneled through the junction is:

$$I = -\frac{4e\pi}{\hbar}|M|^2\left(\int_{E_F}^{E_F+eV}\rho_s(\varepsilon)\rho_t(\varepsilon+eV)d\varepsilon\right) \qquad (2.5.)$$

As our tip is always made of some single element metal or metallic compound so that the tip's DOS is almost a constant with energy, therefore we could further simplify the equation (2. 5.) to:

$$I = -\frac{4e\pi}{\hbar}|M|^2\rho_t(0)\left(\int_{E_F}^{E_F+eV}\rho_s(\varepsilon)d\varepsilon\right) \qquad (2.6.)$$

Our spin averaged STM experiments are performed with W tip, which has been sharpened to be atomic sharp on top of the Au surface before use, and this material has a relatively flat DOS at a low range of bias ~ +/- 200mV. We could easily check this assumption by taking spectra at different locations because Au has a flat DOS.

The tunneling matrix $|M|^2$can be estimated by using WKB approximation if we regard the vacuum barrier as a simple square barrier. WKB gives the tunneling probability through a square barrier as $|M|^2 = e^{-2\gamma}$, the γ can be given by:

$$\gamma = \int_0^s \frac{\sqrt{2m\varphi}}{\hbar} dx = \frac{s}{\hbar}\sqrt{2m\varphi} \qquad (2.7.)$$

s is the width of the barrier, m is the mass of the electron, φ is the height of the barrier, which is a mixture of the work function of tip and sample.

Combining the equation (2. 6.) and (2. 7.) can get the total current tunneled is:

$$I = -\frac{4e\pi}{\hbar}\rho_t(0)e^{-2\frac{s}{\hbar}\sqrt{2m\varphi}}\left(\int_{E_F}^{E_F+eV}\rho_s(\varepsilon)d\varepsilon\right) \qquad (2.8.)$$

In summary, the tunneling current is proportional to the integral of the sample's DOS from the Fermi level to the bias we applied.

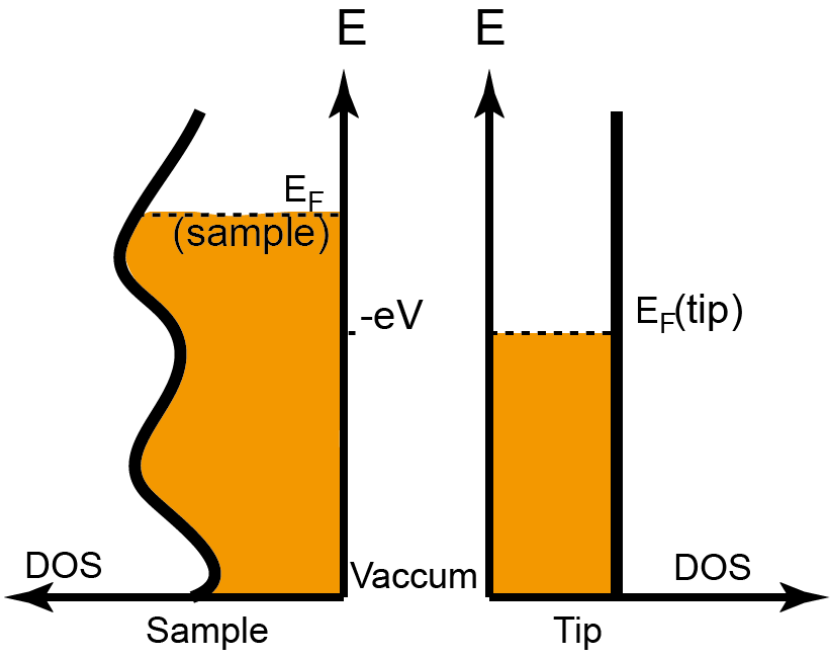

Figure. 2. 1. 2. Schematic of the sample and tip density-of-states at bias V_B.

2.2 TYPES OF MEASUREMENT

2.2.1 Topograph

Topograph is probably the most commonly seen data taken by STM. It can be acquired by recording the tip height change when tip rasters across the sample surface. The tip height is controlled by applying a voltage between STM and tip and keeping a constant tunneling current set for the feedback loop during tip scanning.

As the topograph measured by STM is a direct tip height response to tunneled current at different surface locations, so it may not be able to reflect the real sample surface structure. Suppose the tunneling matrix $M(r)$ is uniform over the topograph area, and the integrated DOS from fermi energy to the voltage applied V is uniform as well, then the output topograph is probably a real surface structure characterization.

As shown in **Figure 2. 2. 1**, the topograph of Fe(Te, Se) can see only the topmost layer Te(Se) composed square lattice. Te (bright) and Se (dark) site color differences are due to the contrast of local DOS integral between Te and Se.

2.2.2 *dI/dV* Spectrum

As mentioned before, the differential conductance $dI(r, z, V)/dV$ at bias voltage V is proportional to DOS. Thus by holding the tip at a constant separation from the sample surface and recording the $dI(r, z, V)/dV$ during sweeping the bias we can obtain a spectrum as dI/dV vs V. We can simply record the current and do the numerical derivative

to the *I* as well. However, the spectrum obtained with small AC voltage modulation from the lock-in amplifier method can provide higher signal-to-noise data, because we can always decompose the current as follows:

Let $V(t)=V_0 + V_m\cos(\omega t + \varphi)$, then

$$I(r, z, V(t))= I(r, z, V_0)+\frac{dI(r,z,V)}{dV}_{V=V_0} V_m cos(\omega t+\varphi)+ \frac{d^2I(r,z,V)}{dV^2}_{V=V_0} {V_m}^2 \cos^2(\omega t+\varphi)+\dots , \quad (2.9.)$$

The conductance is just the first harmonic.

For a positive bias, we have electrons tunneling from tip to sample and vice versa. Hence we can obtain the electronic property of both occupied and unoccupied bands of the sample, which is one of the main advantages over other DOS measurement techniques, like photoemission spectroscope because it can only characterize the occupied bands. Though the most recent development of inverse photoemission can help overcome the limitation, the unoccupied band DOS measurement sacrifices the resolution, and the setup is pretty complicated. A typical *dI/dV* spectrum is as shown in **Figure 2. 2. 1**.

2.2.3 *dI/dV* Mapping

As we have introduced previously that STM can map the surface structural information, which is directly measured as integral of DOS from fermi energy to bias we applied, and apart from that, STM can also obtain the DOS information simultaneously. There are two ways to measure the DOS, one is raster the tip across the surface with feedback and lock-

in on and repeats the scanning over the same area at another bias/setting, another takes single spot *dI/dV* spectrum and then moving tip to the next spot with a feedback loop on but with lock-in off to get rid of tip oscillation. Keeping the feedback loop on is to protect the tip from crashing during tip moving in both cases. We should note that the setup conditions are different for these two methods. One of the typical *dI/dV* maps is shown in **Figure 2. 2. 1**.

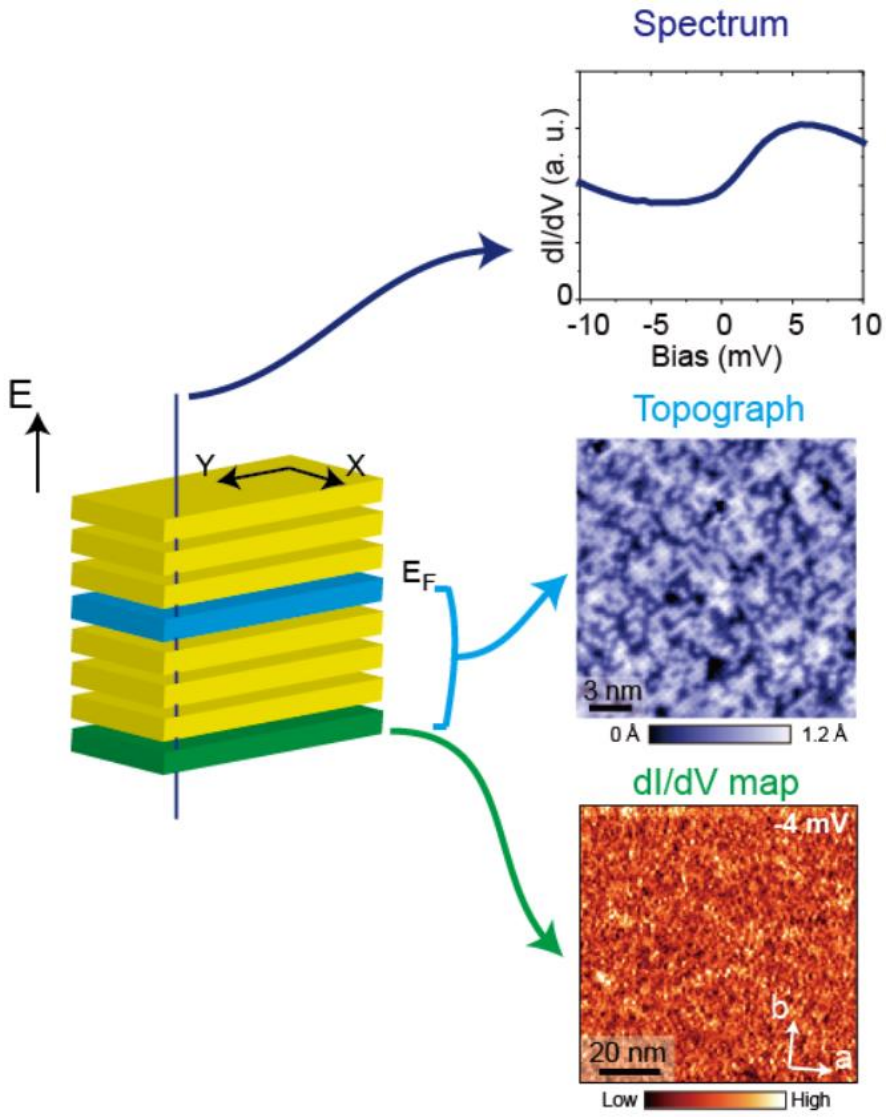

Figure 2. 2. 1. Three different data types measured by STM.

2.3 SPIN-POLARIZED SCANNING TUNNELING MICROSCOPY (SP-STM)

One main difference between the Spin-polarized STM (SP-STM) and non-polarized STM lies in the material of the tip. The tip of SP-STM is always spin-polarized while non-polarized STM cannot resolve the spin signal. Therefore, the SP-STM operation principle is based on the difference of DOS near Fermi energy for electrons of different spin characters. Due to the quantum exchange interaction, the DOS splits into two states based on the polarization, one is the majority another is the minority. These two states will shift rigidly against each other in the band model of ferromagnetism as shown in **Figure 2. 3. 1**. The imbalance causes a spin polarization, in contrast to paramagnetism that spin up and down DOS are identical at the same energy. The splitting of the DOS has immediate consequences on the current tunneled between two electrodes, the magnitude is influenced by the orientation of the two electrodes and this is called the tunneling magnetoresistance (TMR) effect.

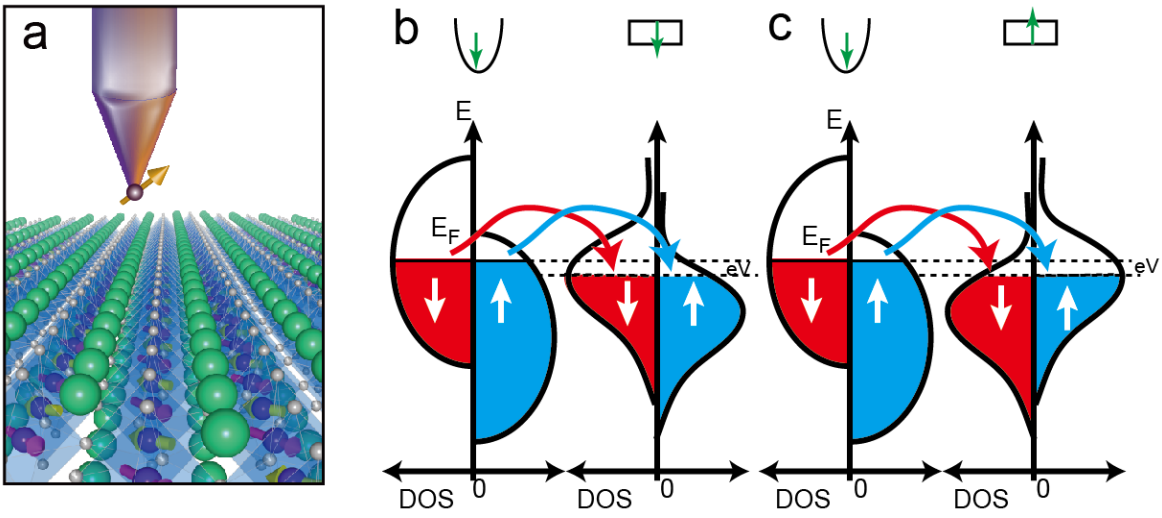

Figure 2. 3. 1. Schematic of SP-STM measurement. (a) The arrow at the apex of the tip denotes the spin polarization of the tip. (b) and (c) simplified picture of pin-polarized tunneling within a hypothetical spin-splitting DOS model in the parallel and antiparallel magnetization scenarios, respectively.

Considering the TMR effect, the parallel and antiparallel magnetization scenarios of tip/sample will allow quite a different magnitude of tunneling current. To make the picture simple, let's suppose that the spin orientation of the electron will not flip after tunneling between electrodes and the tip and sample have similar spin-splitting DOS as shown in **Figure 2. 3. 1**. For the scenario described in panel (b), the tip and sample have parallel magnetization. Under a small positive bias, an occupied electron with up-spin (down-spin) near the Fermi energy of tip will tunnel to unoccupied spin up (down) band of the sample. The high DOS of spin-down electrons at the Fermi energy of tip and sample will lead to a high tunneling current while spin up will give a very limited contribution to the final current. However in the panel (c), the antiparallel magnetization scenario, high DOS of spin-down electrons in the tip side tunnel to the diminished DOS of spin down in sample side now, so the tunneled current is low. Though low DOS of

spin-up electrons in the tip can all tunnel to the sample, there is still very low current. Finally, the tunneling current is low for both orientations.

As we have introduced in the previous section, the tunneling current expression can be derived from time-dependent perturbation, but for the spin-polarized case, the wavefunctions of tip and sample should be expressed with spinors[40].

$$I_t \propto V(\rho_t^{\uparrow}\rho_s^{\uparrow}|M_{\uparrow\uparrow}|^2 + \rho_t^{\uparrow}\rho_s^{\downarrow}|M_{\uparrow\downarrow}|^2 + \rho_t^{\downarrow}\rho_s^{\uparrow}|M_{\downarrow\uparrow}|^2 + \rho_t^{\downarrow}\rho_s^{\downarrow}|M_{\downarrow\downarrow}|^2) \qquad (2.10.)$$

$\rho_{t,S}^{\uparrow,\downarrow}$ denotes the spin-resolved DOS of tip and sample, respectively, $\left|M_{\uparrow,\downarrow}\right|^2$ represent the tunneling matrix between the spin-resolved tip and sample.

The spin-resolved tip (sample) DOS can be expressed:

$$\rho_{t(s)} = \rho_{t(S)}^{\uparrow} + \rho_{t(S)}^{\downarrow} \qquad (2.11.)$$

The spin polarization of the tip (sample):

$$\mathrm{P_{T(S)}} = \frac{\rho_{\mathrm{T(S)}}^{\uparrow} - \rho_{\mathrm{T(S)}}^{\downarrow}}{\rho_{\mathrm{T(S)}}^{\uparrow} + \rho_{\mathrm{T(S)}}^{\downarrow}} \qquad (2.12.)$$

Hence, the equation (2.10.) can be reduced to:

$$I_t \propto V|M_0|^2\rho_T\rho_S(1 + P_T P_S cos\theta) \qquad (2.13.)$$

where M_0 is the average tunneling matrix and θ is the angle between the polarization orientation of tip and sample. As we can see from equation (2. 13.) if either tip or sample polarization ($P_{T,S}$) is 0, the tunneling current will reduce to nonpolarized current[41, 42] as we introduced before. Equation (2. 13.) also shows that I_t depends on components of spin-resolved DOS and the contribution of nonpolarized DOS of tip and sample. The

spin-resolved tunneling depends on the angle θ between tip and sample polarization directions as well, similarly to the case of planar magnetic tunnel junctions.

3 SUPERCONDUCTING PROXIMITY EFFECT IN A TOPOLOGICAL INSULATOR USING FE(TE, SE)

3.1 Bi_2Te_3/Fe(Te, Se) AS A PROMISING PLATFORM TO FORM A TOPOLOGICAL SUPERCONDUCTOR

Recently, the interest in SPE reignited due to the realization of topological insulators (TI)[43]. One of the most attractive applications of SPE is that the heterostructures of TIs and SCs are predicted to harbor topological superconductivity (TSC) hosting Majorana modes inside the vortex cores[44], as shown in **Figure 3. 1. 1**.

To achieve the TSC, it needs to meet two main conditions: 1, the existence of helical Dirac states on the surface of TI; 2, a gap induced by the *s*-wave SC pairing. Many trials focusing on coupling TIs with low-T_c SCs ($NbSe_2$[45, 46, 47] and elemental SCs[48, 49]) or with a high-Tc cuprates Bi-2212[50, 51, 52] have been carried out. However, these two types of TI/SC platforms still cannot meet our requirements:

- TI/$NbSe_2$ platform can only induce a SC gap of ~1mV makes the experimental characterization of the emergent phase challenging and also limits the potential future applications of any Majorana modes detected.
- The high T_c Bi-2212 still had conflicted results[50, 51, 52] which should be related to the short coherence length along the *c*-axis and also the large

mismatch between the Fermi surface of TI near the Brillouin zone center and that of Bi-2212 near the edge.

Based on the argument above, Fe-based SC could be a potential alternative to NbSe*2* and Bi-2212 because it can meet both requirements, i.e. large SC gap and comparable size of Fermi surface near the center of BZ. We choose the Fe-based high T_c SC Fe(Te, Se) with a ~2.5meV SC gap at the Gamma point in BZ as the substrate and grow Bi_2Te_3 thin films with molecular-beam epitaxy (MBE) on top of a cleaved Fe(Te, Se) bulk single crystal (**Figure 3. 1. 2** (a)).

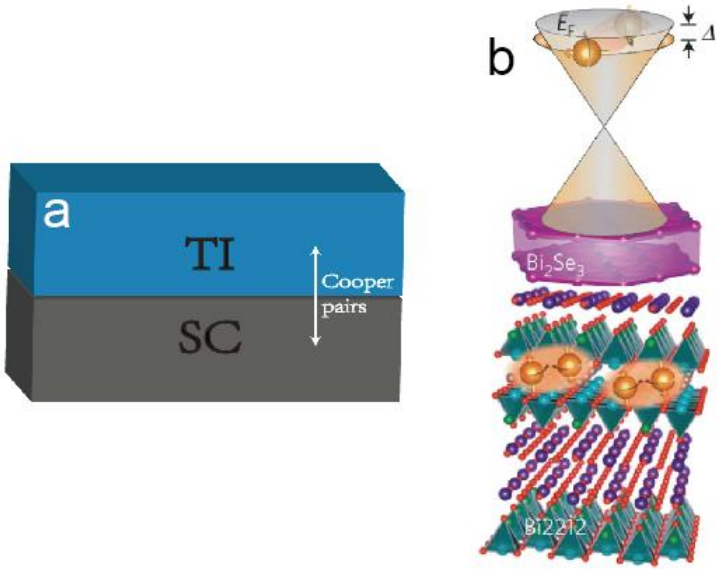

Figure 3. 1. 1. Schematic presentation of the TI/SC platform. (b) Bi_2Se_3 / Bi-2212 heterostructure. A SC gap opened within the Bi_2Se_3 Surface state. Reprinted from ref. 51.

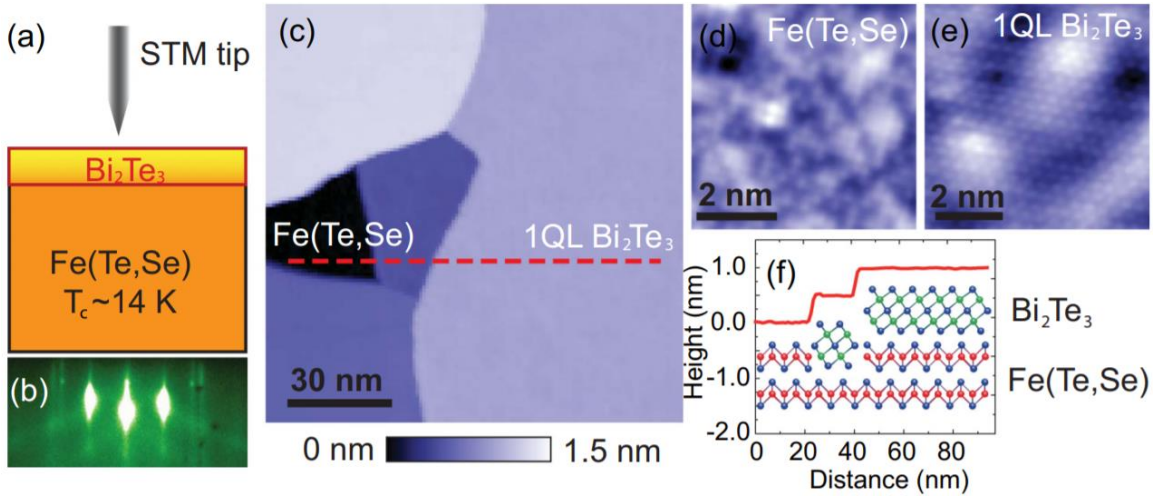

Figure 3. 1. 2. (a) Schematic of Bi_2Te_3/Fe(Te,Se) heterostructure. (b) Typical post-growth RHEED image of the MBE-grown heterostructure showing long streaks characteristic of two-dimensional layer-by-layer growth. (c) STM topograph showing (d) the exposed Fe(Te, Se) substrate with square atomic lattice and (e) the Bi_2Te_3 film with a hexagonal lattice structure. (f) Height profile taken along the dashed red line in (c) consistent with 1QL of Bi_2Te_3 grown on top of Fe(Te, Se). Reprinted from our work, ref. 53.

One of the main challenges in successful Bi_2Te_3/Fe(Te, Se) heterostructure growth is the incompatible atomic surface structure of the two materials—the exposed surface of cleaved Fe(Te, Se) along (001) is typically square lattice while Bi_2Te_3 has a hexagonal lattice, as shown in **Figure 3. 1. 2** (d, e). This will naturally induce a formation of two types of Bi_2Te_3 film domain rotated in-plane of 30 degrees relative to each other, as can be seen in the RHEED pattern of **Figure 3. 1. 2.** (b) where the outmost stipes split.

3.2 CHARACTERIZATION OF TOPOLOGICAL SURFACE STATES IN Bi_2Te_3/Fe(Te, Se)

As we have mentioned above, there are two requirements to realize a TSC in TI/SC heterostructure: the helical Dirac states on the surface of a TI and a SC gap due to induced s-wave SC pairing. To characterize the electronic structure of our BT films we use the QPI imaging method as we have introduced in the last chapter. Based on the APRES results[54], the interference between the top and bottom surface will be absent when the thickness is larger than 2QLs. That means there will be low spin-momentum locking indicative of the degenerate nature of the surface state in 1QL BT, which facilitates the observation of the backscattering vector. As a consequence, the morphology of QPI appears to be isotropic with similar intensity along with all angles (**Figure 3. 2. 1**(d-f)). We note that the observed QPI on BT is clearly distinct from the recently reported SS on the surface of Fe(Te, Se)[55]. Following the growth of 1QL BT/FTS, we also successfully grew 3QLs and 5QLs BT on top of FTS. Based on results from ref. 56, 57, and 58, away from Dirac point will open the backscattering channel due to the small hexagonal warping on the constant energy contour. And consistent with ARPES measurements, we observe the characteristic angle-dependent QPI pattern with energy-dispersive wave vectors along the Γ-M direction, which allows us to visualize the topological SS band dispersion (**Figure 3. 2. 2** (h, l)).

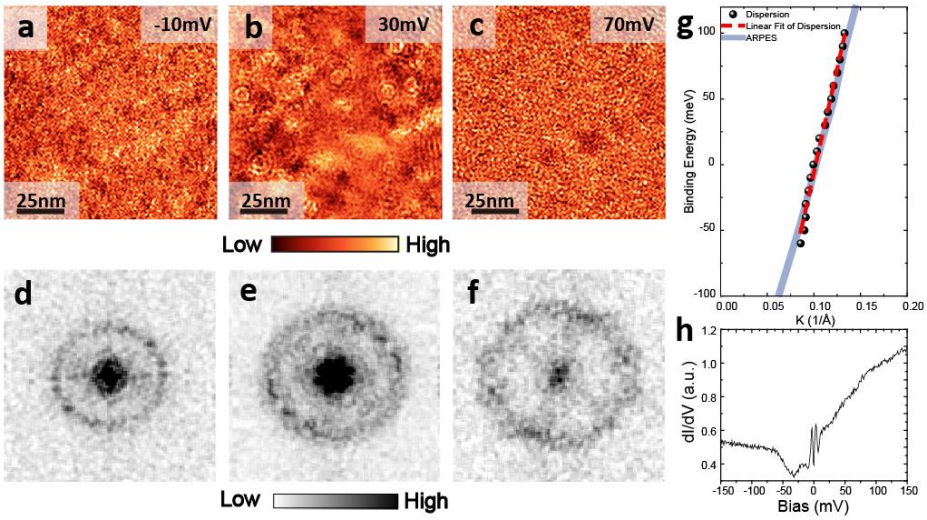

Figure 3. 2. 1. QPI pattern on single layer BT. (a-c) real space dI/dV map at specific energies and the corresponding (d-f) Fourier transform (FT) images. (g) Extracted QPI pattern along Γ-M direction for 1QL BT film. The red dash line is the fit of the QPI dispersion. The thick gray line represents the fit based on ARPES measurements in ref. 54, shifted by ~150meV to match the QPI dispersion. (h) Spatial average dI/dV spectrum over the QPI region. Reprinted from our work, ref. 53.

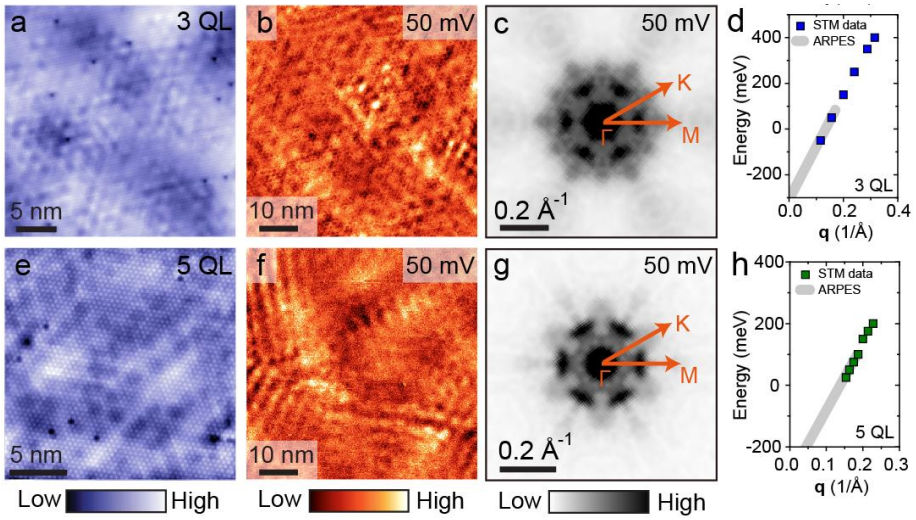

Figure 3. 2. 2. Thickness-dependent quasiparticle interference imaging of the BT SS. (a-d) is the topograph, *dI/dV* map over the same region, FT image of the *dI/dV* map, and extracted QPI dispersion and fit based on ARPES measurements on 3QL BT, respectively. (e-h) are for the 5QLs, respectively. Gray lines in (d) and (h) are the fit based on ARPES measurements in ref. 54, but both of them have a shift ~ 100meV. Reprinted from our work, ref. 53.

3.3 SUPERCONDUCTIVITY INDUCED ON THE SURFACE OF Bi_2Te_3/FE(TE, SE)

3.3.1 Temperature and magnetic field measurements of the induced gap

On the surface of 1QL BT/FTS, symmetric *dI/dV* spectra with respect to the Fermi energy and a clear energy gap $\Delta_{ind} \sim 3.5$ meV under 4.5K can be revealed (**Figure 3. 3. 1.** (a)). We acquire the average spectra under various *T* and find that the SC gap can persist up to 10K (**Figure 3. 3. 2.**(a)), which is a little bit lower than FTS's *Tc* ~14.5K. The *T* dependent Δ_{ind} presents the first indication of the proximity-induced superconductivity. Another significant evidence of the superconducting origin of Δ_{ind} is the *dI/dV* spectra evolution after the application of different magnetic fields (B). For a type II SC, when B is lower than Hc_2, *the* magnetic field will penetrate the sample in quantized flux quanta in the form of vortices.

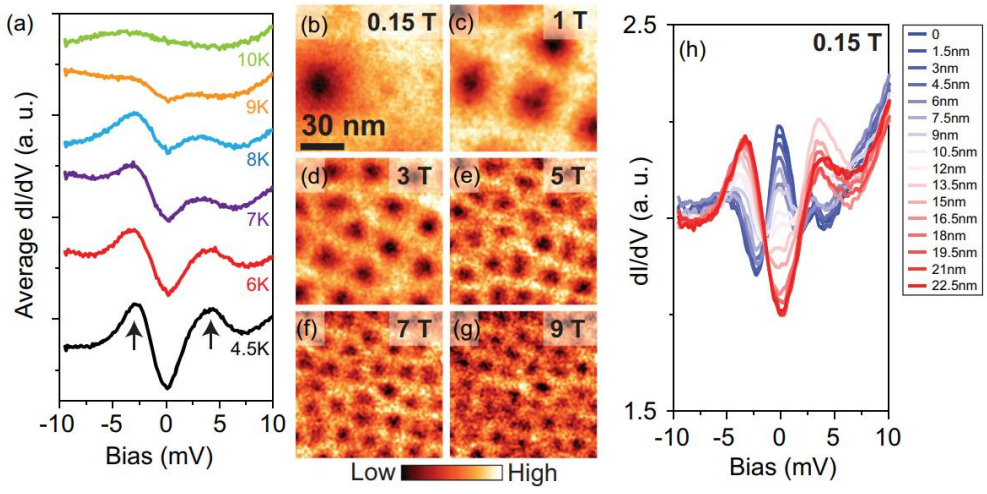

Figure 3. 3. 3. Temperature dependence of *dI/dV* spectra and Abrikosov vortex lattice imaging. Reprinted from our work, ref. 53.

Showing 'dark spot' vortex lattice up to highest magnetic field (9T) (**Figure 3. 3. 3**), *dI/dV* maps at ~ Δ_{ind} can give us the average magnetic flux per vortex ~ $2.16 \pm 0.07 \times 10^{-15} m^2 T$ (**Figure 3. 3. 4**). This value can be calculated by:

$$d = \left(\frac{4}{3}\right)^{\frac{1}{4}} \left(\frac{\Phi_0}{B}\right)^{\frac{1}{2}} \qquad \#(3.1)$$

Where Φ_0 is the magnetic flux quantum and B the magnetic field in Tesla.

We can see that the vortices in our BT/FTS heterostructure can persist up to much larger B compared to BT/$NbSe_2$[59], which is consistent with high Hc_2 of the FTS family. The linecut through a vortex core shows the suppression of gap edge peaks inside the vortex (**Figure 3. 3. 3** (h)).

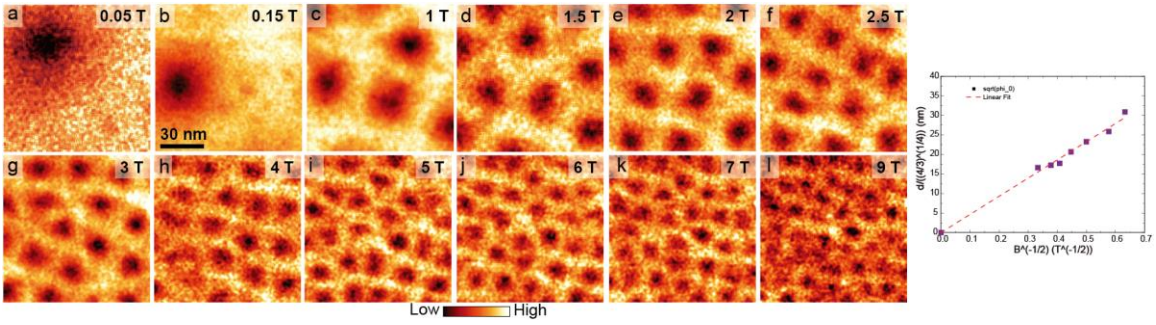

Figure 3. 3. 4. Vortex lattice under different B. (a-l) *dI/dV* maps under different fields. The plot extracts the average magnetic flux per vortex. The data points represent the average distance between vortices d based on FT of the vortices lattice in (a-l). Reprinted from our work, ref. 53.

3.3.2 Thickness dependence of the induced gap

We proceed to explore the induced SC gap dependence on the thickness of the BT film. From **Figure 3. 3. 5** we can see that the gap magnitude on single layer BT is similar to the substrate while the gap evolves to 1.8meV on 3QLs BT and 1.5meV on 5QLs BT. We emphasize that the induced gap on BT/FTS system is almost 3 times larger than the previous largest gap on TI/$NbSe_2$. The finite conductance around Fermi energy is possibly due to the local, incoherent states like the impurity states, which can also explain why our s-wave BCS function cannot fit the experimental *dI/dV* spectra well.

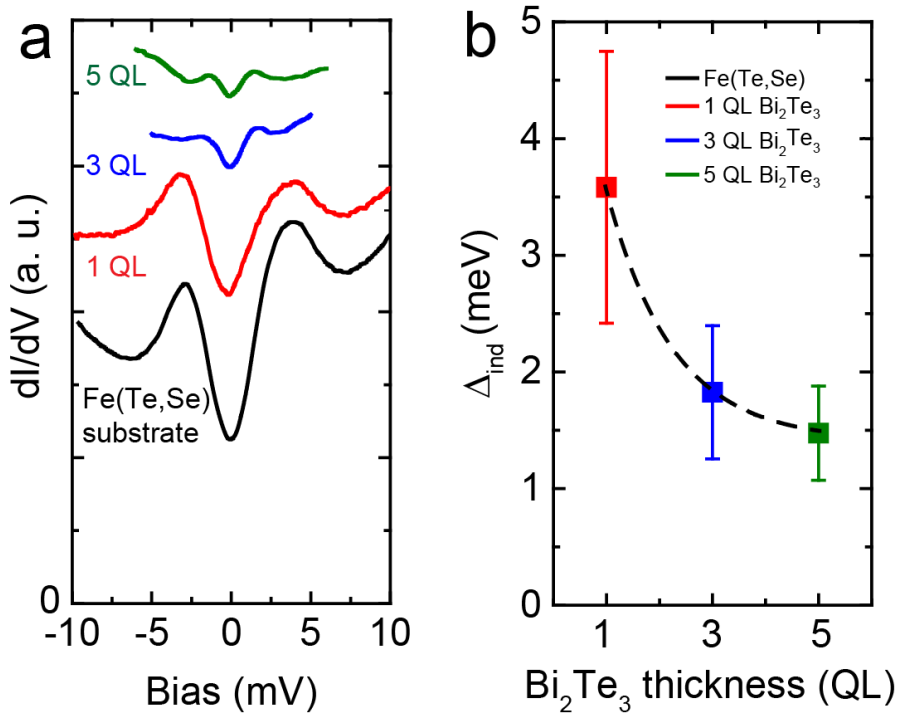

Figure 3. 3. 5. Evolution of the Δ_{ind} with BT film thickness. (a) average *dI/dV* spectra obtained on different thickness BT films. (b) the plot of the magnitude of Δ_{ind} extracted from (a) as a function of BT thickness. Reprinted from our work, ref. 53.

3.3.3 BCS theory fitting

We compare the obtained average *dI/dV* spectra on 1 QL, 3QLs, and 5QLs BT with a thermally broadened s-wave BCS spectral function from Dynes et al.[60] with 2 parameters: gap magnitude Δ and the scattering rate Γ. However, the s-wave function cannot reproduce the two most prominent features of our spectra at the same time — the sharpness of coherence peaks and the zero-bias conductance. For example, as shown in **Figure 3. 3. 6,** after tuning the Δ and Γ, the BCS curve can match the zero-bias conductance and the overall 'V' shape of the experimental spectra but the coherence peaks clearly cannot be reproduced. Conversely, choosing parameters that can match the s-wave function with the sharpness of coherence peaks will always lead to a curve deviating from experimental spectra.

The BCS fit on BT/$NbSe_2$ from ref. 46 also observed the small deviation from the experimental spectra beyond a critical thickness and the authors ascribed that to the formation of topological surface state. It's not our case considering that spectra on all of the thickness BT/ FTS heterostructures— before and after the formation of topological surface states— cannot be reproduced by the s-wave BCS fit. We hypothesize that deviation as the result of the presence of impurities states which could affect the zero-bias conductance.

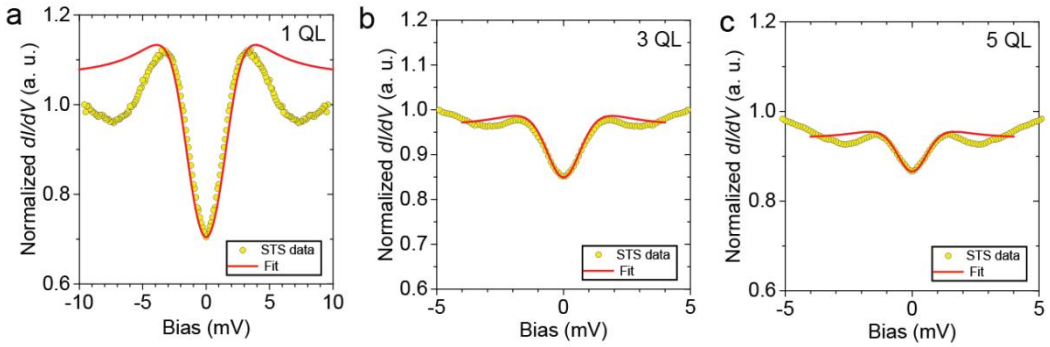

Figure 3. 3. 6. Average *dI/dV* spectra, symmetrized around the fermi energy for visualization purposes (yellow points), and s-wave BCS spectral function fit (red curves) for 1, 3, and 5QLs BT films. Reprinted from our work, ref. 53.

We proceed to explore if the SC opens a gap at the SS of BT. If a gap exists in the SS, the FTs of *dI/dV* maps near the Fermi level should exhibit no detectable QPI signal within the gap. We start with 1QL BT which has only coherent SS crossing Fermi level. FTs of *dI/dV* maps (**Figure 3. 3. 7** (a-d)) resemble those QPI patterns observed at higher energies. However, when entering the SC gap energy, we discover a striking suppression of scattering from 2meV to -2meV, indicating a full gap in the SS around the Fermi level (**Figure 3. 3. 7** (e-i)). This result is further supported by the analysis of the QPI intensity as a function of energy, where complete suppression of the QPI pattern occurs exactly within the induced gap and recovers outside the gap (**Figure 3. 3. 7** (j)). For the 3QLs BT, one can observe similar pattern change from within to outside induced gap range (**Figure 3. 3. 7** (k)).

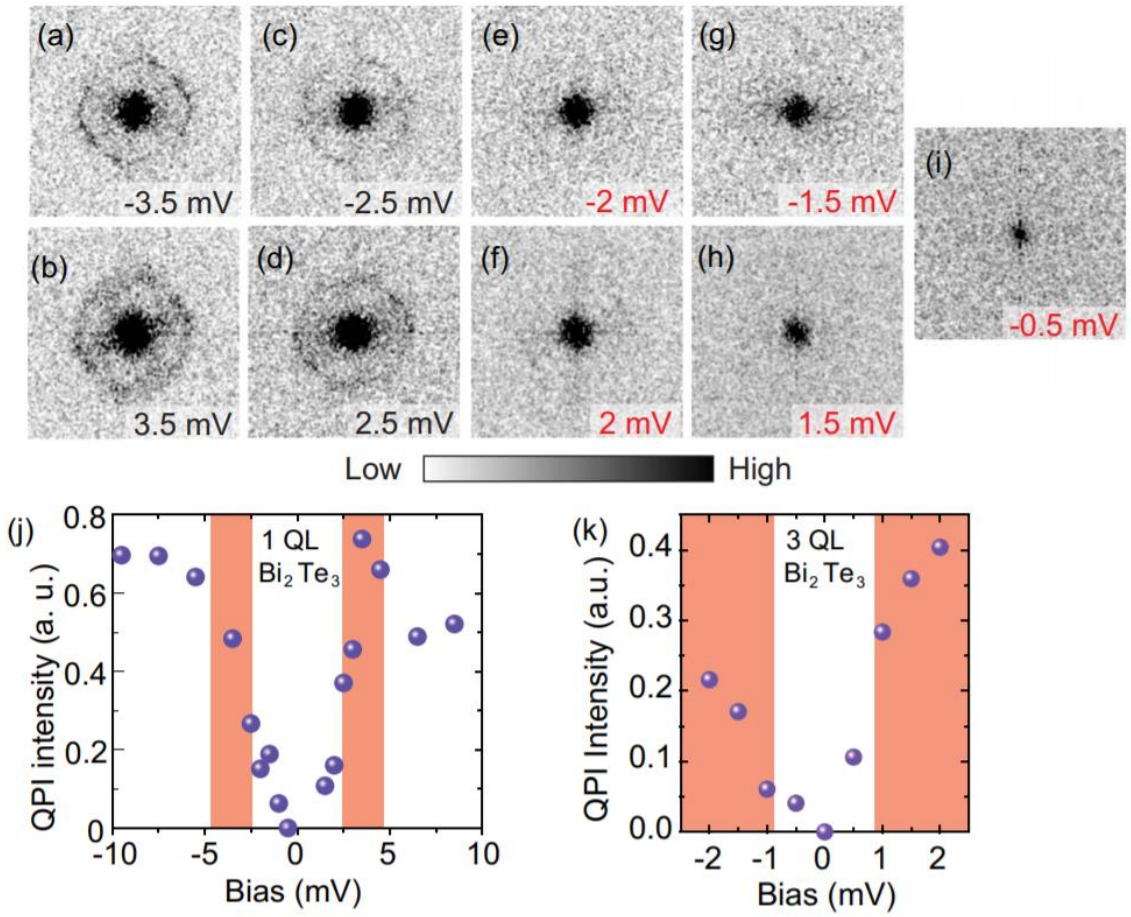

Figure 3. 3. 7. Suppression of QPI within the SC gap. (a-i) FT of dI/dV maps at various biases. Distinct quasi-circular QPI peak can be seen from (a) to (d), while for (e)-(i) the peaks are significantly suppressed. (j, h) Normalized QPI intensity is relative to the background as a function of STM biases for 1QL and 3QLs BT, respectively. The orange lines indicate the approximate energy of the observed gap peaks and the width of lines corresponds to thermal broadening at the measurement temperature. Reprinted from our work, ref. 53.

3.4 CONCLUSION AND DISCUSSION

Our results build up the platform achieving topological SC with higher Δ_{ind} and T_c using FTS and related Fe-based SCs. We observe that the induced SC opens a gap on the SS of BT films with different thicknesses. The multi-gap structure of FTS with different gap magnitudes on different Fermi surfaces allows us to test the role of momentum-space matching of the Fermi surfaces at the interface in inducing proximity. The Fermi surface of FTS is composed of electron pockets at M point and hole pockets at Γ point, while BT has only SS crossing Fermi level as we have mentioned before (**Figure 3. 3. 8**). It's natural to ask the question: which pocket induces the SC gap on the surface of BT? Previous ARPES result on FTS has confirmed that the larger gap $\Delta_1 \sim 4.2$meV is at the M point (hole pocket), while the two bands at Γ have smaller gaps: $\Delta_2 \sim 1.7$meV and $\Delta_3 \sim 2.5$meV[61]. Considering the out-of-plane orbitals might be more effective to tunnel across the interface into the normal material, we hypothesize that the out-of-plane p_z orbital at M point plays a role in the proximity effect. This hypothesis can be supported by our experimental result that the induced gap magnitude $\Delta_{ind} \sim 3.5$meV is smaller than Δ_1 but larger than Δ_3. In contrast to our conventional physical picture that the SC proximity effect on BT film should arise from the momentum-space match between the electron pocket of FTS and BT Fermi surface, the induced gap is due to the momentum-mismatched electron pockets of the FTS referring to our schematic of 1st BZ of FTS and BT (**Figure 3. 3. 8**). Moreover, this intuitive picture could also explain the contact plane dependent observation of the SPE at the interface of normal materials and cuprate superconductors. Cuprates host an in-plane $d_{x^2-y^2}$ -wave superconducting order

parameter, so based on our orbital picture the proximity effect would be strongest when contacting the side of the superconductor. Indeed, Δ_{ind} in a normal material was measured to be the largest when contacting the side surface of the high-T_c cuprate $YBa_2Cu_3O_{7-x}$[62].

Another interesting result that we cannot fully understand is the appearance of zero-bias peak (ZBP) in *dI/dV* spectra inside the core of the magnetic vortex after applying B (**Figure 3. 3. 4**). One of the possibilities is that this ZBP hosts Majorana fermion at zero bias. The nonsplitting ZBP away from the vortex center in 3QL BT/FTS surface could help us rule out the trivial bound state scenario which has been detected in >3 QLs BT thin films grown on top of $NbSe_2$. In 1QL BT thin film, the ZBP gets suppressed but it's still not splitting away from the vortex center. Further work needs to be done to help us unveil the origin of the ZBP by a new technique, specifically SP-STM.

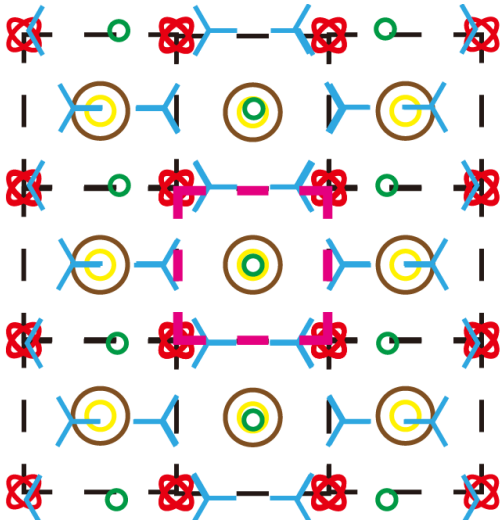

Figure 3. 3. 8. The 1st Brillouin Zone mismatch between BT and FTS. The blue dashed hexagon represents the BZ of BT while the black dash square indicates FTS. Yellow and brown circles around the center Γ point of FTS BZ position the d orbitals while the red flowers around M point are the p_z orbital of FTS. Green circles represent the electron pockets at Γ point of BT. Reprinted from our work, ref. 53.

4 CHARGE-STRIPE CRYSTAL PHASE IN AN INSULATING CUPRATE

4.1 CHARGE STRIPE ORDER IN CUPRATES

As we have introduced in the introduction chapter, the experiments so far have primarily focused on exploring the novel forms of the charge order in the pseudogap phase, shortly before or after the onset of superconductivity. And the prior measurements presented tremendous pieces of evidence for the existence of a 2-dimensional charge order. However, there could be a 'stripe' phase[8] appearing with competition between magnetism and the kinetic energy of mobile carriers in doped AFM[8]. The neutron scattering measurement provides experimental evidence for such coexisting static spin and charge order in $La_{1.48}Nd_{0.4}Sr_{0.12}CuO_4$ (LNSCO)[8] and $La_{1.875}Ba_{0.125}CuO_4$ (LBCO)[63]. Actually, the neutron scattering cannot detect the charge order because the neutron is neutral but the lattice distortion is associated with the order. Then using resonant soft X-ray scattering (RSXS), Abbamonte et al.[64] observed the static charge 'stripe' in LBCO with x~1/8 by measuring the charge correlations in reciprocal space. However, observation of the static 'stripe' phase didn't only happen in La-based cuprate, but also in Y-based ones. Wu et al.[65] studied $YBa_2Cu_3O_y$ by NMR with high B applied which induces a $4a_0$ charge stripe modulation and dissipates superconductivity. This result kind of indicates that the charge order is a propensity of hole-doped cuprates. Following that, in the same material but the varying level of hole doping, Comin et al.[66] observed a short-range unidirectional charge order breaking translational and rotational symmetry by RXS. Interestingly, they found

that SC weakens more along the transverse direction of stripes than longitudinal. Based on all the works we introduced above, only static charge stripe has been caught inside hole-doped cuprates. In contrast to all the previous works, Ghiringhelli et al.[67] detected low energy charge stripe fluctuation by using resonant elastic x-ray scattering (REXS) inside $YBa_2Cu_3O_{6+x}$ with doping level ranging from 0.045 to 0.065 when *T* varies. All of the measurements came to a similar conclusion that charge stripe competes with SC.

In the introduction chapter, we also introduced the 2D charge order (also called checkerboard) observed in Bi- and Cl- based cuprates in the pseudogap phase. There are rare literature works talking about one-dimensional charge stripe (either static or fluctuating stripe) in Bi-based cuprate[68, 69]. And all of the charge stripe experiments mentioned above are related to the short before or after the SC phase, while our work corroborates the existence of static order in the AFM phase of Bi-2212.

4.2 ELECTRONIC EVOLUTION WITH OXYGEN DOPING IN $Bi_2Sr_2CaCu_2O_{8+\Delta}$

$Bi_2Sr_2CaCu_2O_{8+\delta}$ (Bi-2212) is a layer cuprate and inside which the interstitial O atoms control the hole doping level (*p*) and each of them contributes approximately 2 holes to the bulk. The as-grown Bi-2212 tends to be optimally doped with $p \sim 0.16$ per unit cell and T_c reaches a maximum at ~ 91K. To lower *p*, the sample can be annealed in the ultrahigh vacuum (UHV) at high temperatures. Bulk insulating cuprates are very difficult

to characterize via tunneling techniques due to the insufficient electron for tunneling[70]. However, this problem can be solved by a 'flash' annealing in UHV which primarily removes O atoms from the topmost layers while the bulk still keeps SC. Enough carrier density allows us to access the previously inaccessible AFM phase of Bi-2212 before the charge transfer gap closed through STM/S at low $T \sim 4.5$K.

Here we start with cleaving the optimally doped Bi-2212 bulk single crystal (T_c~91K) and take *dI/dV* spectra, which exhibits inhomogeneous spectral gap[71] as consistent with the previous study (**Figure 4. 2. 1** (b)). Then we anneal Bi-2212 at ~ 270^{o}C in UHV and reinsert STM. Though the topograph (inset in **Figure 4. 2. 1** (c)) looks similar to non-annealed, the electronic property changed a lot—the SC gap changes to a V-shape more linear spectrum in lower energy with poorly defined gap-edge peaks, reminiscent of that obtained on underdoped Bi-based cuprates with low T_c. Interestingly, we detect a large insulating charge gap ~ 1.1eV when further annealing with higher T ~380 ^{o}C (**Figure 4. 2. 1** (d, f)). Besides the electronic evolution from low T annealed crystal, the topograph (inset in **Figure 4. 2. 1** (d)) annealed at high T looks clearly disparate from the low T surface. Those stripes pattern is what we called static charge stripe and hereby the material is in charge stripe crystal phase.

4.2.1 Surface hole density estimate in $Bi_2Sr_2CaCu_2O_{8+\delta}$

To quantify the effect of annealing, we count the oxygen dopants that can be detected at high bias *dI/dV* map in Bi-2212—'type A' oxygens located near SrO plane and 'type B'

oxygens positioned close to BiO layer[72, 73, 74]. We find that the densities of both are significantly reduced after annealing (**Figure 4. 2. 1** (e) and **Figure 4. 2. 2**). The annealing process also creates oxygen vacancies in the SrO layer. We estimate the hole density using the following method:

Assuming that each interstitial oxygen atom contributes 2 holes, while each apical oxygen vacancy contributes 2 electrons, we can calculate the average hole density contributed by these 3 types of dopants for the 5 samples we used to get **Figure 4. 2. 3** (A) and plot them in comparison to the Presland formula[75] (**Figure 4. 2. 3** (B)). Though the general trend of p vs Tc based on our dopant counting method can follow the dome-shaped dependence based on the Presland formula, there is a systematic offset for all samples. The offset could be due to the yet detected dopants. We calculate the average of all of the dopants for the underdoped samples to be 2.2%. Assuming that this offset doesn't significantly change as a function of doping, we estimate that the sample in **Figure 4. 2. 1** (c) is $p\sim 0.057\pm0.008$.

This dopant concentration is consistent with the averaged V-shaped *dI/dV* spectrum and the observed incommensurate charge-ordering wave-vectors Q*=0.28±0.03 and Q**=0.73±0.04, all of which are qualitatively similar to those reported in bulk underdoped Bi-2212 with comparable hole density[76, 16]. We note that another source of doping could in principle come from cation removal. However, since cation concentration is reported not to change after annealing as high as 840^{o}C[77], it's unlikely to change at the significantly lower T used in this work. A more accurate measurement of the Fermi surface by QPI in future studies could provide a more precise estimate of the hole density.

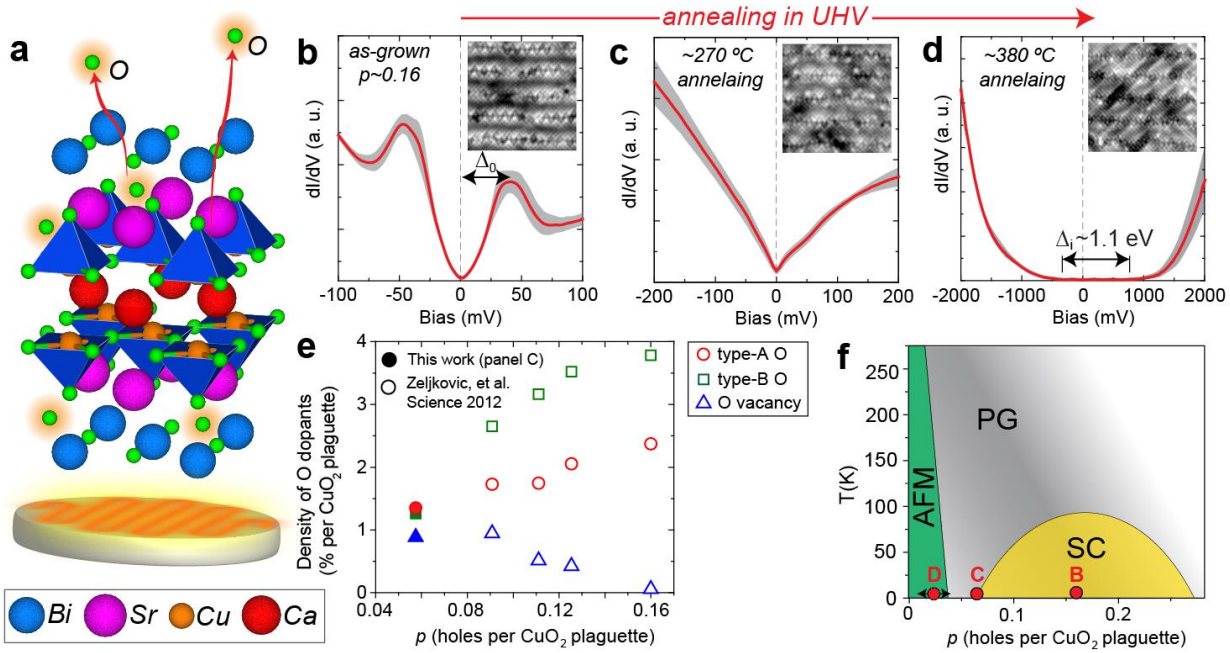

Figure 4. 2. 1. Surface preparation and electronic characterization. (a) Schematic of the top half of the Bi-2212 unit cell. Annealing removes a fraction of the oxygen atoms, thus reducing the hole density. (b-d) Average *dI/dV* spectra obtained on the surface before annealing (b), after annealing at ~270°C (c), and after annealing at ~380 °C (d). One half of the width of the grey shaded line at each bias represents two standard deviations within *dI/dV(**r**, V)*. Insets in (b-d) represent typical STM topographs. (e) The density of different types of O defects as a function of *p*. (f) Schematic of the hole-doped cuprate phase diagram. AFM: antiferromagnetic Mott insulator, SC: superconducting state, PG: pseudogap. Red circles represent approximate doping levels from (b) and (c). Reprinted from our work, ref. 78.

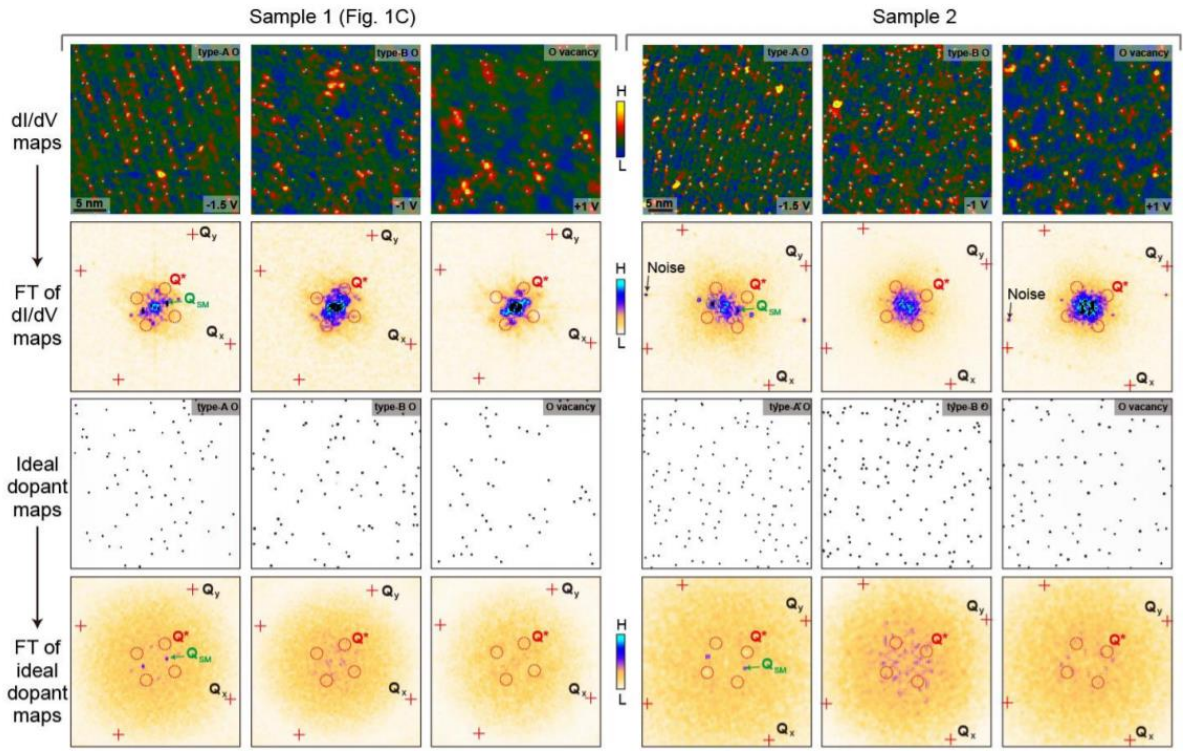

Figure 4. 2. 2. Nanoscale imaging of oxygen dopants in underdoped Bi-2212 samples annealed at comparable temperatures: left half with p~ 0.057±0.008 and the right half with p~ 0.063±0.008. (Top row) dI/dV(r, V) maps showing three known types of O defects: type-A O(-1.5V), type-B O(-1V), and apical O vacancy(+1V), and (Second row) their associated Fourier transforms. Superimposed blue circles are the dopants identified. (Third row) Idealized dopant locations obtained from *dI/dV*(r, V) maps in the top row, and (Bottom row) their associated Fourier transforms. Reprinted from our work, ref. 78.

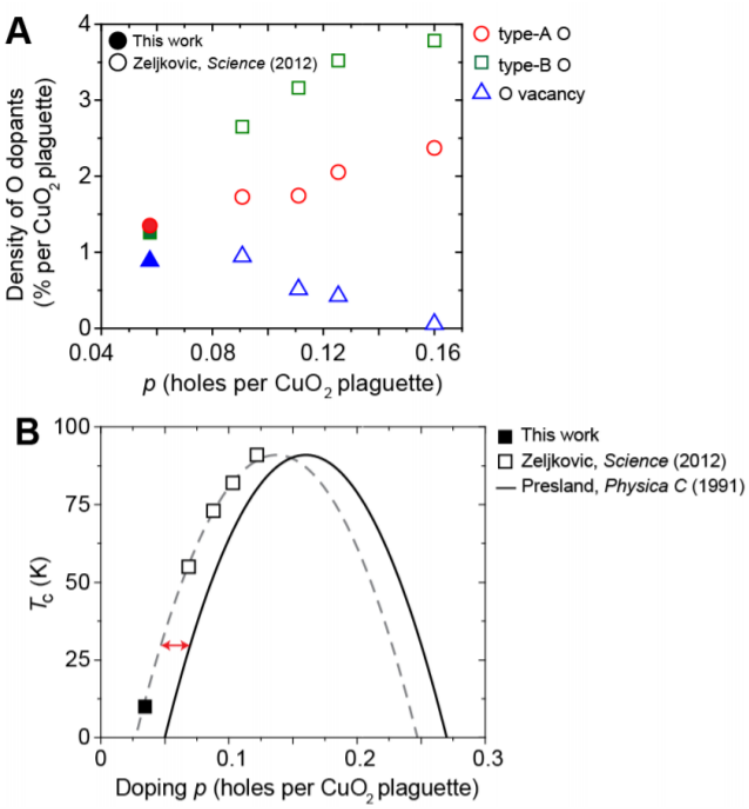

Figure 4. 2. 3. (A) Density of each type of O defect as a function estimated hole doping for 5 different samples. (B) Tc as a function of estimated hole doping based on measured densities of O defects for 5 samples in (A). Presland formula (black line) and the same curve shifted to match the data (dashed line). Reprinted from our work, ref. 78.

4.2.2 2D charge order observed in underdoped $Bi_2Sr_2CaCu_2O_{8+\delta}$

To demonstrate the similarity between the phenomena observed on our surface-doped samples and the bulk samples of comparable hole density studied previously, we compare the properties of the emergent charge order. Both annealed at T~270^{o}C samples display the similar charge order along with two lattice directions, seen as modulations in real-space dI/dV(r, V) maps (**Figure 4. 2. 4** (A-B)), and as nondispersive peaks in the FTs (**Figure 4. 2. 4 (C-F)**). We use Gaussian fitting (Supplementary information ZZ) to determine the wave-vector magnitude to be: (Sample 1) |Q*|~0.28±0.03 and |Q**|~0.73±0.04, and (sample 2) |Q*|~0.27±0.03 and |Q**|~0.71±0.05, which are consistent with those measured on the samples with similar bulk density[16]. For the sample annealed at higher T~380^{o}C, we cannot detect all types of the oxygen dopants based on the dI/dV(r, V) maps methods we introduced above because of the low conductance within the charge transfer gap with size ~1.1eV.

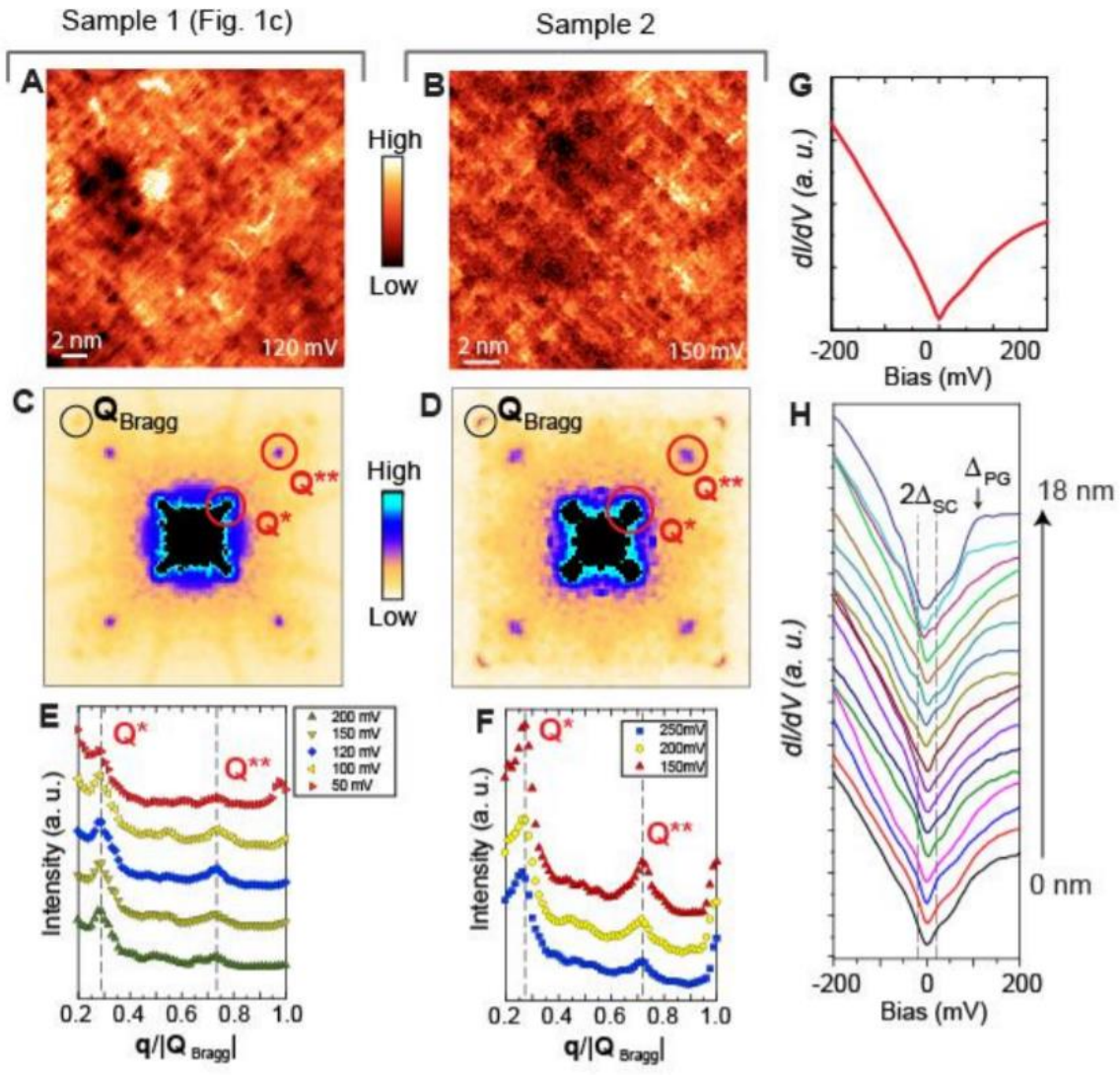

Figure 4. 2. 4. Charge ordering in non-insulating, heavily underdoped Bi-2212. (A. B) *dI/dV*(r, V) maps. (C, D) their associated 4-fold symmetrized FTs and (E, F) corresponding linecuts, vertically offset for clarity, acquired from the center of the FT to the atomic Bragg peak Q_{Bragg} at various energies. We observe two charge ordering vectors: (Sample 1)|Q*| ~ 0.28 ± 0.03 and |Q**|~0.73 ± 0.04, and (sample 2), |Q*|~ 0.27 ± 0.03 and |Q**|~ 0.71 ± 0.05 (in units of $2\pi/a_0 = 1$, with a_0 ~ 3.8 Å corresponding to the Bi-Bi, or equivalently Cu-Cu, distance). (G) Average dI/dV spectrum of sample 1, (H) dI/dV spectra, vertically offset for clarity, acquired over ~ 18nm area on sample 1. The kink near the Fermi level is associated with the SC gap Δ_{SC}. Reprinted from our work, ref. 78.

4.3 1D CHARGE STRIPE IN ANTIFERROMAGNETIC PHASE $Bi_2Sr_2CaCu_2O_{8+\Delta}$

Previous observations of charge ordering in hole-doped cuprates have been limited to the approximate doping level achieved in **Figure 4. 2. 1** (c), in the pseudogap regime with a finite density of states at the Fermi level, after the charge transfer gap closed. However, after annealing at T ~380°C, an insulating gap Δ ~ 1.1eV opens in the spectrum taken at 4.5K on the Bi-2212 surface (**Figure 4. 2. 1** (d)), comparable to that observed in bulk insulating Bi-2212[79]. The gap is asymmetric with respect to the Fermi level and extends from -0.3eV to 0.8eV. A typical STM topograph of an insulating sample, which contains both structural and electronic information, shows the individual Bi atoms on the surface and the characteristic super modulation oriented at a 45° with respect to the lattice. Prominently, the topograph also exhibits periodic unidirectional features aligned parallel to the Cu-O-Cu lattice direction, which have never been seen before. The spatial extent of unidirectional stripe domains is typically ~ 5-8 nm in length, but it can be as large as ~ 10 nm square region in **Figure 4. 3. 1**(c), spanning > 500 unit cells. The periodic nature of the stripes can be confirmed by doing 2D discrete FT to the STM topograph, where we can see the 2 peaks Q^x_{CO} and Q^y_{CO} emerge at (0.25, 0) and (0, 0.25), respectively (**Figure 4. 3. 1**(b)). Those two peaks represent the stripes have an exactly 4a0 wavelength in real space along either lattice direction. In contrast to previously observed bond-centered 2D charge order, the charge stripes are site-centered, positioned on Bi atoms and therefore on top of Cu atoms, which can be confirmed from the filtered topograph (**Figure 4. 3. 1**(e)) and the linecuts from the center of FT image to Bragg peaks (**Figure 4. 3. 1**(f)). The

unidirectionality can be quantitatively confirmed by the FT (**Figure 4. 3. 1**(d, f)) of mostly horizontal lines topograph (**Figure 4. 3. 1**(c)), where there is only Q^{x}_{CO} peaks along vertical direction but no Q^{y}_{CO} along the horizon. Based on the modulation amplitude maps we constructed along two lattice directions (**Figure 4. 3. 1**(g, h)), we can observe a strong anti-correlation relation between the two (inset in **Figure 4. 3. 1**(h)). This is consistent with the observation that a certain area only hosts modulation along either x or y direction, but not both. We should note that this unidirectionality cannot be explained by a directional tip because we can observe stripes along both lattice orientation within the field-of-view using the same tip.

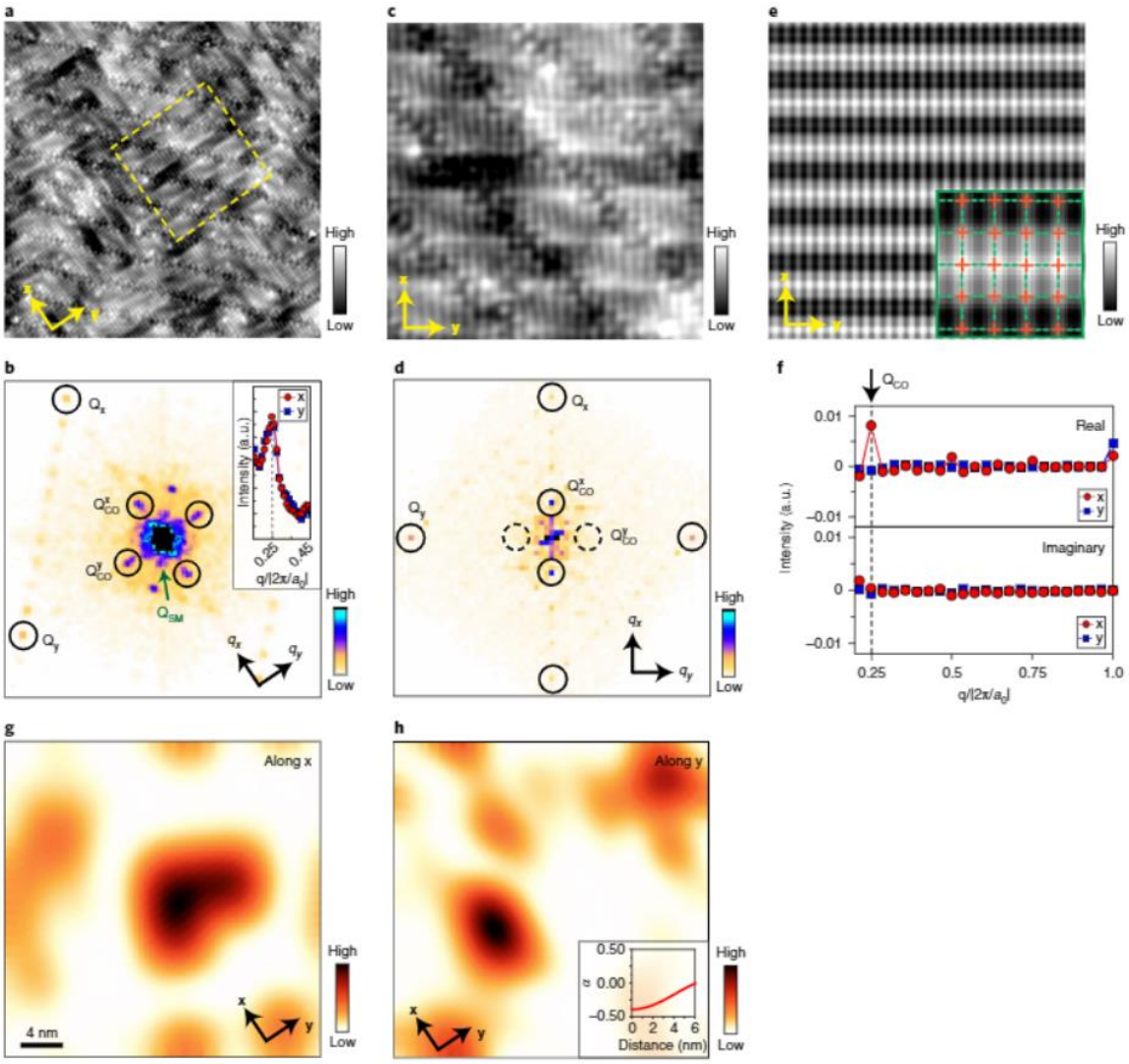

Figure 4. 3. 1. Unidirectional charge-stripe order in insulating Bi-2212. (a, b) Atomically resolved STM topograph of a ~30nm surface area (a) and its associated FT (b). Charge-stripe ordering peaks (Q^{x}_{CO} and Q^{y}_{CO}) and the structural supermodulation peak (Q_{SM}) are identified. Inset in (b), linecut along Bragg peaks (Q_x and Q_y). (c, d) Magnified view of a ~10nm square STM topograph hosting a single charge-stripe direction (dash yellow square in (a))(c) and its associated FT (d). (e) Fourier-filtered STM topograph from (c) isolating contribution s from wave-vectors at Q^{x}_{CO}, Q^{y}_{CO}, $Q_{x,}$ and Q_y only. The topograph demonstrates that the charge order is site-centered. Inset, the position of Cu atoms (orange crosses) and O atoms (green ellipses) in the CuO_2 layer with respect to the filtered STM topograph. (f) Linecuts from the center of FT image (d) to Q_x and Q_y, showing the real and imaginary FT components separately. Both Q^{x}_{CO} and Q_x show non-zero real components, while the imaginary components are zero, thus confirming that they are in phase. (g, h) The amplitude of the charge-stripe order along x (g) and y (h) lattice directions acquired over the region in (a) that show strong anti-correlation. Reprinted from our work, ref. 78.

4.3.1 Electronic origin of 1D Charge stripe

The electronic origin of the charge modulation can be studied by acquiring *dI/dV* maps, where the modulation is visible as bright lines directly corresponding to the equivalent patterns observed in the topograph (**Figure 4. 3. 2** (a, b)). The associated FT also shows peaks at Q^{x}_{CO}, Q^{y}_{CO} with the same wave-vector as topograph (**Figure 4. 3. 2** (c)). And as shown in **Figure 4. 3. 2** (e), the modulation is nondispersive with biases, confirming the nature of charge order. To describe the electronic structure of the striped hole crystal in more details, the *dI/dV* conductance linecuts across the stripes are shown in **Figure 4. 3. 2** (f). This modulation by 4a0 periodicity can also be seen in the spatial map of the charge transfer gap and its associated FT (**Figure** 4. 3. 3). The charge stripe by identical periodicity (4a0) as 2D charge order observed in the pseudogap phase of cuprate is likely associated with CuO_2-derived bands as it's generally accepted for Q*. We note that in addition to the upper Hubbard and lower Hubbard bands, other high energy bands may also be present at energies of ~1-2eV where Q_{CO} is observed. However, if the charge stripe is associated with other bands, one may expect to see the same ordering in the STM topographs and/or dI/dV maps in samples with slightly higher doped samples, such as the very underdoped Bi-2212 with p~ 6%. However, at -1V, -1.5V, and 1V *dI/dV* maps we cannot see the signs of this order.

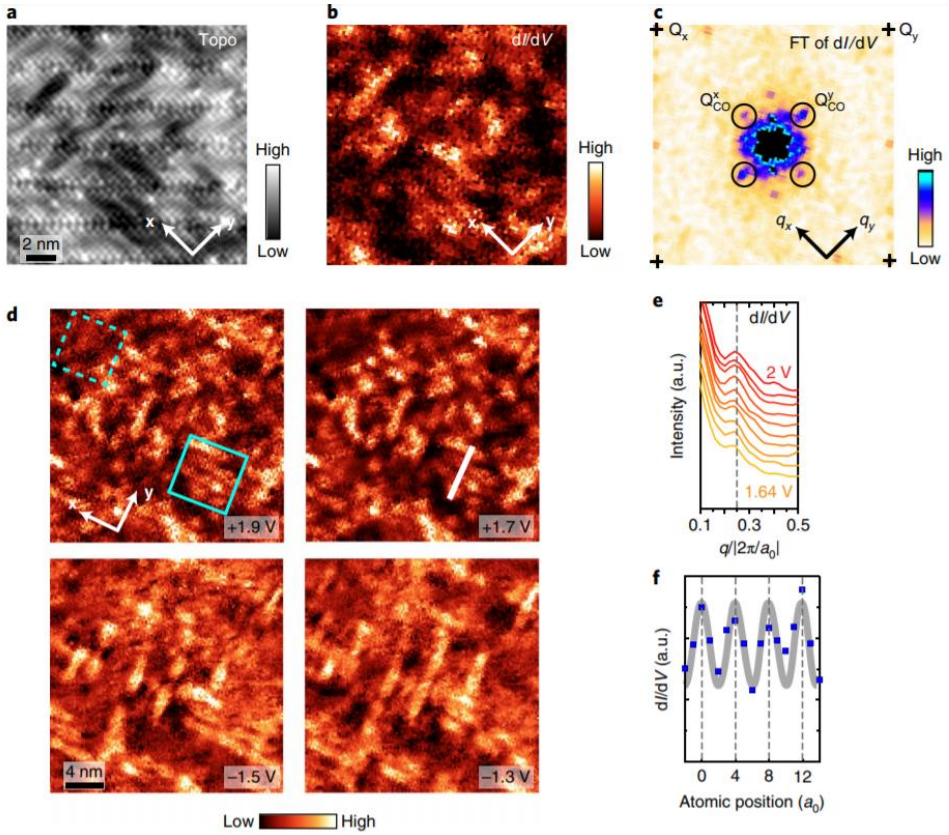

Figure 4. 3. 2. Visualizing the charge-stripe order in STM *dI/dV* map. The atomic topograph of insulating Bi-2212 and the *dI/dV* map (b) obtained over the same area. (c) Discrete FT of (b) showing the 4a0 charge modulation periodicity peaks Q^{x}_{CO} and Q^{y}_{CO}. Crosses in the corner indicate the positions of the atomic Bragg peaks. (d) Four integrated *dI/dV* maps at different biases over the same region of the sample. To enhance signal-to-noise, each map is an average of five *dI/dV* maps, spaced by 40mV, centered on the bias labeled. (e) a series of linecuts, offset for clarity, in the four-fold symmetrized FT images of *dI/dV* maps at ten equally spaced biases from V=1.64V to 2V. (f) real space linecut along the white line drawn in (d) showing a variation of the conductance signal within in the *dI/dV* map (green square), the ideal 4a0 modulation as a visual guide (gray curve). Reprinted from our work, ref. 78.

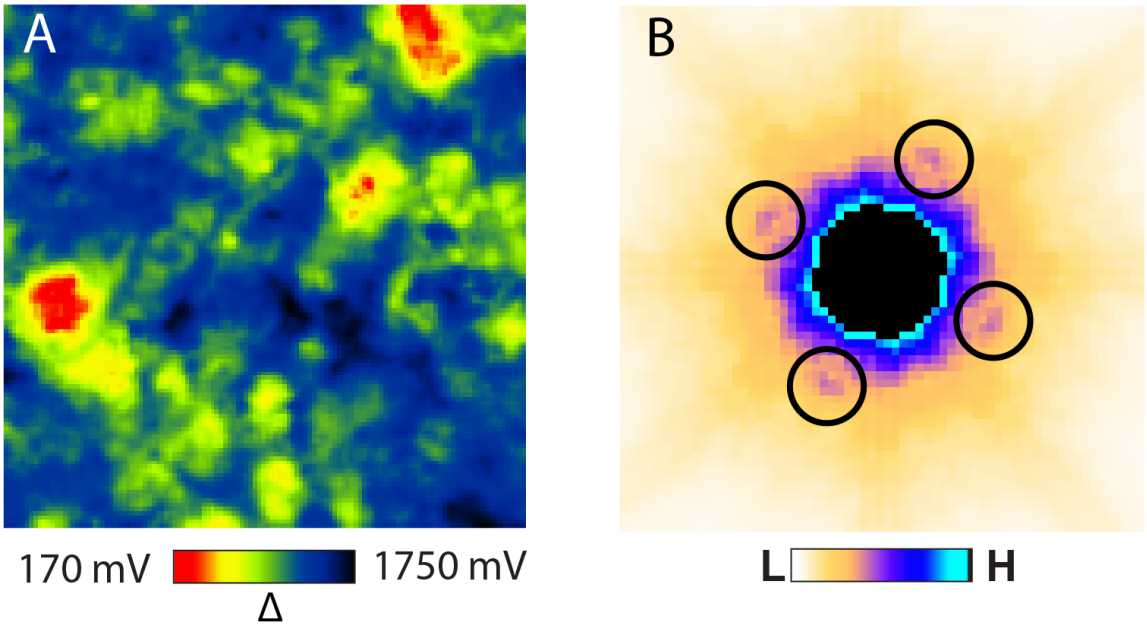

Figure 4. 3. 3. (A) The map of charge transfer gap over the same region of the sample as Figure. 4. 3. 2 (d) and its associated four-fold symmetrized FT (B). Reprinted from our work, ref. 78.

4.4 CONCLUSION AND DISCUSSION

In addition to previously observed smectic and nematic orders in the pseudogap phase, we reported strong evidence for perhaps the most elusive electron liquid crystal phase in ultra-low hole-doped cuprates—the charge-stripe crystal phase. In contrast to the charge-ordered phases in the pseudogap phase manifested at low energies near the Fermi level, the striped hole crystal phase is detected in the insulating state and highly probably tied to the spatial modulation of charge transfer gap. Given the long term debate on whether the stripe (checkerboard) that breaks (preserve) C4 rotational symmetry is favored in cuprates, our work provides real-space evidence that strongly indicates the preference of lightly doped cuprates to form charge stripes over the checkerboard. The large phase-coherent regions suggest that the striped hole crystal may exist as a stable ground state of a lightly doped Mott insulator stabilized by long-range Coulomb interaction. Moreover, the coexistence of ordered and disordered regions within the same field of view (dashed and solid square in **Figure 4. 3. 2** (d)) indicates the possibly coulomb frustrated phase separation. We also note that the conducting bulk below the insulating top layers may screen the long-range Coulomb interaction in the surface layers. The observed charge stripe crystal phase is consistent with the picture of fluctuating stripes pinned by the chemical disorder. We expect it could be detected by resonant X-ray scattering provided that the insulating state achieved at the surface by annealing extends into the bulk over micrometer-scale distances. We note that our measurement cannot separate spin from charge signal which means the role played by spin in the stripe hole crystal is still unclear.

However, because coexistent spin and charge order has been observed in La_2NiO_{4+x}[80], albeit being diagonal and with a much larger charge transfer gap, it's possible that the insulating charge stripes in Bi-2212 also carry a periodic ordering of spins. It may need SP-STM to test this in the future.

Prior experiments have suggested that the charge ordering in cuprates may be related to the pseudogap and that its wavevector exhibits a doping dependence as is it were driven by Fermi surface scattering. However, our measurements of stripe charge order in the ultralow hole-doped insulating state, before the onset of pseudogap and emergence of Fermi surface, challenges the momentum space picture. It's conceivable that the stripe crystal phase serves as the reference insulating state. In this scenario, further hole doping will close the charge transfer gap by nucleating the inherently nematic low-energy quasiparticles states, which are unstable to the formation of incommensurate charge and other intertwined orders associated with the pseudogap. This is consistent with the underlying commensurate nature of the charge order throughout the pseudogap phase, disentangled from the apparent incommensurate, doping dependent vector[81].

4.5 APPENDIX

4.5.1 RHEED characterization

Using a 15 keV RHEED gun, we acquire RHEED patterns on the Bi-2212 surface as shown in **Figure 4. 5. 1** and **Figure 4. 5. 2**. Our RHEED patterns at different angles look identical to previously published work. Through the different temperature annealed Bi-2212 surfaces, we cannot see any new emergent features along any high-symmetry directions. The patterns due to the $4a_0$ surface reconstruction should be observable in the RHEED pattern as denoted by the red arrows in the 45-degree and 135-degree angle (**Figure 4. 5. 1** and **Figure 4. 5. 2**.B). However, there are no new streaks at the position labeled out. It's reasonable to rule out that the $4a_0$ charge stripe we observed on the 380^{o}C annealed Bi-2212 surface is from the surface reconstruction.

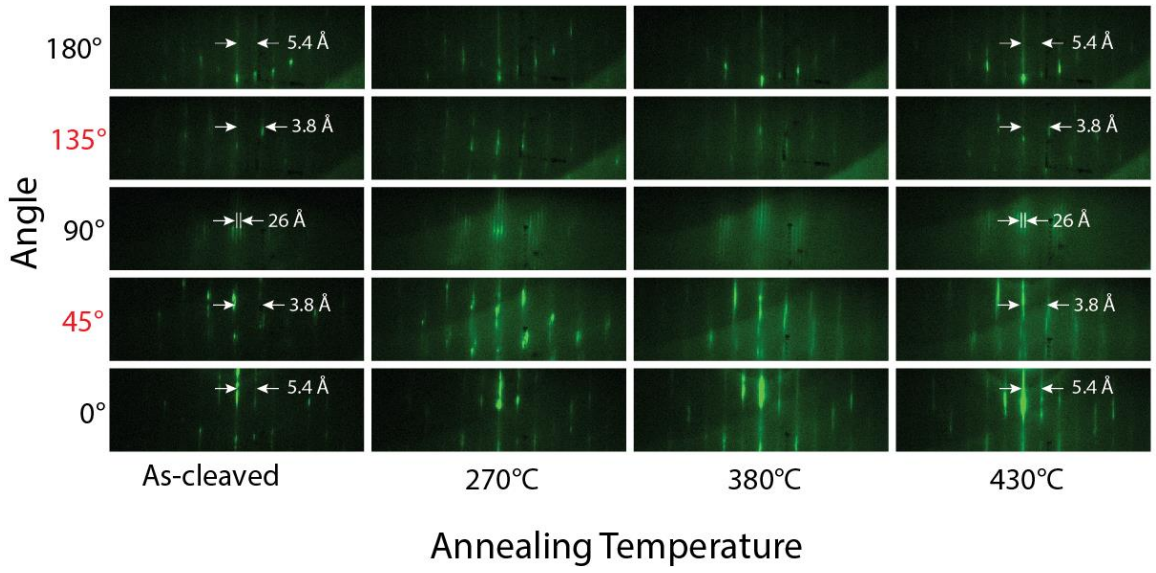

Figure 4. 5. 1. Angle (rows) vs. annealing temperature (columns) RHEED images acquired using a 15keV electron gun. All images are taken on the surface of the same optimally-doped Bi-2212 crystal (T_c ~ 91K), cleaved in UHV, annealed for 30mins at temperature denoted in the column labels, and cooled back down to room temperature where the RHEED data was taken. The real-space lattice periodicities corresponding to the reciprocal-space distances imaged are denoted by white arrows. No change in the RHEED pattern is observed up to the highest annealing temperature used. Surface reconstruction with ~ 4a0 period would be detected at the 45-degree and 135-degree angles. Reprinted from our work, ref. 78.

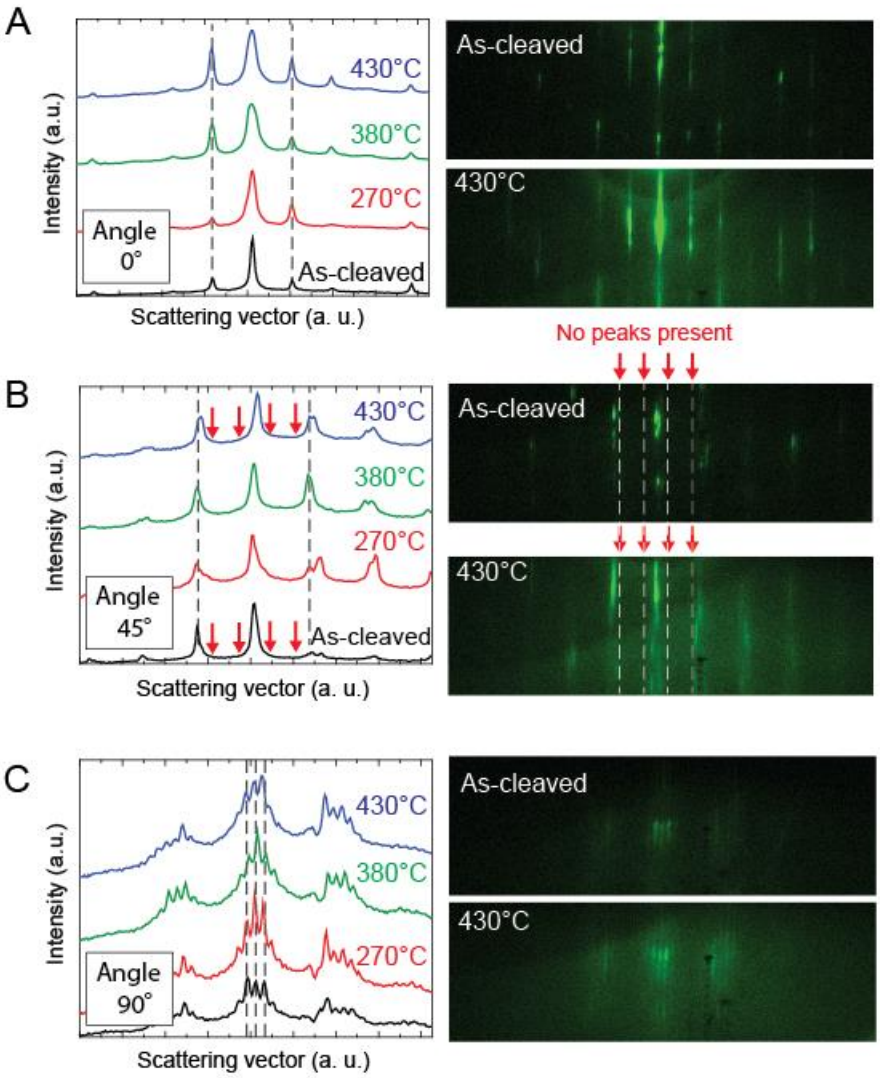

Figure 4. 5. 2. RHEED images and the intensity profile linecuts associated with the three inequivalent high-symmetry directions: (A) 0° showing the $\sqrt{2}a_0$ real-space period, (B) 45° showing the a_0 period, and (C) 90° showing the Bi-2212 superstructure with 6.5 a_0. All of the profile intensity linecuts are taken along a horizontal line, perpendicular to the long streaks seen in the RHEED images on the right. Reprinted from our work, ref. 78.

4.5.2 The effect of the superconducting bulk on STM surface measurements

As shown in **Figure 4. 5. 3**, the electronic property of our UHV annealed sample is different on the sample surface from the interior of the Bi-2212 crystal. We achieve a sample that has an insulating surface state but with SC bulk state. It's generally accepted that STM can detect the property of the topmost layer of the sample, which suggests that the electronic property exclusively in the bulk could be hard to be measured. In Bi-2212 for example, STM can detect the electronic signal from O dopants near the topmost BiO and SrO planes (above the first CuO_2 plane), but not the equivalent dopants below the second CuO_2 plane[73]. To rule out that the observed charge stripe in the insulating surface is a trivial result of tip measuring the charge order of SC bulk, we point out the following:

If these higher-doped, either superconducting, or possibly in the metallic pseudogap phase layers indeed contribute to the tunneling current measured by STM, we would expect to see the residue conductance near Fermi level in *dI/dV* spectrum. Insensitive to conducting bulk states can also be confirmed that our tip keeps injecting into the surface after Bi-2212 was annealed at even higher T; Based on previously published work and charge order measured on our non-annealed OP Bi-2212 and the same sample after annealing at 270^{o}C, the charge order is usually detected at approximately $\pm 100 - 150\ meV$ away from the Fermi level. At these energies, we don't measure any *dI/dV* signal and of course no Qco order which only emerges at high energies. Additionally, Q* in raw *dI/dV* maps in bulk UD Bi-2212 is reported to increase to ~ 0.3 Q_{Bragg} at 6~7% hole density, while our charge ordering vector observed at the surface in the insulating

state is exactly 0.25 Q_{Bragg}. Also, the charge stripe order of our insulating surface centers on Cu atoms while the charge order from the pseudogap bulk sample center on the Cu-O bond. For those reasons, the Qco order we measured in the insulating surface cannot be a simple visualization of the charge order in UD Bi-2212 below the insulating surface.

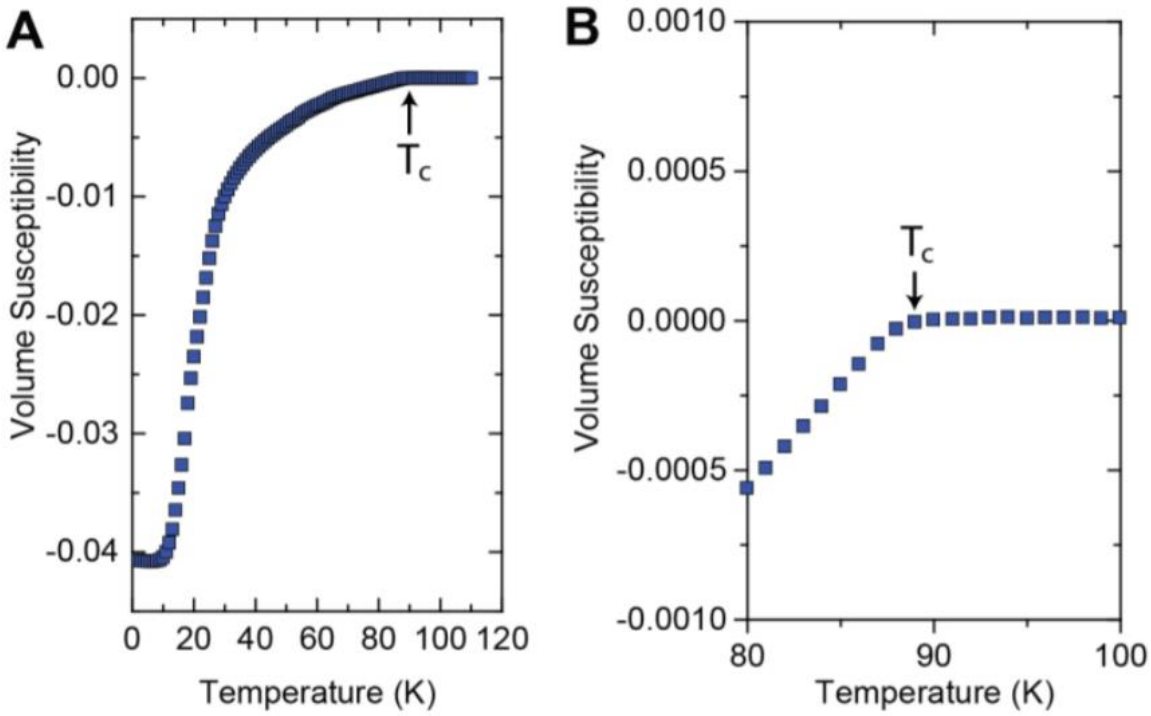

Figure 4. 5. 3. Zero field cooled (ZFC) magnetic susceptibility measurements of post-annealed Bi-2212 samples over: (A) 120K temperature range and (B) 20K temperature range around the superconducting transition. Although the *dI/dV* spectrum of 380^{o}C annealed sample shows an insulating feature, the onset of magnetization (~89K) is still approximately the same as before annealing (~91K). Reprinted from our work, ref. 78.

4.5.3 Distribution of oxygen dopants as the possibility to form the charge order in the annealed underdoped Bi-2212

Here we discuss the possibility that the observed charge order on surface annealed underdoped Bi-2212 is formed by the oxygen dopants. Oxygen dopants in bulk underdoped Bi-2212 don't show any ordering with a periodicity of ~ 4a0 except that the type-A O dopants order with the supermodulation wavelength. And the underdoped Bi-2212 is achieved after annealing at much higher T ~ 550oC in vacuum over a long term (~ days) to remove the interstitial oxygen dopants. So it's unlikely that those O atoms can order after a short time and low T annealing since even much higher T and longer time annealing process cannot make O dopants to order. To rule out the possibility that the oxygen atoms on the annealed Bi-2212 surface can form order, we image the three types of dopants (**Figure 4. 5. 4**). However, the distribution of the dopants doesn't show ordering by either eye or FTs of extracted dopants location maps (the bottom two rows in **Figure 4. 5. 4**). Notably, we can still see the peaks located close to Q^{SM} peaks in the FTs of the extracted type-A oxygen dopants maps from both annealed samples, similar to what the ref. 82 observed, which supports the similarity of phenomena of surface annealed vs bulk annealed sample. Although we don't observe the distribution of the dopants over the ultra-low doped sample, considering the fact that the oxygen cannot order on both lightly surface doped (annealed at 200^{o}C~300^{o}C) and bulk doped (annealed at ~550^{o}C) samples, it's reasonable to expect that the oxygen dopants would not order on the surface of the sample annealed at ~380^{o}C.

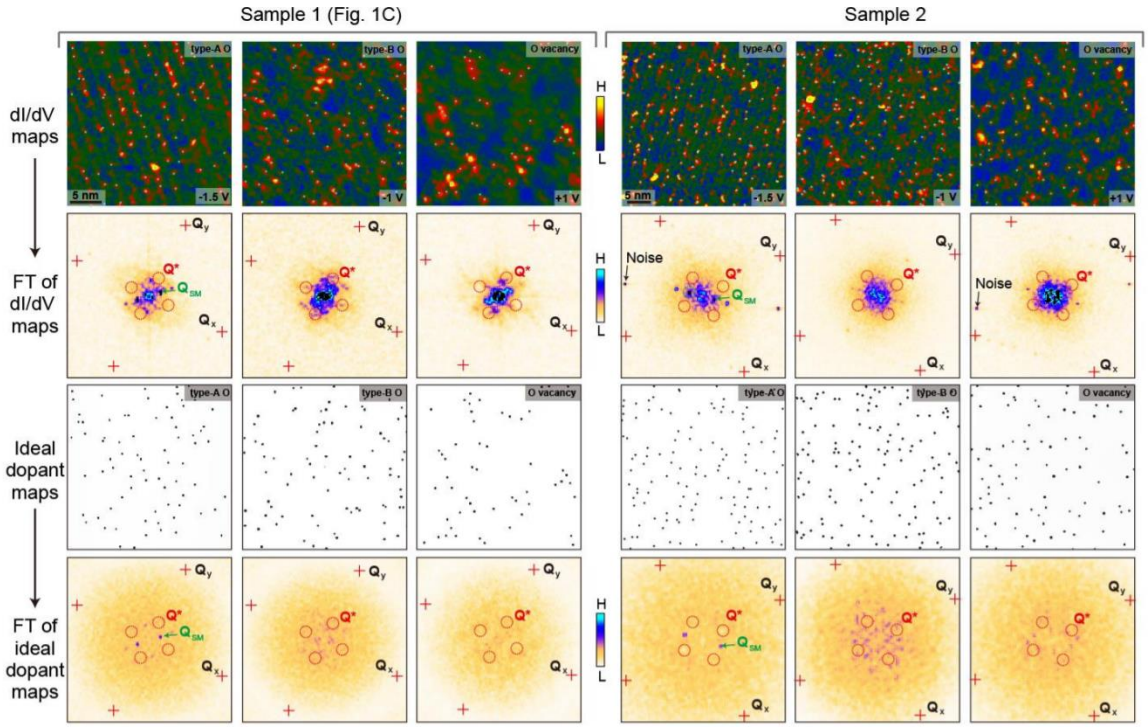

Figure 4. 5. 4 Nanoscale imaging of three types of oxygen dopants over two lightly doped cuprates samples. The top row displays the dI/dV maps presenting three types of oxygen dopants distribution. Blue dots are the superimposed oxygen dopants locations. 2nd row shows the associated FT images of each dI/dV map. Qx(y) peaks denote the Bragg peaks of the top Bi square lattice, QSM peaks correspond to the supermodulations and Q* peaks indicate the charge stripe order. The 3rd row presents the extracted dopants' positions maps from dI/dV maps and the bottom row shows the corresponding FT images. Reprinted from our work, ref. 78.

5 ATOMIC-SCALE MAGNETISM MELTING IN IRIDATES

5.1 INTRODUCTION TO THE RUDDLESDEN-POPPER(RP) IRIDATES: $Sr_{N+1}Ir_NO_{3N+1}$(N=1, 2, AND ∞)

As we have briefly introduced in chapter 1, RP-iridates have strong spin-orbit coupling, comparable with Coulomb interaction, so that the SOC here plays an equivalently important role in forming the electronic structure as the **Figure 5. 1. 1.** shows. The $5d^5$ band could be finally modified to form an insulator as **Figure 5. 1. 1** (e) described and the insulating gap opens as a result of the combined effect of SOC and U. However, there is much debate over whether the correlation effect induced gap in the simplest R-P $Sr_{n+1}Ir_nO_{3n+1}$ at n=1, i.e. Sr_2IrO_4. is Mott or Slater type. For a typical Slater insulator, a gap is induced by the magnetism when T lowers than T_N, and some works support this scenario explaining the property of Sr_2IrO_4[83, 84]. However, other works found that the induced insulating charge gap magnitude is much larger than the magnetic energy[85, 86]. As criterion− insulating gap still opens at $T > T_N$ for Mott insulator− is not valid for 2D systems because of the sizable short-range magnetic order persisting up to high T, there is no sharp border between 2D Mott insulator and Slater insulator.

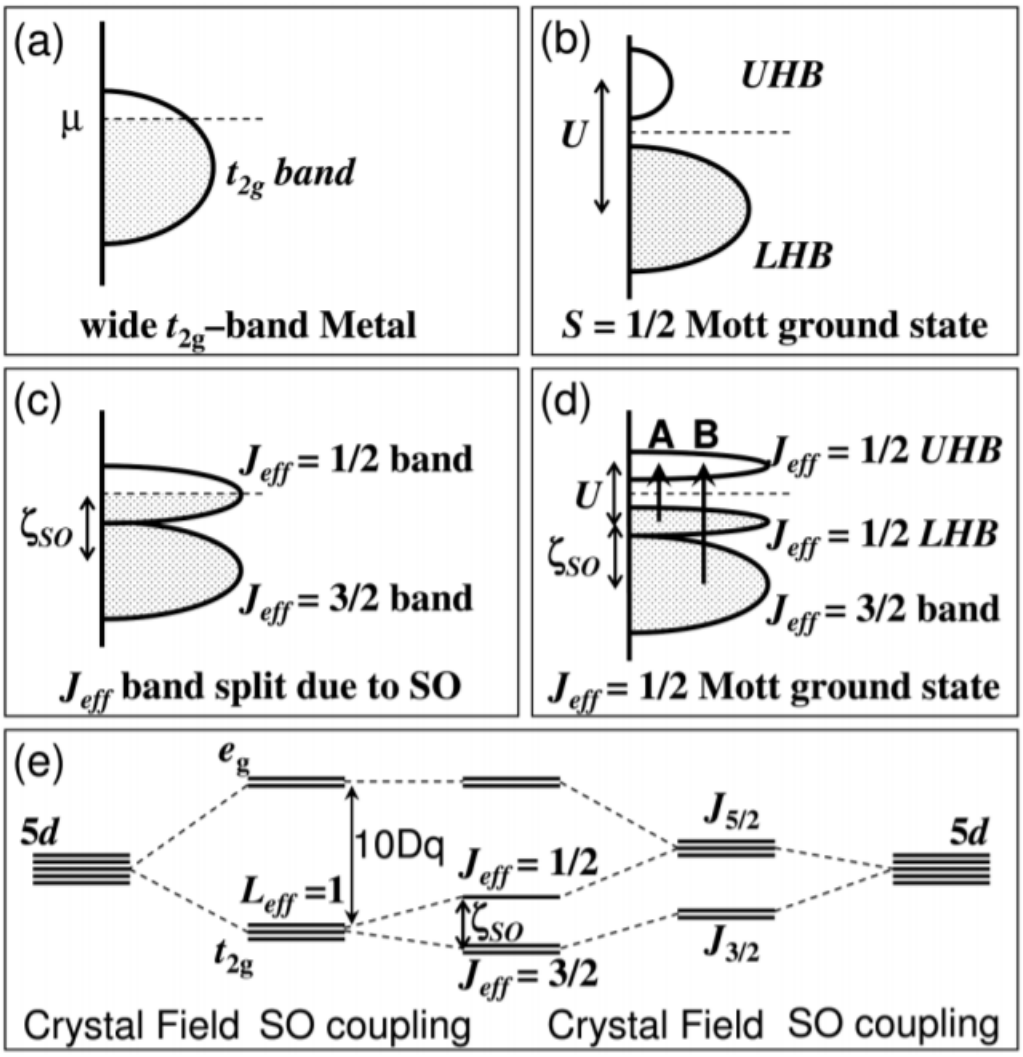

Figure 5. 1. 1. Schematic energy diagram of crystal field tuned $5d^5$ band (a) without considering SOC and U, (b) with a large U. (c)t_{2g} band splits into $J_{eff=1/2}$ and $J_{eff=3/2}$ with only SOC, and (d) the crossing fermi level $J_{eff=1/2}$ band splits further into occupied valence band and unoccupied band due to the existence of onsite U. (e) The overall *5d* band evolution due to the existence of crystal field, SOC and U. Figure is reprinted from ref. 87.

5.1.1 Magnetism of $Sr_{n+1}Ir_nO_{3n+1}$(n=1, 2, and ∞)

In Sr_2IrO_4, the magnetic ordering is canted in-plane AFM following the staggered rotation of the oxygen octahedral(~12°) with T_N ~240K, as illustrated in **Figure 5. 1. 2** and **Figure 5. 1. 4**(a). However, the moment directions of $Sr_3Ir_2O_7$ are different, forming a collinear arrangement perpendicular to the Ir planes with T_N ~285K, as shown in **Figure 5. 1. 2**. The 'zigzag' moment with T_N ~18K, which is much lower than the prior two iridates, forms the AFM order of Na_2IrO_3 when n=∞.

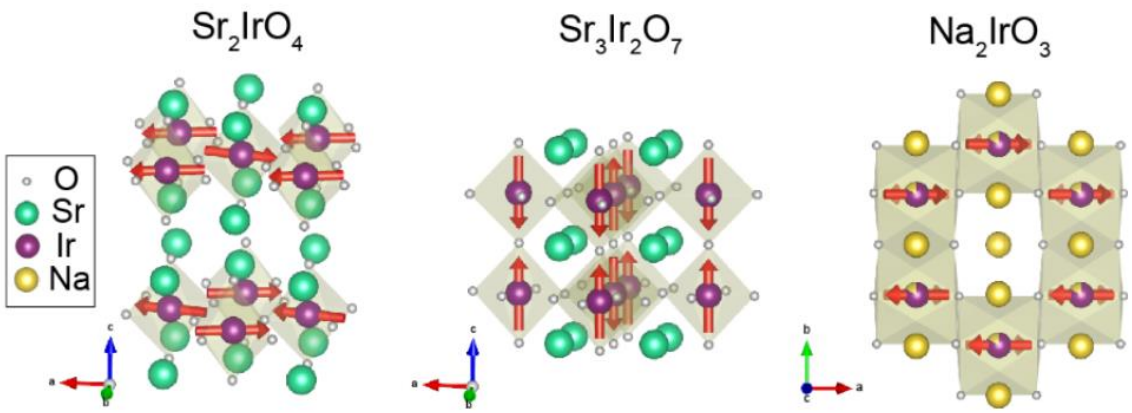

Figure 5. 1. 2. Atomic structure of three representative R-P Iridates with n=1, 2, and ∞. The arrows in each panel display the magnetic moment directions.

5.1.2 Brief introduction of electron-doped Sr_2IrO_4

As electrons are doped into Sr_2IrO_4, lots of arising properties, identical to the hole-doped cuprates, make this system more interesting. They exhibit the same electronic phenomena, such as pseudogap[88, 89, 90], fermi arcs[91], and incommensurate spin density waves[92]. Though the superconductivity state is still elusive, electron-doped Sr_2IrO_4 share almost the same phase diagram with hole-doped cuprates, as illustrated in **Figure 5. 1. 3** upper panels. In contrast to hole-doped cuprates, where the AFM gets suppressed strongly at p~0.05, the AFM order is still not quenched in electron-doped Sr_2IrO_4 even at doping level p~0.12. Additionally, STS detects that the doped electrons are bound to the dopants while the background clean area is still insulating when the doping level is low (**Figure 5. 1. 4** (e, f)). As the doping increases further, a sudden heterogeneous collapse of the mott gap occurs, and nanoscale metallic puddles nucleate around intense dopants area[88]. The coexisted long-range AFM order also gets suppressed and develops to a short-range AFM ordering with the dopants increasing, as shown in **Figure 5. 1. 5** bottom panel. Accompanying the MIT at around La~4%, the short-range AFM order undergoes a transition to an inhomogeneous spin density wave state as observed by neutron scattering[33].

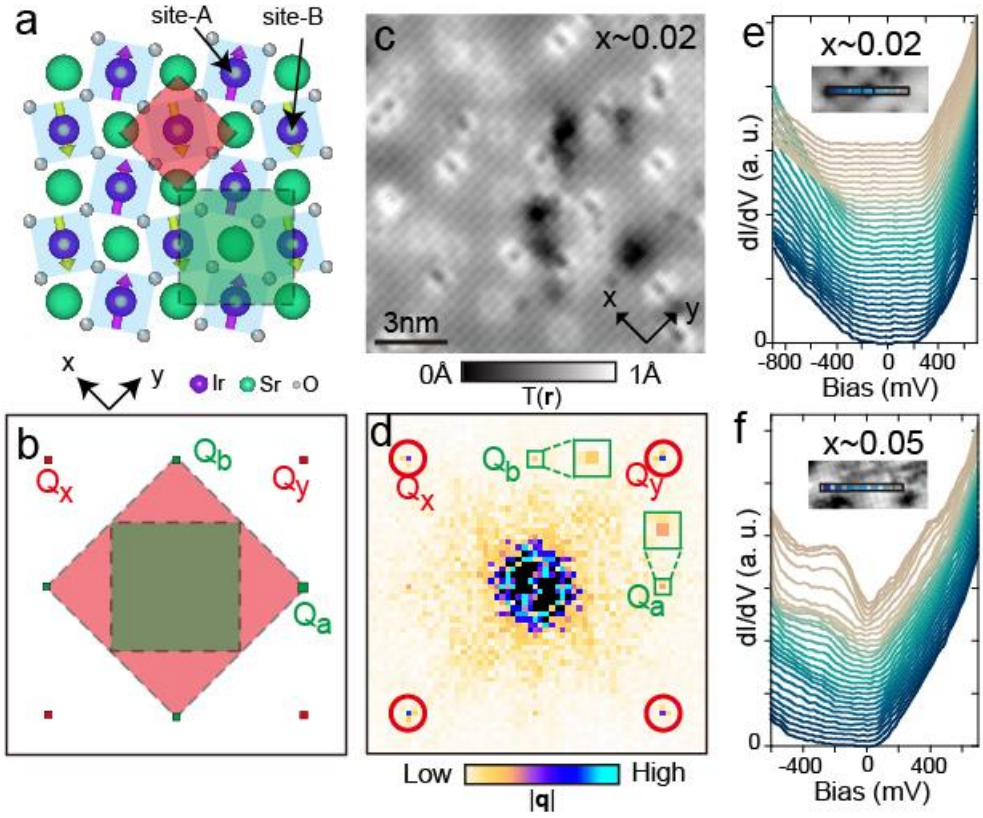

Figure 5. 1. 4. Crystal structure and basic electronic properties of $(Sr_{1-x}La_x)_2IrO_4$. (a) Crystal structure of Sr_2IrO_4 (Sr-214) in the xy plane. Green balls represent Sr atoms, purple balls are Ir atoms and small gray are O atoms. The arrows indicate the moment directions of local magnetic moments. Both the Sr atomic unit cell (pink square) and the unit cell of superstructure due to the octahedral IrO6 (green square, also magnetic structure) are shown. (b)The expected FT of the Sr-214 STM topograph. Pink and green squares represent the 1st Brillouin zone of atomic structure and superstructure, respectively. $Q_{x(y)}$ peak indicates the Bragg peak along x(y) direction, $Q_{a(b)}$ represent the collinear AFM ordering peaks. (c) The representative STM topograph of La-doped Sr-214 and (d) the associated FT of the topograph obtained using W tip. Those bright squares denote the La substitutions on the surface. A series of dI/dV spectra acquired on the surface of (e) x~0.02 and (f) x~0.05 La-doped Sr-214 along the line shown in each inset. Reprinted from our work, ref. 109.

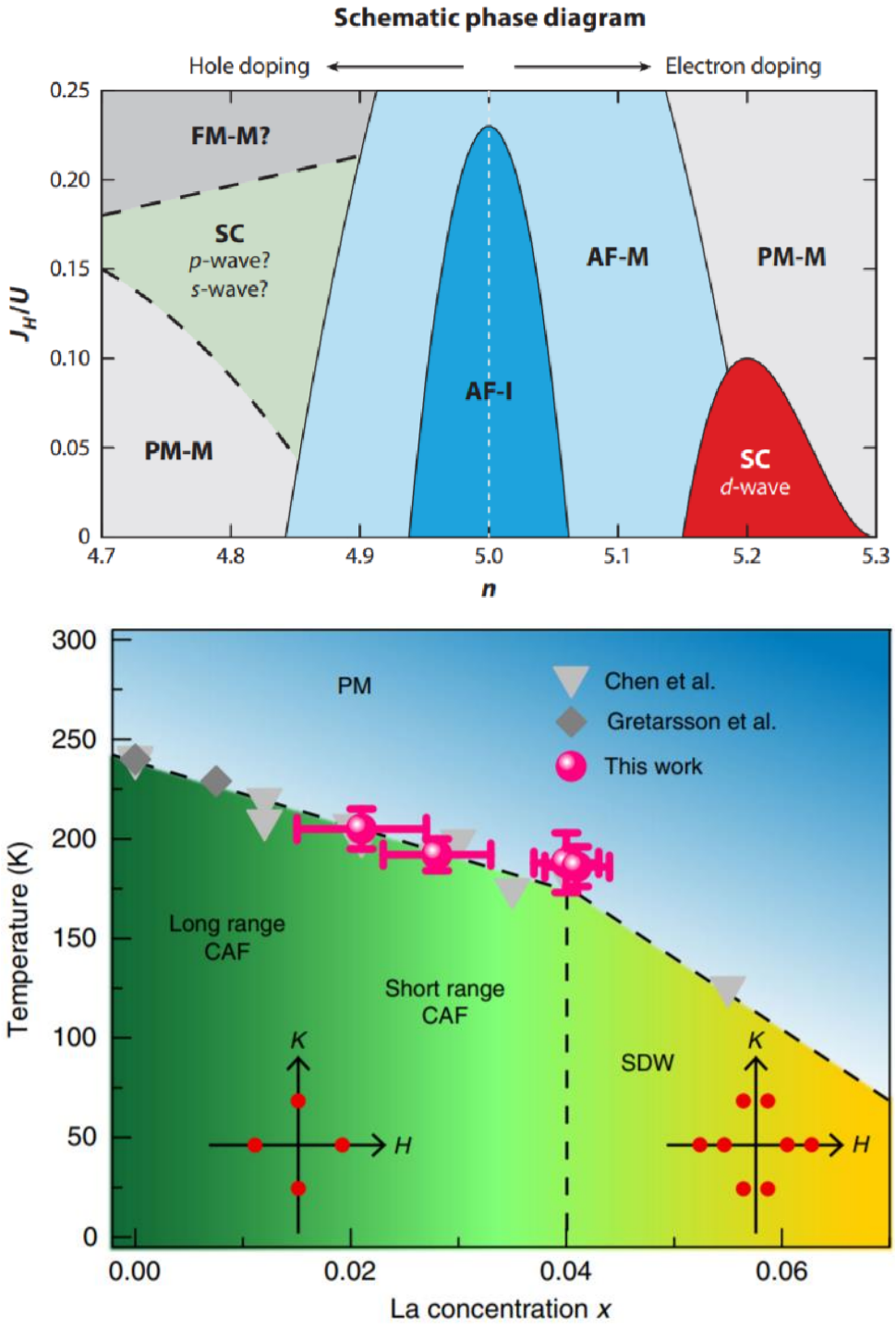

Figure 5. 1. 5. Phase diagram of $(Sr_{1-x}La_x)_2IrO_4$. The upper panel presents a variety of phases appear, such as an AFM insulator(AF-I) and metal(AF-M), a paramagnetic metal(PM-M), as well as two SC phases. The bottom panel displays the zoom-in of the low electron doping. With La dopants(electron doping level) increasing, the long-range canted AF(CAF) evolves to short-range CAF and finally to metallic unidirectional spin density wave (SDW) state when x larger than 4%. Figures credit to ref. 38, 92.

5.2 BULK CR TIP PREPARATION AND CHARACTERIZATION OF THE SPIN-POLARIZED TIP ON $Fe_{1+Y}Te$

To map the AFM order in iridates, we etch the bulk Cr wire electrochemically to prepare a spin-polarized tip firstly with 2 mol/L NaOH solution. As the Cr single crystal is an AFM material, its stray field should be ignorable and only the apex Cr atom's magnetic moment matters so that it could be used to make one of the ideal spin-polarized tips. After the tip etching, we transfer it into the UHV chamber and anneal the tip head to remove the oxidization of Cr. Prior to applying the Cr tip for measuring the magnetic sample (iridates), we have to characterize the polarization of the tip on top of $Fe_{1+y}Te$.

$Fe_{1+y}Te$ is also an AFM material but with bi-collinear magnetic order, as shown in **Figure 5. 2. 1**(c). With a spin-polarized tip, the scanned topograph should display a diagonal double stripes pattern (**Figure 5. 2. 1**(c)) with a 2a0 period and the Fourier transformed image should be able to detect the AFM peaks as well. To achieve sufficient sensitivity and atomic resolution of the annealed Cr tip, we change the annealed Cr tip *in-situ* by fast scanning over Fe impurities and/or pulsing the tip with several Volts on $Fe_{1+y}Te$. This process can lead to the rearrangement of Cr atoms in the apex, and in the tip head picking up some Fe atoms or a small piece of $Fe_{1+y}Te$ sample. To check the magnetic moment of tip apex switchable at different magnetic fields, we scan topographs on top of the $Fe_{1+y}Te$ surface after applying 2T (**Figure 5. 2. 1**(a)) and -3T (**Figure 5. 2. 1**(b)) at exactly the same field-of-view. Consistent with the AFM scenario in $Fe_{1+y}Te$, both of the topographs present DDS with a 2a0 period besides the clear topmost Te atoms and clear AFM order peaks located at 1/2 $\mathbf{Q_{Bragg}}$ can be seen in FTs. Similar to the procedure described in ref. 93, we obtain a magnetic contrast (M(r)) map (**Figure 5. 2.**

1(c)) by subtracting the two topographs and a magnetic average (N(r)) map (**Figure 5. 2. 1**(d)) by adding up the two topographs. The M(r) map is expected to display only the magnetic order signal changed by B but no atomic structural information, which is consistent with the only spin polarization being different, while the N(r) map is opposite, which is consistent with the spin-related information canceling out by different B. Experimentally, the 2a0 DDS pattern can be detected by the Cr tip in the M(r) map (**Figure 5. 2. 1**(c)) and correspondingly DDS related 1/2 $\mathbf{Q_{Bragg}}$ peaks without Bragg peaks can be seen in the FT (**Figure 5. 2. 1**(g)). In contrast, N(r) map (**Figure 5. 2. 1**(d)) presents clear topmost Te square lattice, and FT of N(r) shows only Bragg peaks but no others. This is consistent with the scenario that our tip polarization could be switched by a different magnetic field.

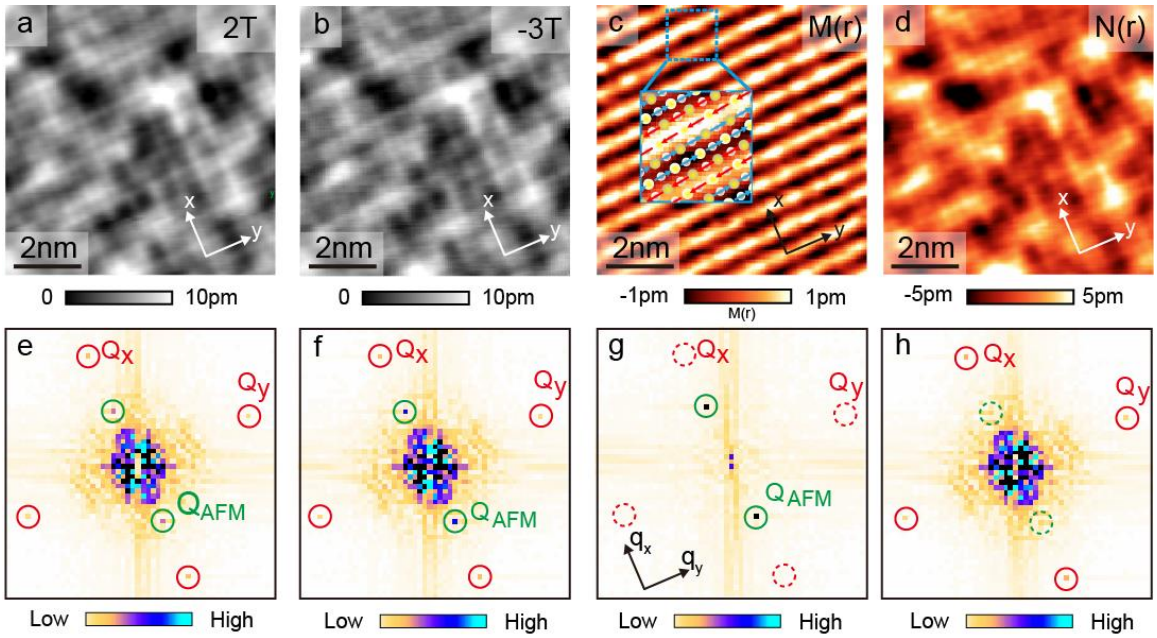

Figure 5. 2. 1. Characterization of Cr tip on top of $Fe_{1+y}Te$. The STM topographs acquired at (a) 2T and (b) -3T using a Cr tip. The minus sign means the magnetic field direction is reversed which is always applied perpendicular to the sample surface. (e, f) FTs of the topographs (a, b), respectively. Green circled peaks are the additional peaks arising from the bi-collinear AFM order. (c)The spin contrast (M(r)) map obtained by subtracting (a) and (b), the inset of which is the atomic ball model of the topmost Te (light yellow balls) and Fe(gray balls) and the second Te layer (dark yellow balls) overlayed on topograph. The arrows indicate one of the possible AFM order scenarios showing the local magnetic moment. And (d) the spin average (N(r)) map obtained by adding (a) and (b) topographs. (g) FTs of the M(r) and N(r) map, respectively. Setup condition: (a, b) V_{sample} = 700 mV, I_{set} = 100 pA. Reprinted from our work, ref. 109.

5.3 COLLINEAR AFM ORDER AND ELECTRONIC PROPERTIES OBSERVED ON ELECTRON-DOPED $(Sr_{1-X}La_X)_2IrO_4$

5.3.1 Magnetic order on low electron-doped $(Sr_{1-x}La_x)_2IrO_4$

After the characterization of Cr tips on top of $Fe_{1+y}Te$, we apply the tip to measure the topographs on low La-doped Sr-214 firstly. Based on neutron scattering results, one is expected to be able to detect the magnetic order signal at $Q_a = (1/2, 1/2)$ and $Q_b = (1/2, -1/2)$ on Sr-214. To map the AFM ordering in La-doped Sr-214, we scan the topographs over the same field-of-view with the same magnitude (**Figure 5. 3. 1**(a, b)) but varying directions of the magnetic field, which is always perpendicular to the sample surface, while keeping all other setup scanning conditions constant. As the magnetic moment on Sr-214 is in-plane and polarization of Cr tip is typically canted in 3D space, with both in-plane and out-of-plane component even at zero B, the varying magnetic field could change the overlap between an in-plane component of polarization of tip and moment of Sr-214, which in turn modulates the measured electronic signals at Q_a and Q_b. The FT of topographs measured using a spin-polarized tip shows a systematic evolution of Q_a and Q_b (**Figure 5. 3. 1**(g)). As the nearest exchange energy scale is much larger than the Zeeman energy due to B, the applied field is expected to be able to only vary the spin polarization of Cr tip but not affect the magnetic moment of sample[94]. Similarly to measurement using Cr tip, we repeat the procedure above with spin averaged W tip, and the intensity of each peak in FT of topographs shows no dependence on the magnetic field.

To map the spin-resolved magnetic modulation, firstly we apply the Lawler-Fujita algorithm[95] to the topographic images taken at opposite directions B to align them (**Figure 5. 3. 1**(a, b)), using those green circled La dopants to mark the positions. Similarly to the procedure described in ref. 96, the spin-resolved magnetic contrast (M(r)) map is obtained by subtracting topograph at 3T (**Figure 5. 3. 1**(a)) by the -3T one (**Figure 5. 3. 1**(b)) and the magnetic average (N(r)) map is by averaging those two topographs, which is expected to cancel out all of the spin signals but only structural information is left (**Figure 5. 3. 1**(e)). And the FT image of M(r) map shows narrow single-pixel centered peaks at (1/2, 1/2) and (1/2, -1/2), which are 45 degrees with respect to the Sr lattice, consistent with the scenario that lightly La-doped Sr-214 has a long-range AFM order established by neutron scattering measurements[33]. We should note that the STM topographs are the integral of DOS from E_F to the voltage we set (500mV to 700mV). As introduced above, the spin-orbital coupling separates the t_{2g} band into $J_{eff=1/2}$ and $J_{eff=3/2}$ orbitals with the $J_{eff=1/2}$ crossing E_F but $J_{eff=3/2}$ and other bands are far away[97]. Therefore, our topographs are mainly mapping the electronic properties of $J_{eff=1/2}$ orbital, indicating that the M(r) map is tightly associated with $J_{eff=1/2}$.

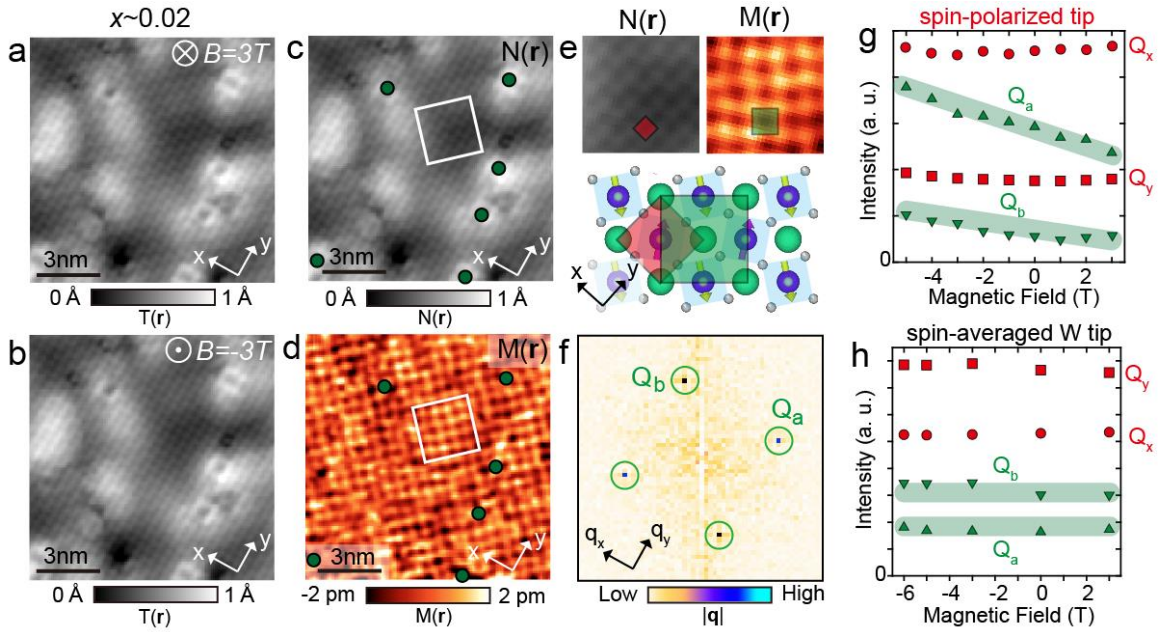

Figure 5. 3. 1 Spin resolved magnetic contrast modulation in low electron-doped Sr-214. STM topograph taken at (a)3T and (b)-3T field over identical field-of-view using characterized spin-resolved Cr tip (minus sign indicates the reversal magnetic direction from the positive field). (c) The spin averaged (N(r)) map by adding up topographs in (a,b) which is expected to cancel out the spin signal change due to the different B but only display atomic structure. (d) The spin contrast (M(r)) map by subtracting topographs in (a,b) showing only AFM ordering modulation. The green dots label La substitutions. (e) Zoom-in on a small region outlined by the white square in (c, d), showing the atomic-scale structure of N(r) and M(r) maps. The pink and green small squares denote the atomic unit cell and unit cell of superstructure arising from the AFM modulation, respectively. (f) The associated FT image of (d). The extracted intensity of peaks in FT images of STM topographs using (g) spin-polarized Cr tip and (h) spin averaged W tip. Reprinted from our work, ref. 109.

5.3.2 AFM order melting in highly doped $(Sr_{1-x}La_x)_2IrO_4$

To study the effect of higher electron doping over the evolution of AFM order in Sr-214, we proceed to x~0.05 sample, which is closer to MIT, with repeating the similar measurements on x~0.02. Again, we obtain the M(r) and N(r) maps (**Figure 5. 3. 2**(c, d)) with topographs at varying fields (**Figure 5. 3. 2**(a, b)). Interestingly, consistent with magnetization measurements at this approximate doping level, the M(r) map on x~0.05 La-doped Sr-214 sample displays fragmented magnetic contrast modulations even within a 10 nm region. That fragmentation can be classified into three types of modulation domains based on their magnitudes and phases (**Figure 5. 3. 2**(d)): the domain III denotes area with a much smaller magnitude of modulation, domain I and II modulations have comparable amplitudes but with a pi phase shifting between each another. As the phase diagram is shown above, the paramagnetic phase should appear at an even higher doping level. Therefore, it's reasonable to interpret the domain III as the arisen paramagnetic state. The FT image of the M(r) map also presents the broader peaks around Qa and Qb in contrast to single-pixel peaks detected on x~0.02 samples, which means the long-range AFM order melts into short-range fragmented ordering at high doping level. To exclude the effect of STM tip and other experimental parameters on the short-range order, we show M(r) map of other samples, acquired using other Cr tip and different magnitudes' magnetic field, that exhibit qualitatively the same behavior, as shown in the sample #2 of **Figure 5. 3. 2**. The auto-correlation of M(r) over a larger FOV (**Figure 5. 3. 2**(g)) gives the correlation length ~ 5nm. By constructing the magnetic contrast modulation amplitude map, we visualize the local strength of the magnetic

correlation, which highlighted the fragmented nature of the state, with ordered puddles varying in size from ~10 to 100 IrO_6.

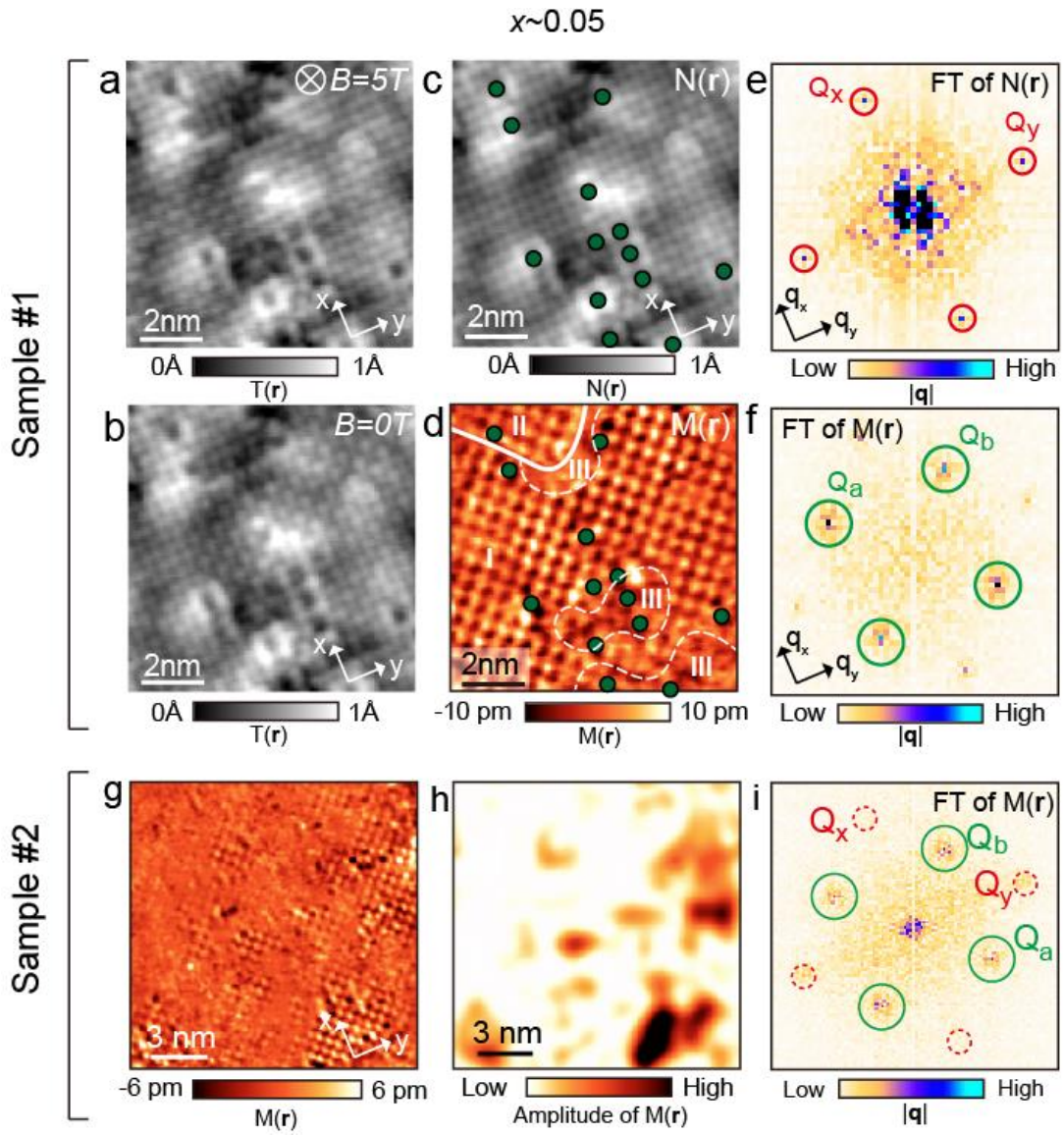

Figure 5. 3. 2. The fragmented magnetic contrast pattern in x~0.05 sample. Sample #1: The STM topographs taken at (a) 5T and (b) 0T over the same FOV. (c) The N(r) map and (d) M(r) map obtained by averaging and subtracting the two topographs, respectively. Green dots mark those La dopants. In panel (d), the white curves outline the AFM domains observed by the eye. (e, f) FT images of (c) and (d), respectively. Sample #2: (g) M(r) map acquired by subtracting two topographs at +/-0.5T. (h) The associated magnetic amplitude map by Fourier filtering through only Qa and Qb peaks in (h), the FT image of (g). Reprinted from our work, ref. 109.

5.3.3 Correlation between fragmented order and electronic property

As the magnetic properties of Sr-214 have been studied, finally we proceed to study the relationship between magnetic and electronic structures. On top of low doped Sr214, we can always observe a U shape (or hard gap) insulating Mott type *dI/dV* spectrum everywhere. However, the spectra vary crossing the sample even in atomic-scale and they typically can be divided into two types: one is still U shape Mott type another shows a V-shape (or small gap) pseudogap. To quantify the electronic structure, we acquire the *dI/dV* spectra on a dense space grid map and extract the approximate gap magnitude distribution (Δ(r) map (**Figure 5. 3. 3**(b)) over the same FOV as M(r) map (**Figure 5. 3. 3**(c)). The theoretical calculations indicate that the gap opened in the insulating state should scale with the strength of magnetic order [97]. For an insulating sample where AFM state is the only ordered state, the AFM ordered regions should present large Δ(r) and Mott like spectra, but as the AFM order collapses, the gap also shrinks. Surprisingly, we find that there is no cross-correlation between AFM modulation magnitude and gap magnitude distribution (**Figure 5. 3. 3** (f)). Such a conclusion can also be verified by visual inspection of **Figure 5. 3. 3**(a-d). For example, the local short-range magnetic contrast modulated regions (solid blue and black squared) can display both U-shape Mott like and V-shape insulating gap spectra and so do those weakly magnetic modulated areas (dashed blue and black square).

Therefore, our experiments point out that only the AFM order is unlikely the only culprit behind the inhomogeneous gap closing mechanism near the MIT. The residual gap could be due to the pure Mott charge gap in the weak Mott state, but we deem this possibility

unlikely given the high electron doping and proximity to dopants. This brings a surprising possibility suggestive of another, 'hidden' order that may be contributing the gap modulation[98], or the existence of spin-orbit density wave theoretically proposed by ref. 97. The latter is an intriguing possibility as it can in principle modulates the gap at the X point by ~200meV, which can explain the correlation between the electronic structure and the AFM we found. It remains to see which parameter controls the patchy distribution in the M(r) map, as the domains observed does not correlate with the distribution of La dopants in the topmost layer. The sublayer dopants may determine the ordered puddles distribution but we cannot detect that with STM.

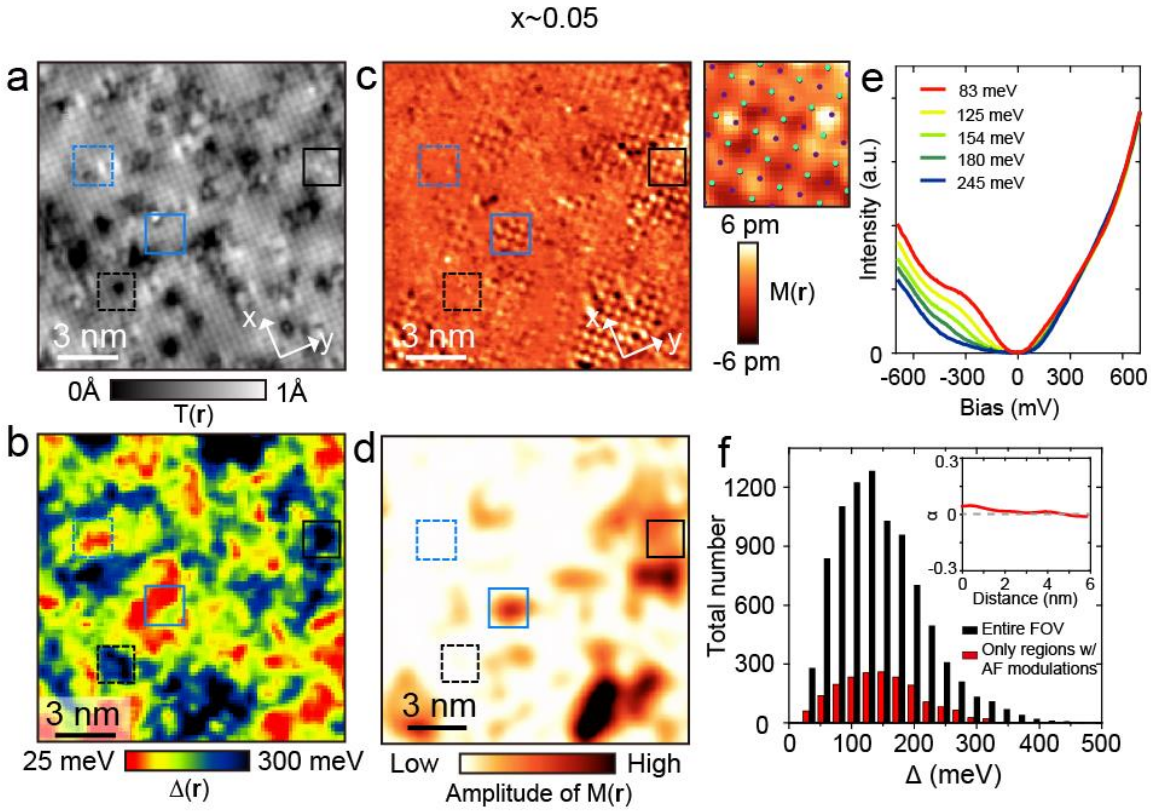

Figure 5. 3. 3 Relationship between melted AFM modulation and electronic structure on x~0.05 sample. (a) The N(r) map and (c) M(r) map obtained by arithmetic processing of topographs at +/-0.5T over the same FOV. (d) Associated modulation amplitude map of the (c). (b) Insulating gap size map over the same FOV as (a, c). (e) The binned average spectra by the gap size. (f) Statistics of gap size over the entire FOV (black columns) and only AFM modulation puddled areas, inset of which is the plot of the correlation between gap size map and magnetic modulation map. Reprinted from our work, ref. 109.

5.4 CONCLUSION AND DISCUSSION

Visualizing spin-resolved magnetic modulation using SP-STM, we detect the AFM order evolution from lightly (x~0.02) to heavily (x~0.05) electron-doped Sr-214 samples. In addition to the insulating-to-metal transition with doping varying (the U-shaped charge Mott like gap develops to a V-shaped pseudogap spectrum), the spin-resolved AFM modulation's transition from long-range order at low doping to a short-range, fragmented order at higher doping can be observed in Sr-214. However, in the short-ranged AFM modulation sample, the charge gap opening cannot be explained only by the local AFM order because of the lacking correlation between the magnitude of AFM modulation and gap opening size near MIT. Besides the inhomogeneous AFM order, some 'hidden' order can be another culprit to explain the gap, which can be measured in the future.

6 VISUALIZING SCALE-INVARIANT MAGNETIC STRUCTURE IN $(Sr_{1-x}La_x)_3Ir_2O_7$

6.1 INTRODUCTION OF BILAYER R-P IRIDATES: $(Sr_{1-x}La_x)_3Ir_2O_7$

We have briefly introduced the single layer R-P iridates−Sr_2IrO_4, the cousin of cuprate, in chapter 5 and it's one of the representative 5d Mott insulators but with strong spin-orbital coupling (SOC). The band structure of Sr_2IrO_4 is formed by a combination of multiple interactions and energies: Coulomb interaction (*U*), crystal field, the SOC, and bandwidth (*W*). However, these parameters undergo strong variations with the varying number of IrO_2 planes (the stoichiometric number n in $Sr_{n+1}Ir_nO_{3n+1}$), which is caused by the interlayer interaction between IrO_2 layers. For example, the *W* of the $J_{eff=1/2}$ band increases from 0.48 eV for n = 1, to 0.56 eV for n = 2, and 1.01 eV for n = ∞[99, 100] and concomitantly, the $Sr_{n+1}Ir_nO_{3n+1}$ undergoes a transition from strong Mott insulator (~0.6eV) for n = 1, to weak Mott insulator with much smaller charge gap (~0.18eV) for n = 2 and finally becomes a correlated metal with infinite n. Other than the electronic structural variations, the magnetic properties also get tuned by the strength of the interaction between layers driven by the dimensionality.

Chapter 5 has explored the single-layered Sr_2IrO_4, showing collinear in-plane antiferromagnetism with the magnetic moment on Ir atoms canting ~11° by following the structurally IrO_6 octahedral rotation. But its cousin, the bi-layered $Sr_3Ir_2O_7$(Sr-327), has a

much weaker moment with a magnetic easy axis along c[38, 101] (**Figure 6. 2. 1**). Such difference suggests a spin-flop transition as a function of the number of IrO_2 layers due to the strong competition among intra- and inter-layer bond-directional, pseudodipolar interactions [101], [102]. Considering the charge gap size reduces strongly (~fourfold), compared with single-layered Sr_2IrO_4, the $Sr_3Ir_2O_7$ should be a fortuitous starting point for perturbing the spin-orbit Mott phase by free carrier[103] and studying the magnetic order unstability.

6.2 THE PHASE DIAGRAM OF $(SR_{1-X}LA_X)_3(IR_{1-Y}RU_Y)_2O_7$

The Sr-327 has a collinear AF ground state persisting up to a high T_N ~ 285K, with the magnetic moment of Ir spins in Sr-327 orienting out-of-plane. The octahedral IrO_6 rotation and AF order lead to a doubling of the primitive unit cell of Ir cations (**Figure 6. 2. 1** (b)). Consistent with previous works on Sr-327[104, 105, 106], to get rid of the surface reconstruction, the Sr-327 needs to get cleaved at 77K, and following which we obtain the terminated surface with squared SrO layer having lattice constant a_0~ 0.39 Å, as shown in **Figure 6. 2. 1**.

As our earlier work on single-layered Sr-214 shows, the SP-STM has been proven to be a reliable tool to visualize the long-range AF order at the atomic-scale. Here we utilize bulk Cr tip, which is firstly characterized to be ferromagnetically polarized, on the well-known AF $Fe_{1+y}Te$, to take topographs of Sr-327 at different B (+/-8T) parallel to the c-axis over the same area (**Figure 6. 2. 1** (c, d)). The bright squares on top of topographs are the apical oxygen vacancies from IrO_6 octahedra. The B only tunes the orientation of the

polarization of the tip, whereas the magnetic moment intrinsic to the sample is robust to the external field. The polarization orientation of the tip can be flipped by switching the direction of the field so that the spin-polarized component of the tunneled current is expected to be removed by the sum of the two topographs (N(r) map, **Figure 6. 2. 1** (e)) with only structural signal left. While the subtraction between the topographs (M(r) map, **Figure 6. 2. 1** (f)) only smears out the structural modulation but keeps the information related to magnetism. Therefore, the modulations, with a periodicity ~ $\sqrt{2}$ a_0 and 45° rotated from Sr lattice, on the M(r) map should be due to the magnetic order in principle. After applying Fourier transform (FT) to the M(r) map, we can clearly detect peaks at Q_a = (−1/2,1/2) and Q_b = (1/2,1/2) (reciprocal lattice vector $2\pi/a_0 = 1$), but the FT image of N(r) map only presents Bragg peaks of structural SrO square lattice at Q_x = (−1,0) and Q_b = (0,1), supporting the collinear AF order scenario established by neutron scattering measurements[103] and resonant x-ray diffraction study[101, 102].

It's theoretically predicted that the Sr327 is at an intermediate phase between strong spin-orbit Mott (SOM) insulator and correlated metal phase with a weak AF order [38, 107]. And experimentally the coexistence of metallic puddles due to the locally dense Ru dopants with insulating background has been revealed[103, 104], and the IMT happens at the metallic cluster percolation threshold. As shown in **Figure 6. 2. 2**(j-l), a hard U-shaped gap (~130meV) can be observed from the spatially averaged *dI/dV* (r, V) spectrum in the pristine Sr327, it starts softening with Ru doping setting in and finally a metallic states with V-shaped spectrum appears crossing IMT boundary. The neutron scattering measurements observed the long-range AF order (>20 nm) [104] close to IMT (~35% Ru doping) and such long-range order can persist to deep metallic phase. So the spectrum

evolution could not be explained by the hole doping induced softening of other underlying orders, apparently the AF order.

To visualize this picture at atomic resolution, we perform the SP-STM measurement over Ru-doped samples. As performed on pristine Sr327, we acquire the M(r) maps over the 29% (**Figure 6. 2. 2** (b)) and 40% (**Figure 6. 2. 2** (c)) Ru doped Sr327 samples by applying different B. And all of the $Q_{a(b)}$ peaks located at (± 1/2, ± 1/2) in the corresponding FT images center on the single pixel, which reveals the persistence of a robust long-ranged AF order even in the metallic regime. In contrast to the coherent magnetic contrast modulations, both the gap maps from insulating pristine Sr327 and 29% Ru-Sr327 display the inhomogeneity (**Figure 6. 2. 3** (k, l)). And the electronic inhomogeneous behavior continues even in the metallic 40% Ru-Sr327, showing a prominent spatially varying density of states (**Figure 6. 2. 3** (j)). Not considering effects from other possible hidden orders, the ref. 108 shows that the V-shaped spectrum developing from a U-shaped gap can be a result of disorder-induced power-law. If the disorder comes from the Ru dopants, we would expect to see a strong correlation between the distribution of dopants and the tunneling gap map. However, the Ru-dopant sites have not been locally detected through either spin averaged STM topograph imaging or conductance mapping. Even if Ru dopants carry strong enough spin due to local polarization, it would be difficult for the spin-polarized tip to catch the spin contrast, considering the topmost Ru dopants tightly residing in the IrO_2 plane, which locates at ~2Å further from tip apex than the terminated SrO surface. Therefore, we may need further experiments or other techniques to determine the relation between Ru doping induced disorder and the IMT driving mechanism.

Similar to our previous single-layered La-Sr-214 work[109], we explore the electron doping effect on the magnetism and spectral gap of bi-layered La-doped Sr-327 with Sr replaced. In addition to the pristine Sr-327, we focus on the sample with nominally ~3.4% Sr sites substituted by La atoms, thus each Ir atom is doped with ~0.051 electrons in average, which is expected to be dense enough to drive the Sr327 across the IMT (**Figure 6. 2. 2** (a)). We should note that the IMT happens in La-Sr327 with a lower electron doping density than half of that in the single-layered La-Sr214, reflecting the weakly spin-orbit Mott property of the Sr327 due to the interlayer coupling. Comparing the average spectra in pristine Sr327, we can observe the coexistence of metallic V-shaped and insulating U-shaped hard gap spectrum in 3.4% La-doped sample (**Figure 6. 2. 2** (h, i)). In contrast to the Ru dopants, the La dopants in the topmost unit cell can be identified by topographs and conductance maps. As introduced in ref. 105, each of the bright square on the topograph marks a La1 dopant from top SrO plane (**Figure 6. 2. 4** (e)), and the bright dots pattern in the conductance map near Fermi energy denotes the La2 dopants (**Figure 6. 2. 4** (b)) located in the middle SrO plane. Considering that the STM tip cannot detect the third SrO layer of the topmost unit cell due to the too large spacing, we approximately estimate the density of the third type of La by the number of La1 as they locate at the terminated surfaces intra a unit cell. By counting the number of La1 and La2 dopants over a small topography, we calculate the La doping density to be ~3.7%, which is within the error of 3.4%[105]. In addition to the bright squared La1 dopants on the topograph, there is another type of pattern, showing as dark spots which are marked as ‘dark’ dopant (**Figure 6. 2. 4** (a, f)). Although we cannot exactly make sure the component of ‘dark’

dopants, we guess they might be either Sr or La vacancies caused by cleaving. But it seems that they don't have a significant effect on the magnetic and electronic properties.

Like the magnetic melting phenomenon observed in our earlier work on 5% La-Sr214, the M(r) map of 3.4% La-Sr327 catches incoherent magnetic modulations (**Figure 6. 2. 2**(e)) even within a ~14 nm FOV, indicating the long-range AF suppressed. Interestingly, not unique to the single-layered La-Sr214, we find that the La-Sr327 also holds the uncorrelation between short-range magnetic order and charge gap magnitude near IMT. The 'hidden' order might be able to explain such a phenomenon as we proposed in single-layered Sr214. Or it's just because the electron-electron interaction plays an important role across IMT[103], making the charge gap in Sr327 not open simultaneously as the onset of AF order. Consistent with the behavior of La dopants in single-layered La-Sr214 (only one type of dopant), the La1 dopants, and 'dark' dopants in 3.4% La-Sr327 barely correlate with magnetic order. However, the La2 dopants density map from the middle SrO plane correlates moderately with the short-range AF order (**Figure 6. 2. 4** (c)) and most of the La2 dopants sit within the weakly ordered region (**Figure 6. 2. 4** (b))**.** We can speculate that the difference between dopants is related to their different densities. The low-density La1 dopants on top SrO surface are highly localized while the much denser La2 dopants are expected to contribute the free carriers flowing into the IrO_2 plane, which reduces the localization effect by screening the top SrO plane. The La2 dopant sites are much lower than Ru, but only the former dopants can be detected with STM measurement and show the correlation between magnetism and dopants distribution, which indicates that electrons from La are much more itinerant.

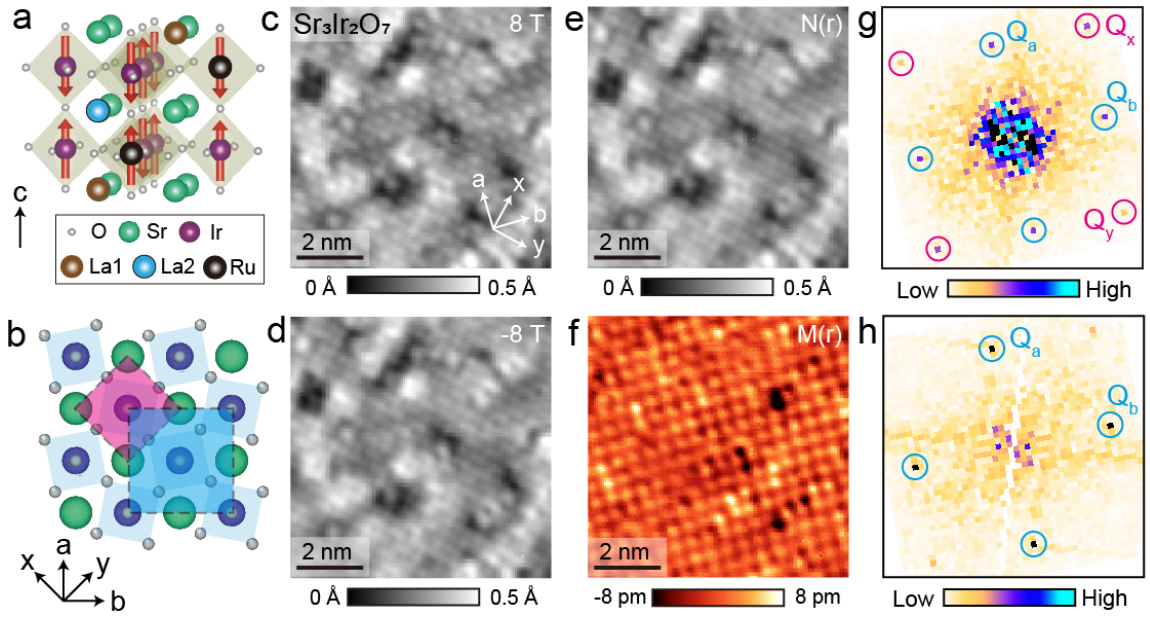

Figure 6. 2. 1 Parent $Sr_3Ir_2O_7$ characterized by the spin-polarized tip. (a) schematic of the atomic structure of parent $Sr_3Ir_2O_7$. The arrows on Ir atoms indicate the direction of the magnetic moment. The brown and light blue circles denote the possible sites of two types of La dopants substituting the Sr atoms−La1 (on top and bottom SrO surfaces) and La2 (on middle SrO plane), respectively. The Black circles denote the possible Ir sites substituted by Ru dopants. The transparent cube represents the IrO_6 octahedra. (b) The top view of $Sr_3Ir_2O_7$ atomic structure. The pink square indicates the structural unit cell of topmost Sr square lattice, blue square denotes the super unit cell due to the AF order. (c-d) STM topographs acquired by spin-polarized (Cr bulk) tip at the +/-8T field over the same area. (e-f) The magnetic average (N(r)) and magnetic contrast (M(r)) maps, calculated by sum and subtraction between (c) and (d), respectively. (g-h) The corresponding Fourier transformed (FT) images of (e-f). $Q_{x(y)}$ peaks denote the Bragg peaks of topmost Sr square lattice and $Q_{a(b)}$ peaks indicate the order due to collinear AF.

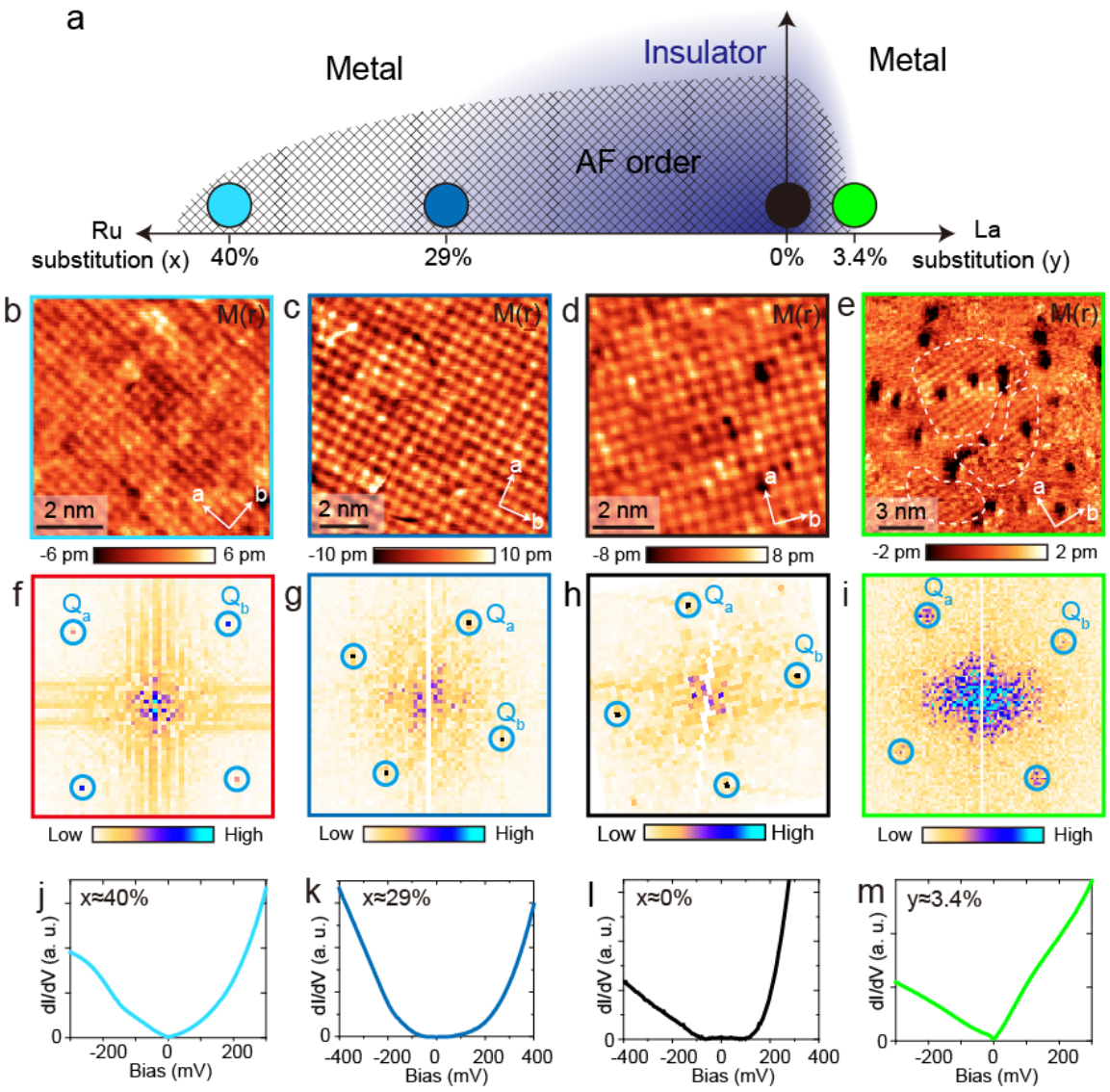

Figure 6. 2. 2 Phase diagram of $(Sr_{1-x}La_x)_3$ $(Ir_{1-y}Ru_y)_2O_7$. (a) Temperature-doping phase diagram of $(Sr_{1-x}La_x)_3(Ir_{1-y}Ru_y)_2O_7$. The four colored solid circles represent the differently doped samples studied: 40% Ru-Sr327 (light blue), 29% Ru-Sr327 (dark blue), parent Sr-327 (black) and 3.4% La-Sr327 (green). (b-e) The atomic-scale M(r) map and (f-i) the associated FT images. (j-m) the spatially averaged *dI/dV* (r, V) spectra acquired by the spin-polarized tip. The dashed white line denotes the domain boundary of magnetic contrast modulations.

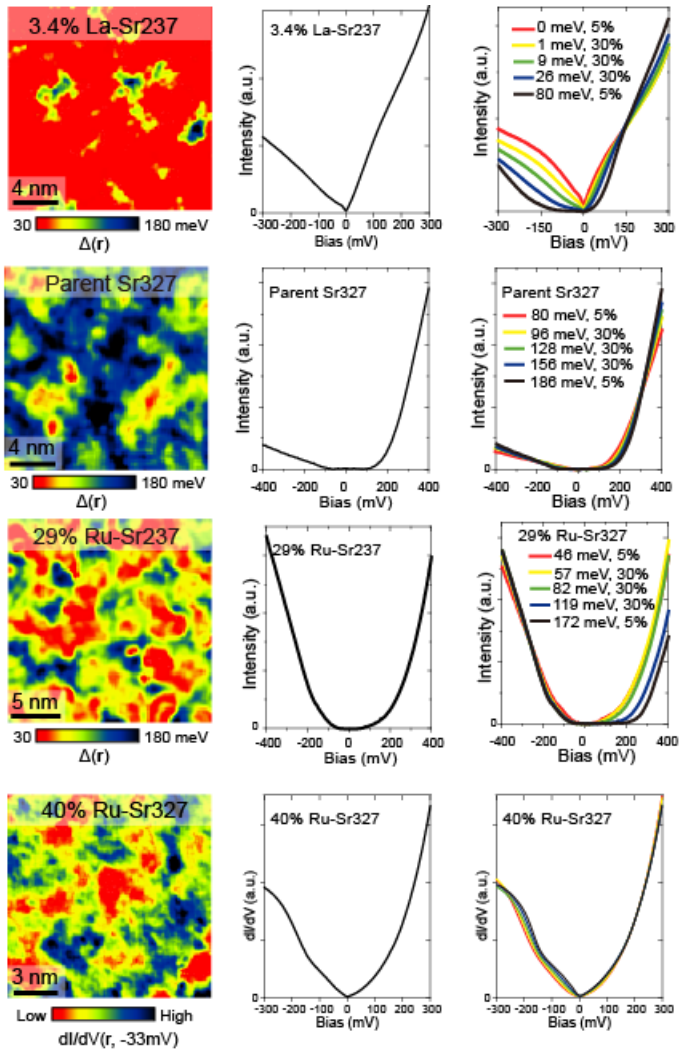

Figure 6. 2. 3 dI/dV(r, V) spectra evolution with doping. The top three rows in the left column display the gap maps of 3.4% La-Sr327, parent Sr327, and 29% Ru-Sr327, respectively, and the last row denotes the *dI/dV* map at -33mV over 40% Ru-Sr327. The middle column represents the spatially averaged *dI/dV* spectrum correspondingly. The top three rows in the right column present the unevenly binned averaged spectra by the gap map, the last row displays the binned averaged spectra by the dI/dV(r, -33mV) map.

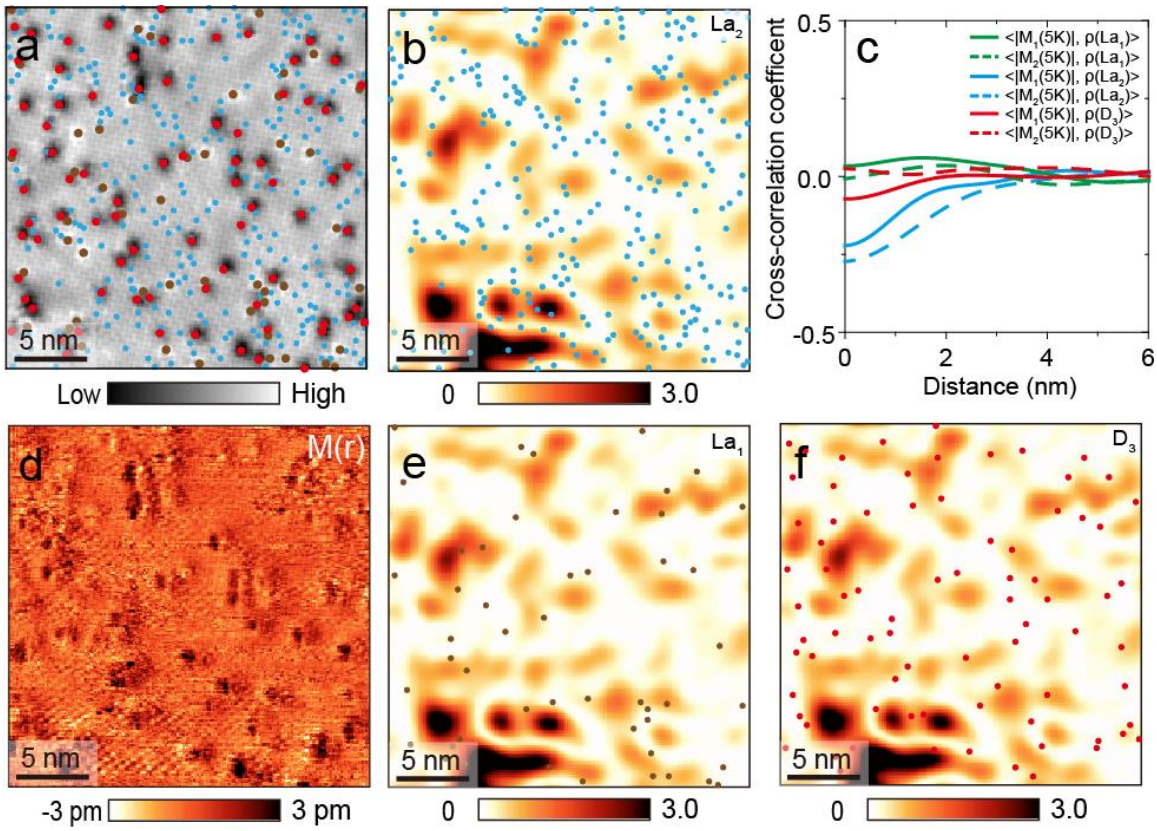

Figure 6. 2. 4 Correlation between magnetic order and La dopants distribution. (a) STM topograph on 3.4% La-Sr327, taken over the same 3.4% La-Sr327 sample in **Figure 6. 2. 2** but on the FOV with micrometer away. The light blue, red, and brown dots denote the positions of La2, La1, and 'dark' dopants, respectively. The magnetic magnitude map superimposed with (b)La2, (e)La1, and (f)'dark' dopants. (c) The correlation between magnetic magnitude map and different dopants map. (d) M(r) map calculated by topographs acquired at +/- 4T by the spin-polarized tip.

6.3 THE EFFECTS OF THERMAL CYCLING ON THE ANTIFERROMAGNETIC ORDER IN 3.4% LA-DOPED $(SR_{1-X}LA_X)_3IR_2O_7$

Having studied the roles played by doping, with either hole or electron, we proceed to explore the thermal fluctuating effect on magnetism near the IMT. We focus on a small area (~26 nm) on a 3.4% La-Sr327 sample and measure the magnetic contrast map (M(r)), as described in the previous section. We start from the M_1(5 K) map at 5 K, by applying 4T filed in different directions. Then warming up the sample at zero B, when the temperature stabilizes at 7K, we obtain the M_1(7K) map over the identical area with the same field and scanning conditions. After repeating the measurement of the M(r) map by heating further to 9K (M_1(9K)), we cool down the system back to 5K and acquire the M_2(5K) map. **Figure 6. 3. 1** (a-d) displays the magnitude maps (|M(r)|) during the thermal cycling as described above. Each of the |M(r)| maps presents 2D magnetic clusters with varying morphology, and obviously, the overall magnitude keeps decreasing in the warming loop (5K to 7k and to 9K) and recovers after the cooling loop (9K to 5K directly). Quantitatively, the spatially averaged magnitude of each map is summarized and plotted in **Figure 6. 3. 1**(h), showing a ~fivefold huge suppression at 7K (9K) compared with 5K. Such contrast can be interpreted as a result of 3.4% La doping driven the system close to a critical point, around where the magnetic order transition happens. Interestingly, the AF domain distribution remains largely similar between 5 K and 7 K. Quantitatively, such AF order patterns being robust to the thermal erasure is evidenced by the high α (correlation coefficient) values from calculating correlations between |M_1(5K)|

and all other maps (**Figure 6. 3. 1** (e-g)). The magnetic 'memory' behavior through thermal cycling may be tightly related to the distribution of the La2 dopant, which cannot be shifted in both warming and cooling thermal loop. However, the AF order texture and magnitudes of gap maps at 9 K don't manifest much difference from 5 K, indicating the low correlation between the AF order and spectral gap magnitude (**Figure 6. 3. 1**(i, l)). Similar to the persistent long-range AF order deep into metallic Ru-Sr327, the AF order in La-Sr327 cannot be simply explained by the charge gap opening.

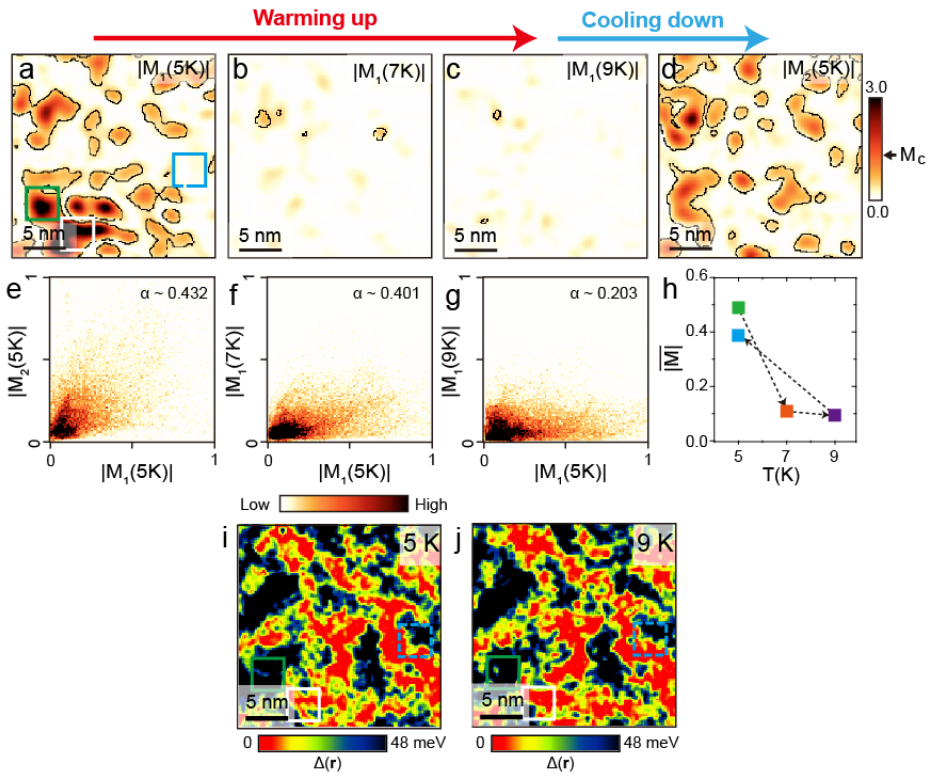

Figure 6. 3. 1 Antiferromagnetic texture change during thermal cycling. (a-d) Evolution of the magnetic order magnitude maps acquired over identical FOV in the 3.4% La-Sr327 during the thermal cycling. The AF order puddles with a universal cutoff M_c are outlined by the black line in each map. The correlation histogram between the AF order map at initial 5K (warming cycle) and other order magnitude maps at (e)7K, (f)9K, and (g)5K (cooling cycle), respectively. (h) The plot of the averaged magnitude of AF order vs T. All of the four |M(r)| maps are obtained with keeping processing parameters consistent: firstly the M(r) map is inversely Fourier transformed through four circled areas covering only the (1/2, 1/2) $Q_{a(b)}$ peaks with a radius of ~0.076/Å per circle, the obtained map is then smoothed with 2 pixels, and the neighboring pixel has ~1.22 Å spacing. The gap map over the same area at (i) 5 K (warming cycling) and (j) 9K. The colored squares over panel (a, i, and j) are selected over strong (solid) and weak (dashed) AF order patches, are the guidance for comparing the local AF order magnitude and gap size.

6.3.1 The scale-free magnetic textures in 3.4% La-doped $(Sr_{1-x}La_x)_3Ir_2O_7$

Driven by La doping, the long-range AF order parameter melts into granular magnetic fabrics. And such a resulting 2D pattern also allows us to do higher-level statistical analysis of the domain distribution. Here, we apply a 2D percolation model, a powerful tool describing the behavior of the network, to our short-range AF order magnitude maps, as shown in **Figure 6. 3. 2**. Firstly we binarize the $|M_1(5K)|$ map into dark clusters and white background based on the magnetic magnitude. The magnitudes interior of the dark islands are above the threshold (Mc defined in **Figure 6. 3. 1**) while within the white background are below Mc, denoting that the AF ordered area is separated from paramagnetic regions. The border of each dark cluster is outlined as shown in **Figure 6. 3. 1** (a). Note that the region in **Figure 6. 3. 1** (a) is cropped from **Figure 6. 3. 2** (a).

We can extract some geometrical descriptors of each cluster necessary for further statistical analysis: the perimeter (P) of the border, the area (A) encircled by the outline, and the gyration radius (Rg, a measure of the length scale of the cluster, as defined in ref. 151). **Figure 6. 3. 2** (d) shows the domain area distribution histogram. We employ logarithmic binning, a standard technique for power-law distribution analysis[110]. Obviously, most of the points fall onto a straight line, exhibiting a power low scaling spanning over 2.5 decades in the ordered area with a critical exponent of $\tau = 0.88 \pm 0.24$. Using logarithmic binning, we plot the A *vs.* Rg (**Figure 6. 3. 2** (e)) and P *vs.* Rg (**Figure 6. 3. 2** (f)), respectively. Near the critical point, the cluster volumes and surfaces become fractal. The plots indicate power-law scaling across ~1.5 decades, with

the returned critical exponents of dv^* (effective volume dimension) = 2.0 ± 0.09 (**Figure 6. 3. 2** (e)) and dh^* (effective hall dimension) = 1.20 ± 0.05 (**Figure 6. 3. 2** (f)). The exponent, dh^*/dv^*=3/5 ± 0.04, extracted from the plot of **Figure 6. 3. 2** (b) matches the calculated $dh^*$and dv^* individually, proving the validity of our percolation analysis. The fractal dimension characterization of the system reveals that the 3.4% L-Sr327 can be explained by a correlated percolation model with electron-electron interactions playing a significant role, otherwise, the critical fractal dimensions are expected to be $dh^* = 7/4 = 1.75$, $dv^* = 91/48 = 1.8958$, extracted from uncorrelated percolation model. We should note that the clusters touching the boundary of the binary map have been excluded before applying percolation analysis. These observations and non-integral exponents reflect the unexpected fractal nature of the magnetic pattern.

Another function, pair connectivity (*PC(r)*), describes the probability that two sites separated by a distance *r* belong to the same connected finite cluster. We fit the plot, *PC(r) vs. r* in **Figure 6. 3. 2** (c) with relation, $PC(r) \sim r^{-\eta} exp^{(-r/\xi)}$, where r is the distance between two sites, ξ is the correlation length, and find that the scaling exponent of pair connectivity function is also far from the uncorrelated model. The hollow circles, representing large size clusters in the *PC(r)* plot, are excluded when fitting because the number of clusters is limited by the size of the map, which also explains the scaling only spanning ~1.5 decades. The power-law scaling in the clusters distribution, the fractal dimensions, and the pair connectivity function are all indicators of near-critical behavior, which has been previously discussed in the case of rare earth nickelates[111, 112, 113], nematic order of cuprates[114]. We find that our analysis also satisfies the hyperscaling relation

$d - 2 + \eta = 2\ (d - dv)$ with our extractions, and it corroborates the validity of our analysis as well.

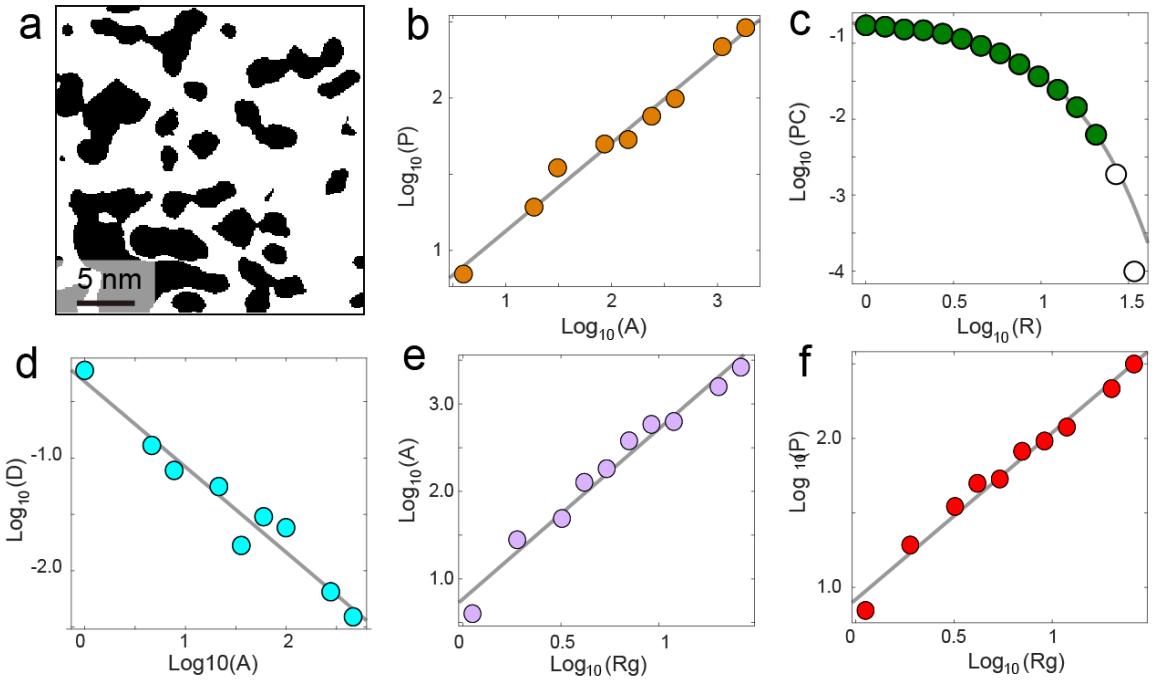

Figure 6. 3. 2 Scale-invariant magnetic texture at 5K (warming cycle). (a) The binarized AFM domain map at 5 K (warming cycle) highlighting the AF domains (black) vs other areas (white) with lower AF order magnitude than M_c. (b) Domain perimeter (*P*) vs. area (*A*), reflecting the effective fractal dimension ratio, dh^*/dv^*. Logarithmic binning has been used. The solid line is the power-law fit of $P \sim A^{dh^*/dv^*}$ with $dh^*/dv^* \sim 3/5$. (c) Pair connectivity (*PC*) function vs. distance (*r*) with logarithmic binning. The solid line is fit to a power-law function with an exponential cutoff $g_{conn} \sim r^{-\eta}\, e^{-x/\xi}$, where ξ is the correlation length and $\eta = 0.02 \pm 0.01$ is the exponent for the connectivity function. (d) The logarithmically binned AF domain area distributions, following a scale-free power-law distribution ($D \sim A^{-\tau}$) with the critical exponent $\tau = 0.88 \pm 0.24$. The solid line is a power-law fit to the experimental data points. (e, f) Domain perimeter (*P*) and area (*A*) vs. gyration radius (R_g) with logarithmic binning. Solid lines are power-law fits of $P \sim R_g^{dh^*}$, $A \sim R_g^{dv^*}$ and with the critical exponents $dh^* = 1.20 \pm 0.05$ and $dv^* = 2.0 \pm 0.09$. The unit of *P, R,* and *Rg* are in the unit of pixel and *A* is in the unit of the area occupied by a single pixel, the neighboring pixel spacing is 1.22 Å. Note that in principle the power law cannot be broken just by different choices of the unit.

7 NEMATICITY UNSTABILITY AND SUPPRESSION OF SUPERCONDUCTIVITY IN FE(TE, SE)

7.1 INTRODUCTION OF ELECTRONIC NEMATICITY IN IRON-BASED SUPERCONDUCTOR: $FeTe_{1-x}Se_x$

The superconductivity is always closely related to the nematicity state in iron-based superconductors, and the determination of the dominant interaction of nematicity state could be largely helpful for us to understand the superconductivity.

The nematicity state−a state that has 4-fold rotational symmetry broken into C_2 symmetry while keeping the translational symmetry invariant−has been observed in both cuprates[115, 116, 95], and iron-based superconductors[117, 118, 119, 120, 121, 122] whatever iron chalcogenides or pnictides. And the electronic nematic state (anisotropic electronic structure) in iron-based superconductors always accompanies a structural transition from tetragonal to orthorhombic lattice crossing T_S, whereas the T_{nem} doesn't necessarily have to be the same as T_S[123, 124], especially on iron-pnictides (**Figure 7. 1. 1**). In the nematic state, the tetrahedral bonding environment or the iron plane is distorted into orthorhombic shape with lattices along x and y inequivalent so that the degeneracy of iron's *3dxz* and *3dyz* orbitals lifts. Another parameter that can cause the C-4 symmetry breaking is the magnetic order even on a tetragonal lattice, which simultaneously breaks the Z2 symmetry: the collinear AFM order(or spin-nematic state) could have either Qx=(n,0) or

Qy=(0,n) (n= π/a_0, a_0 is the longer lattice constant after the distortion) wavevector following the interplay of hole pockets at Γ and electron pockets at the corner of 2Fe Brillouin zone. Therefore, if considering the lattice distortion, all of the parameters mentioned above could cause the C-4 rotational symmetry breaking−the typical nematic phase arising. And it's heavily debated that the nematicity is primarily driven by which of the three freedom of degrees−charge/orbital, spin or lattice−on iron-based superconductors. From a symmetry point of view, it's clear that any of the order develops, the other orders must be affected. One of the possibility has been ruled out: the lattice distortion is only the conjugate field of the primary driving parameter instead of the driving force itself, not only because the distortion is quite weak (~1%), but also a direct conclusion from anisotropy resistance measurement. Therefore, the nematicity (orthorhombic structure) could arise from either spin or orbital ordering and the two scenarios have been proposed following that. One scenario is that the orthorhombic structural change from tetragonal is due to the orbital ordering. The onset of the SDW state is a consequence of the structural C-4 lattice rotational symmetry breaking, which itself is driven by the ferro-orbital ordering[125,126]. And other anisotropic properties displayed in this distorted lattice is due to the unequal occupations between d_{xz} and d_{yz} orbitals between Fe atoms. Another scenario is the opposite of the above one: the SDW induces the structural transition[127, 128, 129, 130, 131]. As can be seen in the **Figure 7. 1. 1**, the $T_{nem}(T_S) > T_N$, so it's not AFM order but the fluctuation that induces the nematicity. When T is between $T_{nem}(T_S)$ and T_N, before the magnetic order forms, the O(3) symmetry(time-reversal symmetry) preserves but Z2 symmetry breaking, a spin-nematic state will set in, preempting the SDW state. Similarly to lattice rotational symmetry breaking, such spin-

driven nematic state gives rise to the nematic orbital order, as the electron pocket at corner of 2-Fe Brillouin zone along X has mostly d_{yz} character while along Y has mostly d_{xz} character.

FeSe is a representative for the iron chalcogenide family with the simplest atomic structure, and experience a structural transition from tetragonal to the orthorhombic lattice. However, it might be the only exception in iron-based superconductors that doesn't show an interaction between nematic order and magnetic order, and experimental evidence supports that its nematicity phase is primarily driven by orbital ordering[132, 133, 121, 134]. As we have mentioned above, the degeneracy of d_{yz} and d_{xz} orbitals being lifted induce the anisotropic electronic structure, i.e. electronic nematicity. However, the nematicity transition can be tuned by a series of parameters, such as chemical composition change[135, 136, 137], strain[138, 139, 140], and pressure[141, 142].

Recently, $FeTe_xSe_{1-x}$ (Fe(Te, Se)) has attracted lots of attention mainly because of the emergence of topological surface states[143, 144], which is a result of the Te doping induced iron d orbital and p orbital inversion at Γ point, and Majorana modes at x~0.55[145, 146, 147]. However, x~0.55 is also proximate to a nematic transition point in the phase diagram, and the doping also prominently enhances the T_c from 8K on FeSe to 14.5K at ambient conditions (**Figure 7. 1. 2**). And one of the somewhat overlooked aspects of the intricate physics of Fe(Te, Se) near optimal doping is that it's expected to undergo an electronic nematic transition. Though the elastoresistance measurements have shown that the nematic fluctuation can be detected at this regime after applying uniaxial strain, the underlying physics of Fe(Te, Se) still has not been fully explored.

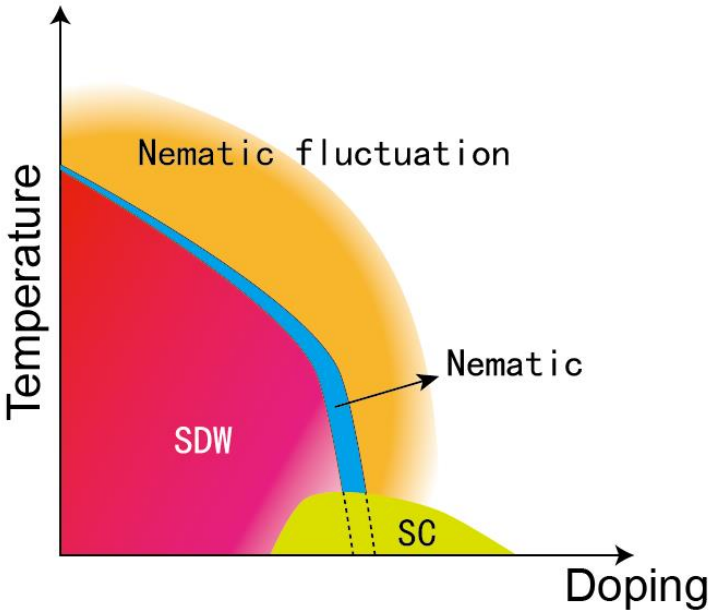

Figure 7. 1. 1 schematic phase diagram of iron pnictides. The SDW denotes the spin density wave, SC the superconducting state, Tel the tetragonal, PM the paramagnetic. The structural happens at T_{nem} while the nematic fluctuation happens at a higher temperature.

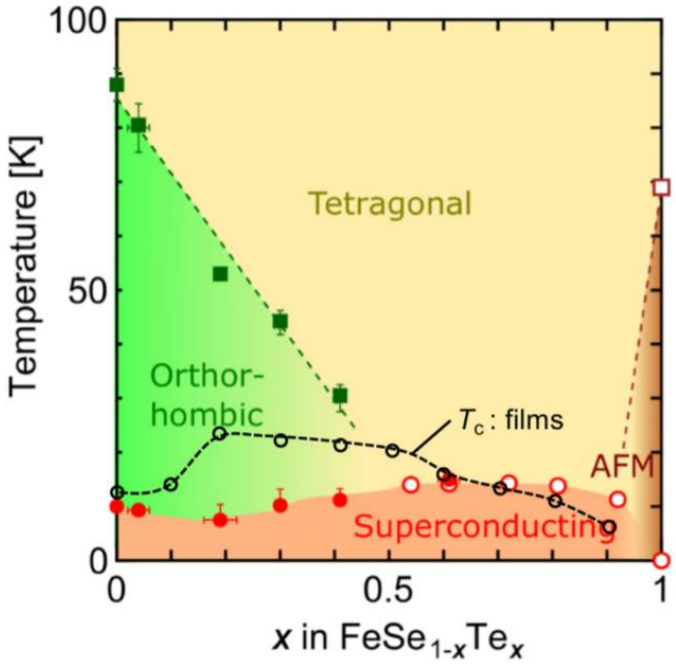

Figure 7. 1. 2 Schematic phase diagram of $FeSe_{1-x}Te_x$. The red solid circles denote the T_C, and the green squares indicate the T_S. The vertical bars of T_C represent the onset of the

transition temperature and the horizontal bars indicate the standard error of x. The figure is reprinted from ref. 148.

7.2 LOCAL NEMATICITY OBSERVED ON TOP OF FE(TE, SE) WITH STM/S

$FeTe_{1-x}Se_x$ has a square lattice, and the top layer is the Te(Se) plane as cleaved. On the STM topograph, only the topmost chalcogens Te(Se) atoms, showing as dark(bright) squared lattice with a_0~0.38 nm, can be detected and the sublayer Fe square lattice (**Figure 7. 2. 1** (a)), with an $a_0/\sqrt{2}$ lattice constant, has a 45 deg rotated from the topmost Te(Se) lattice. The bright sites (Se) versus dark one (Te) can help us determine the doping level x, as shown in **Figure 7. 2. 2**. To study the evolution of nematicity with doping crossing the nematic critical point, we focus on three similarly Te: Se samples proximate to that point with nominal x~ 0.4, 0.45, and 0.5 (**Figure 7. 2. 1** (b)). The characteristic *dI/dV* spectra of the three samples (inset of **Figure 7. 2. 1** (d-f)) all show a similar-sized SC gap ~2.5meV, indicating a combination of the gaps of hole pockets at Γ[149]. As shown in **Figure 7. 2. 1** (d-f), the x~0.5 is the most electronic modulated sample, and on top of the optimally doped (x~0.45), the most superconducting sample, one can observe an anisotropic electronic modulation domain, whereas electronic modulation is completely gone on x~0.4 sample. Here, we map the electronic modulation through L(r, V) = *dI/dV*(r, V)/ (I(r, V)/V) maps, removing the effect from the setup conditions. The directional modulations perfectly orient along the Fe-Fe direction for the x~0.45 and 0.5 samples, which means the underlying physics of such electronic property is intrinsically related to the iron-based superconductors. The absence of electronic modulation on top of

x~0.4 side indicates that it's within the tetragonal nonnematic phase, while the presence of modulation boundary on x~0.45 sample points to the existence of local orthorhombic phase, where one can detect the directional electronic modulation. The smooth transition between two domains shows no obvious structural imperfections of surface buckling, and the Te: Se ratio doesn't display any distinguishable difference either. And another parameter−the topmost interstitial Fe impurities−also doesn't play a significant role in forming the modulation domain (**Figure 7. 2. 3**) based on the result that the density of impurities doesn't vary crossing the nematic domain wall.

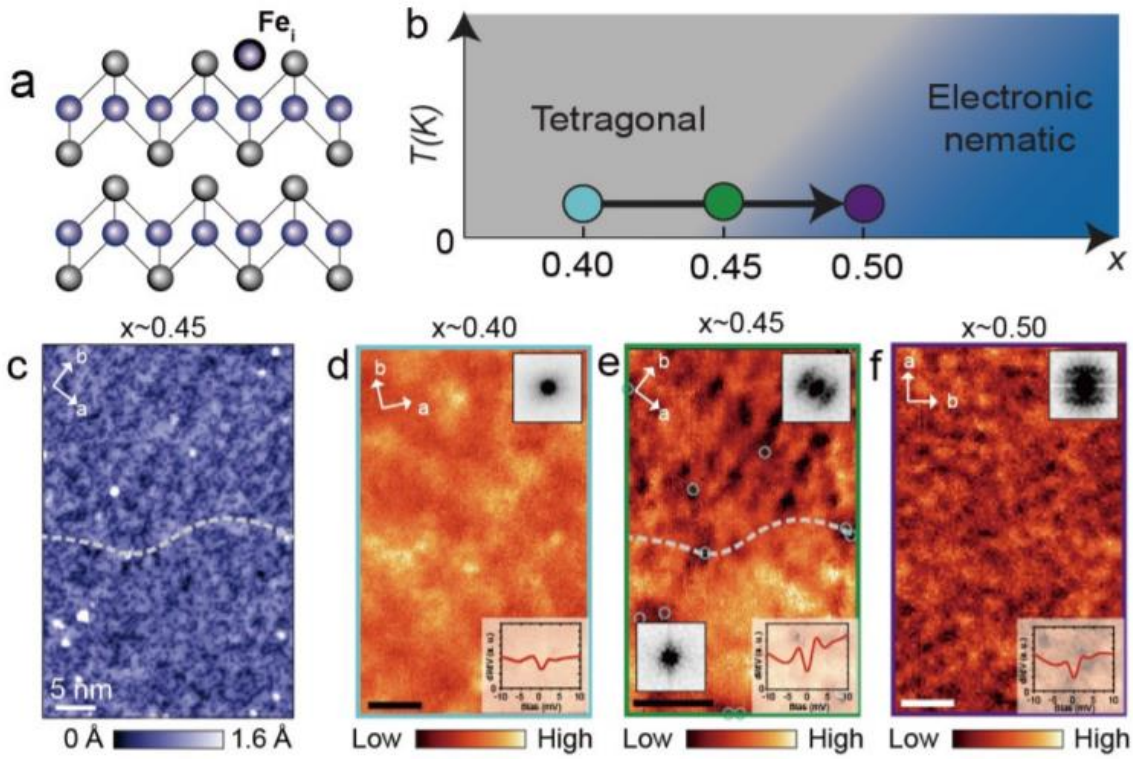

Figure 7. 2. 1 Nematic domain boundary of Fe(Te, Se). (a) The schematic of Fe(Te, Se) atomic structure. The big purple ball is the interstitial Fe impurity on the top Se(Te) layer. (b) The phase diagram of Fe(Te, Se) around optimal doping. The three colored dots denote the three differently doped samples we focus on. (c) STM topograph of $FeTe_{1-x}Se_x$ at x~0.45, encompassing a domain boundary, and the bright dots denote the interstitial Fe impurities, (e) is the simultaneously obtained L(r, V) map, the top half of which presents the anisotropic electronic modulation while the bottom half doesn't. (d-f) the L(r, V) maps of samples at x~0.4 and 0.5, respectively, and only x~0.5 can detect modulations. The inset spectra plots of (d-f) indicate the spatially averaged *dI/dV* spectrum over the associated regions; the upper right inset of (d-f) and lower left inset of (e) are the corresponding local FFT of the L(r, V) maps.

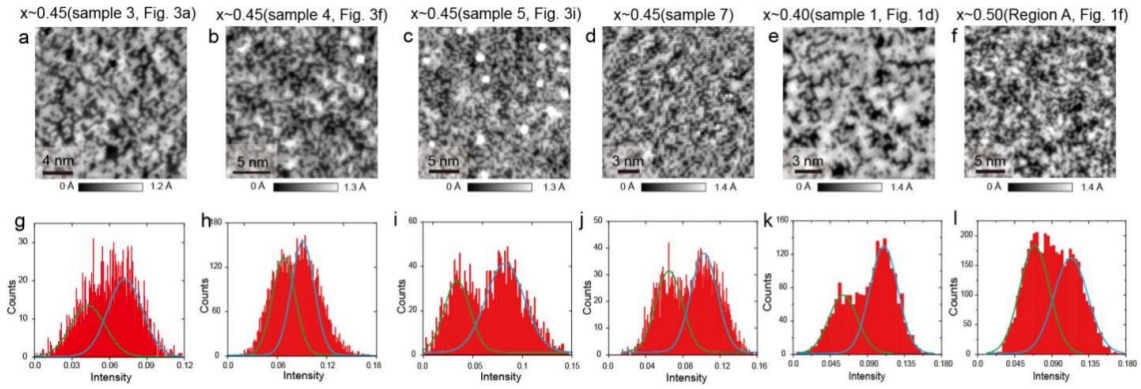

Figure 7. 2. 2 Composition analysis based on the brightness of the topograph of $FeTe_{1-x}Se_x$. (a-c) the topographs taken on top of different nominally doped samples. Bright dots are the interstitial Fe impurities. (g-l) the histogram of the brightness of the atom center pixel. Each histogram is fitted with two Gaussian curves. The ratio of areas under the two fitting curves is taken as a measure of Te/Se composition. The procedure of processing the topographs: 3rd polynomial background subtraction to remove the piezo relaxation and thermal effect, inverse FT covering through only the short-range spatial modulation, filtering out the long-range signals larger than ~7nm to enhance the brightness contrast between Te and Se sites.

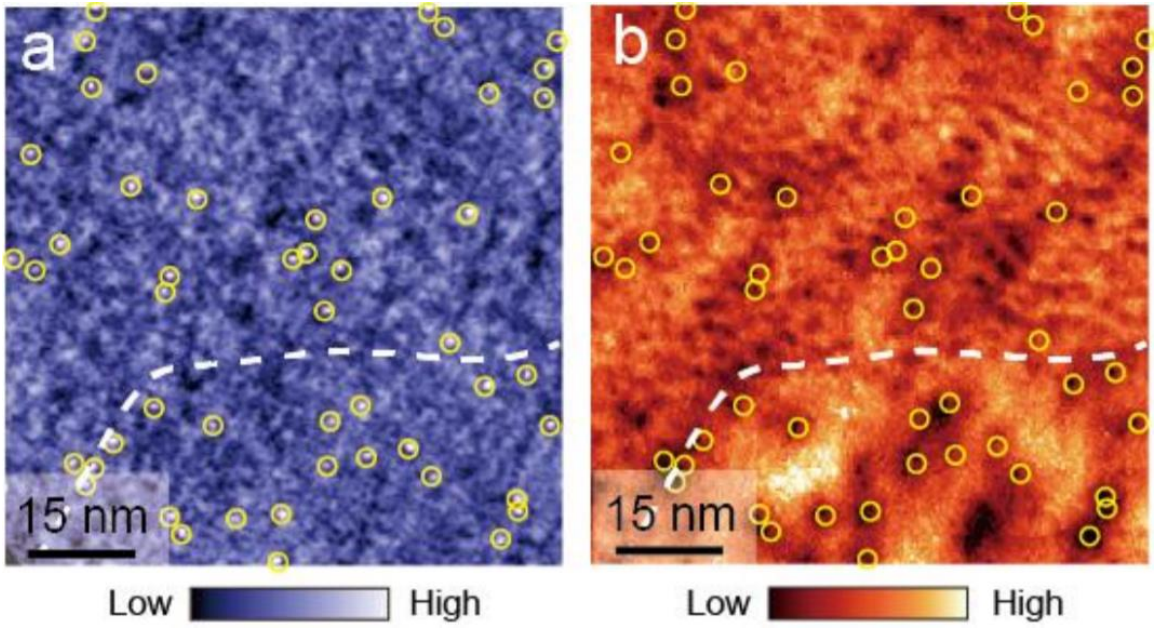

Figure 7. 2. 3 Excess Fe impurities distribution on x~0.45 sample #1. (a) STM topograph and (b) simultaneously obtained *dI/dV*(r, V) map. The yellow circles mark the position of interstitial Fe impurities. The modulation domain boundary is marked by the white dash curve.

7.2.1 Orbital order: dispersive anisotropic QPI on Fe(Te, Se)

To characterize the electronic modulations observed, we acquired L(r, V) maps as a function of energy (**Figure 7. 2. 4**). The unidirectional modulation wavelengths vary a lot even within tiny energy range across the Fermi level. Based on the Fourier transformed images of L(r, V) maps one can only see arc-shape electronic interference pattern along one of the reciprocal sublayer Fe lattice directions (Q_a), 45 degrees rotated from the surface Te/Se lattice Brag peaks, while nothing along the orthogonal direction (Q_b).

For guidance in determining the origin of the dominant wave vector, we refer to the band structure schematic of $FeTe_{1-x}Se_x$ (**Figure 7. 2. 4** (a, b)). The Fermi surface is composed of hole pockets at Γ and electron pockets around M point. Comparing the dispersion velocity and Fermi wave vector with ARPES results [146, 150], the trend that electronic interference wavevector length (Q_a) decreases with energy crossing Fermi level from below to above (**Figure 7. 2. 4** (f-h)) matches the scenario that the unidirectional QPI is probably related to the electronic interference or scattering intra-hole pocket around Γ instead of intra electron pocket at M point. Additionally, the STM tip typically cannot pick up large wave vector signals of reciprocal space in these systems, which supports the intra-hole pocket interference near Γ as well. The result that the anisotropic scattering signature is consistent with scattering between d_{yz} orbital (Q_a) while no scattering between d_{xz} orbital (Q_b) could be explained in terms of the variation of the spectral weight of different orbitals, giving rise to the orbital-selective quasiparticles in the electronic nematic state [151]. This nonequal spectral weight is also accompanied by an elongated Fermi surface, causing the near-parallel Fermi sheets which enhance the

quasiparticle scattering along Q_a. Ref. 151 concludes with a picture that much higher spectral weight on d_{yz} orbital than d_{xz} and d_{xy} induced orbital-selective strong correlations in parent FeSe. This picture is also consistent with our measurements of the modulated electronic region of Fe(Te, Se) at x~0.45.

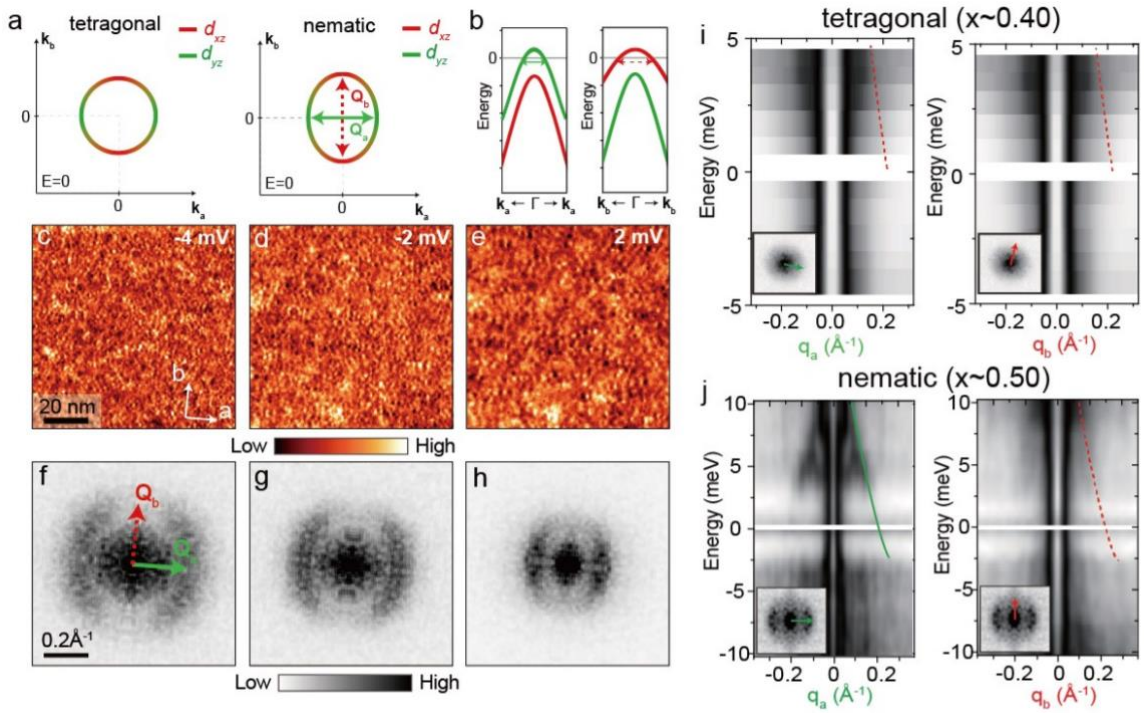

Figure 7. 2. 4 Anisotropic electronic scattering. Schematic of hole pocket at Γ point of Fermi surface for tetragonal lattice phase (a, left) and orthorhombic, nematic phase (a, left). The different orbital content is denoted by red (d_{xz}) and green (d_{yz}). On the nematic Fermi surface, the QPI scattering appears along the larger parallel sheets (more d_{yz} orbital, Q_a) but it's absent along orthogonal direction (more d_{xz} orbital, Q_b), i.e. the smaller parallel sheets. (b) The dispersion of two electronic bands along k_x (left) and k_y (right). (c-e) Normalized conductance (L(r, V)) maps at different biases and (f-h) associated FT images on $FeTe_{1-x}Se_x$ with x~0.45. The two (Q_a and Q_b) arrows denote the expected scatterings as shown in (a, b). The linecuts in 2-fold symmetrized FT images of L(r, V) maps along different directions (q_a and q_b) on $FeTe_{1-x}Se_x$ samples at x~0.40 (i) and 0.50(j). The corresponding inset displays FT image of representative L(r, V) maps and the direction of linecut.

7.2.2 The competition between superconductivity and electronic nematicity tuned by uniaxial strain

We find that the nematic modulation only exists where the superconductivity gets suppressed (**Figure 7. 2. 5** (f-j)) and completely absent (**Figure 7. 2. 5** (a-e)). However, the C2-symmetric electronic modulations are gone in a strong superconducting region and the superconducting gap is clear (**Figure 7. 2. 5** (k-o)). While our measurements demonstrate that the superconductivity and nematicity could co-exist, they show a competition relation between the two order parameters locally. The QPI crossing different nematic regions are comparable, regardless of the presence of superconductivity or not, and the scattering wave vector crossing Fermi level is ~0.2 $Å^{-1}$, which is consistent with the ARPES result.

As we have mentioned that there is no evident change in Te/Se ratio and Fe impurities distribution from the atomic topograph crossing the nematic domain wall in **Figure 7. 2. 1**. This leaves the possibility of structural inhomogeneity. While we don't intentionally apply strain to the sample in our standard sample preparation process, few tenths of a percent of strain could be imparted on the sample due to small differences in thermal contraction coefficients[120]. To investigate this, we apply uniaxial strain analysis (**Figure 7. 2. 6**), which can detect local variations of lattice constant change with a fraction of a percent resolution[152, 95], and the calculated uniaxial strain map shows spatial variations of strain at the order of ~1%. By comparing the strain map with the amplitude map of QPI modulations acquired over the same region, we notice that there is a high correlation coefficient ~0.6 after calculating the correlation relation between these two parameter

maps. This strong correlation indicates that the C2-symmetry modulation is driven by the strain locally. Consistent with the observation in **Figure 7. 2. 5**, the superconductivity gets suppressed over the same strained region, as shown in **Figure 7. 2. 7** (h). This can also be visualized by comparing the averaged *dI/dV*(r, V) spectra in regions of different strain over the same FOV, where the 1% uniaxial strain could strongly suppress the coherence peak and enhance the spectral filling within the gap. However, the gap size (Δ(r)) is robust to the local strain and the Δ(r) map exhibits a low correlation with the strain map (**Figure 7. 2. 8**). Thus the suppression of superconductivity in Fe(Te, Se) is dominated by the loss of coherence, not the decrease in pairing strength.

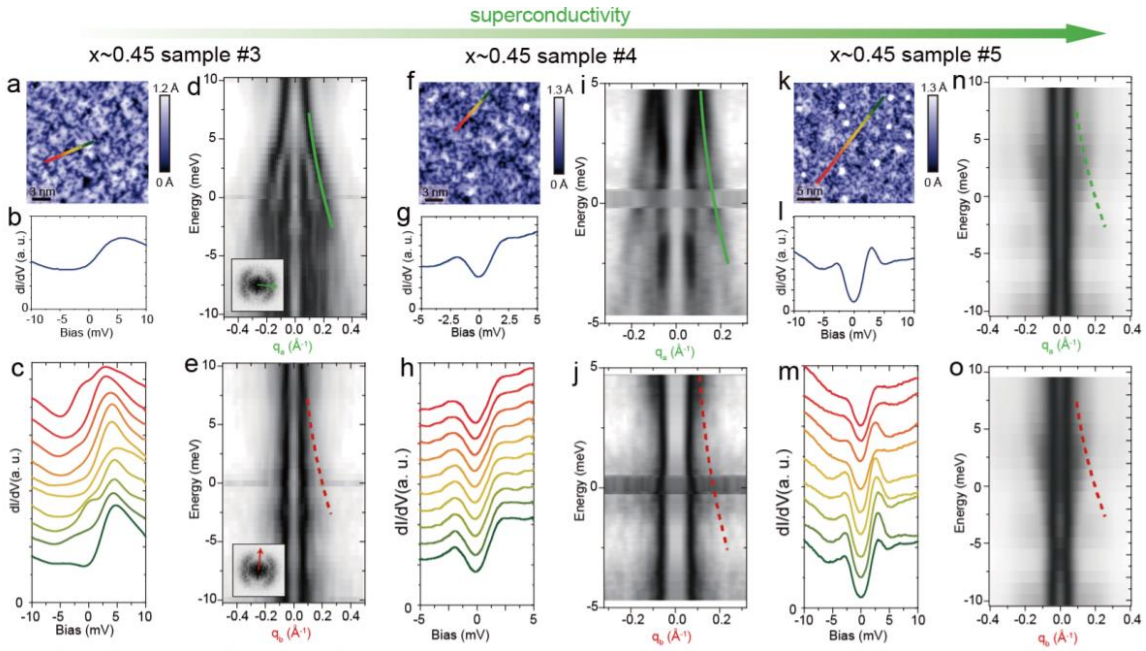

Figure 7. 2. 5 Spectroscopic-imaging scanning tunneling microscopy of critical composition. (a, f and k) STM topographs, (b, g, and l) spatially averaged *dI/dV* spectrum, (c, h, and m) *dI/dV* linecuts, (d, e, i, j, n, o) linecuts in FT images of L(r, V) maps along different directions taken on different $FeTe_{1-x}Se_x$ samples at the critical doping, i.e. x~0.45. The insets of (d, e, i, j, n, o) portray the linecut directions. Green solid curves are

the visual guides showing the dispersion of Q_a. Red dashed curves denote the absence of scatterings as expected at those positions.

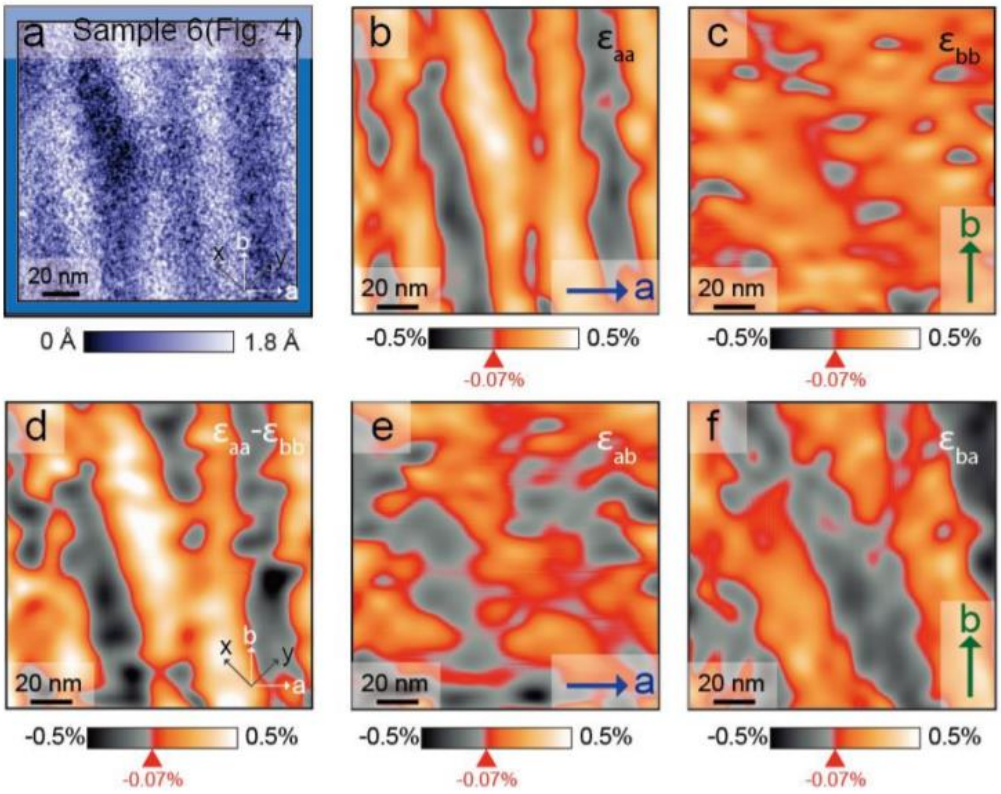

Figure 7. 2. 6 Strain analysis of Fe(Te, Se) in **Figure 7. 2. 7** at x~0.45. (a)Cropped STM topograph from **Figure 7. 2. 8** (a). (b, c) strain tensor components along a and b direction, $\boldsymbol{\varepsilon_{aa}(r)}$ and $\boldsymbol{\varepsilon_{bb}(r)}$, respectively. (d) Relative uniaxial strain map obtained by subtraction between (b) and (c). (e, f) Shear strain components $\boldsymbol{\varepsilon_{a}}_{\mathrm{b}}\boldsymbol{(r)}$ and $\boldsymbol{\varepsilon_{b}}_{\mathrm{a}}\boldsymbol{(r)}$.

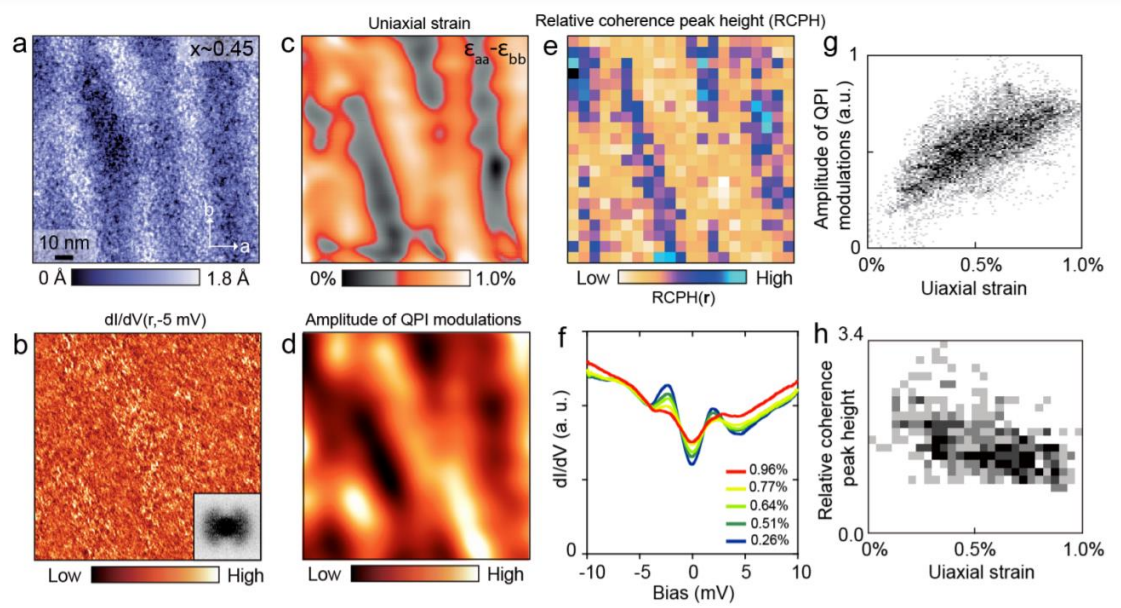

Figure 7. 2. 7 The interplay between strain and superconductivity. (a) atomic STM topograph and (b) simultaneously acquired *dI/dV* map at -5mV showing the QPI, (c) uniaxial strain map, (d) local amplitude map of QPI modulation from (b), and (e) relative coherence peak height (RCHP)= (*dI/dV*(r,Δ+) + *dI/dV*(r,Δ-))/(2·*dI/dV*(r,0)) map acquired over same region as (a-d). (f) Average spectra binned by the strength of uniaxial strain. (g) Correlation histogram between amplitude map of QPI modulation in (d) and uniaxial strain map in (c) showing a high correlation coefficient ~ 0.6. (h) Correlation histogram between RCHP map in (e) and uniaxial strain map in (c) showing a high anti-correlation coefficient ~- 0.5.

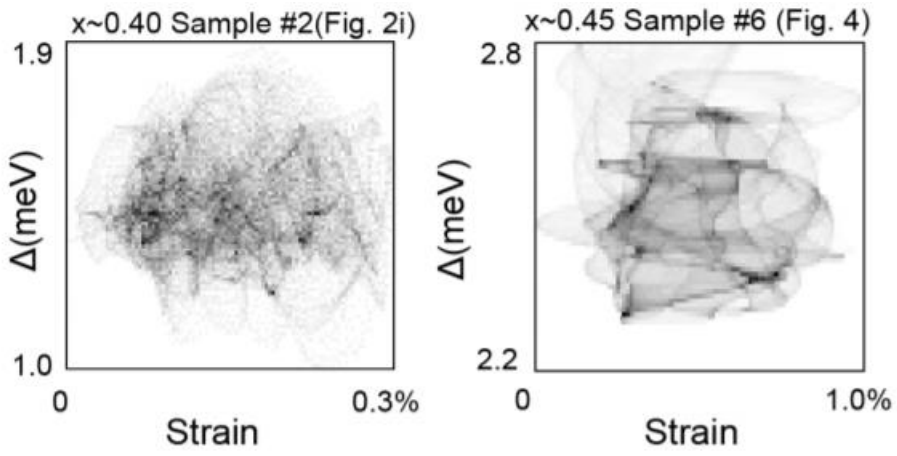

Figure 7. 2. 8 The correlation histogram between gap size (Δ(r)) map and uniaxial strain map over the sample at x~0.4 (left) and x~0.45 (right).

7.3 BEYOND THE STRAIN

As we have shown above that the superconductivity can be strongly suppressed by moderate external strain. However, we find that the completely suppressed superconductivity cannot be fully explained by only the strain on Fe(Te, Se) sample at x~0.45. We apply strain analysis to an atomic topograph encompassing nematic domain boundaries but not obviously buckling area (**Figure 7. 3. 1**), and the uniaxial strain magnitudes don't vary much crossing those boundaries, which sets the upper bar of uniaxial strain over the non-SC nematic regions to ~0.1%. However, the upper bound value sees contradiction on other samples at x~0.45, for example, the strain analysis on the sample from **Figure 7. 2. 7** shows that the nematicity appears at ~1% strain while low superconducting coherence peak and weak symmetric gap feature survive. Thus the strain cannot be the dominant driving mechanism for the suppressed SC and nematicity arising for Fe(Te, Se) at critical doping. For samples away from the critical point, in x~0.40, the

buckling induced 0.5% doesn't give rise to the anisotropic electronic scattering, i.e.electronic nematicity.

The ref. 138 reports that the quantum critical fluctuation associated with the divergent nematic susceptibility in the same material and our observation is consistent with the existence of an underlying nematic quantum critical point picture at critical doping. The detected local nematicity can be a reflection of quantum nematic fluctuation at critical composition.

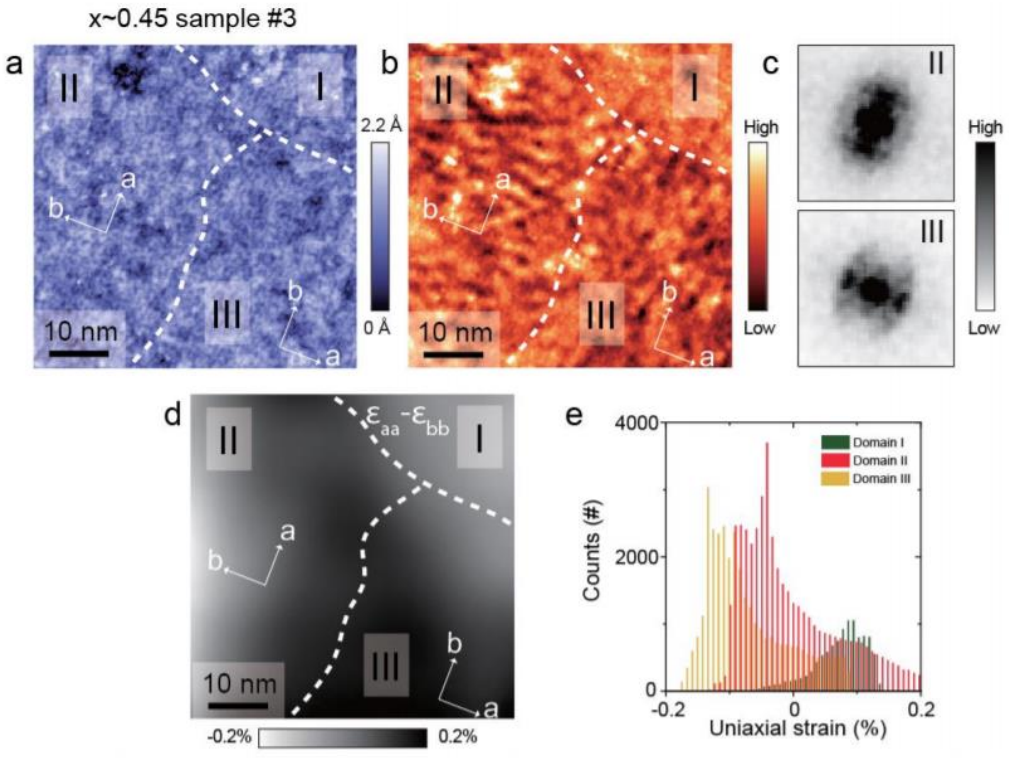

Figure 7. 3. 1 Nematic domain in one FOV of Fe(Te, Se) sample at x~0.45. (a) STM topograph and (b) simultaneously acquired *dI/dV(*r, V=-4 mV). (c) Fourier transforms (FTs) of areas in (b) within the domain (II) and (III). (d) The uniaxial strain map over the region in (a, b). The boundaries between domains I, II, and III are denoted by the white dash curves. (e) Histogram of relative uniaxial strain value within each domain.

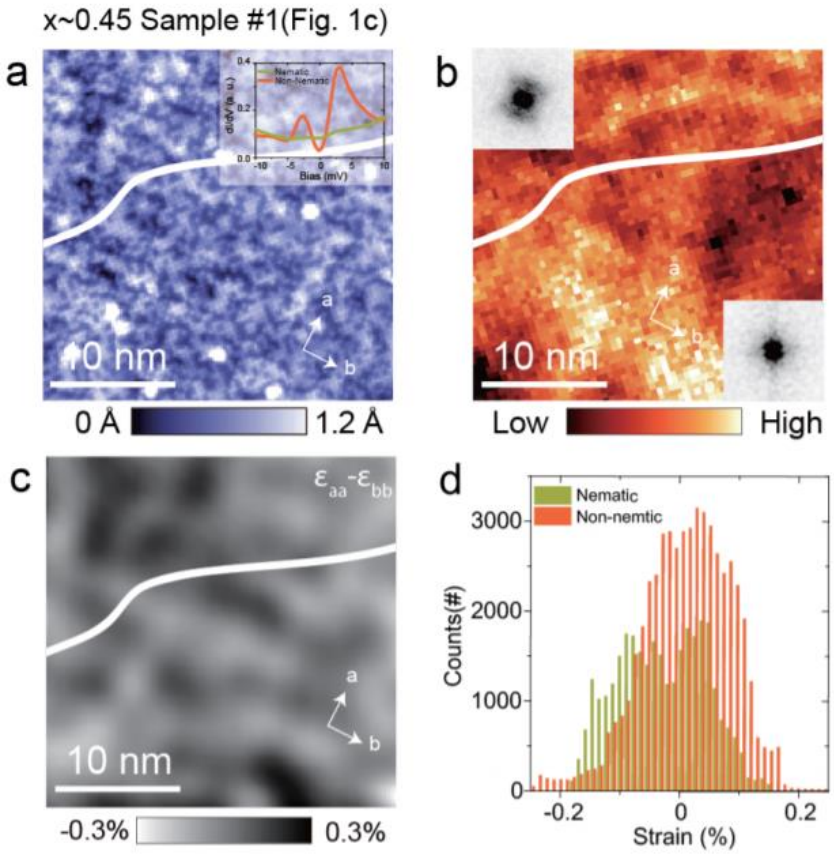

Figure 7. 3. 2 Another nematic domain FOV on critical Fe(Te, Se). (a) STM topograph and (b) simultaneously acquired *L(*r, V=2 mV). Inset in (a) shows the spectrum at a randomly picked point within two domains. Inset in (b) shows the Fourier image of each domain. The white solid line marks the boundary between the nematic domain. (c) The uniaxial strain map over the region in (a, b). (d) Histogram of strain magnitude within nematic (green) and nonnematic (orange) domain.

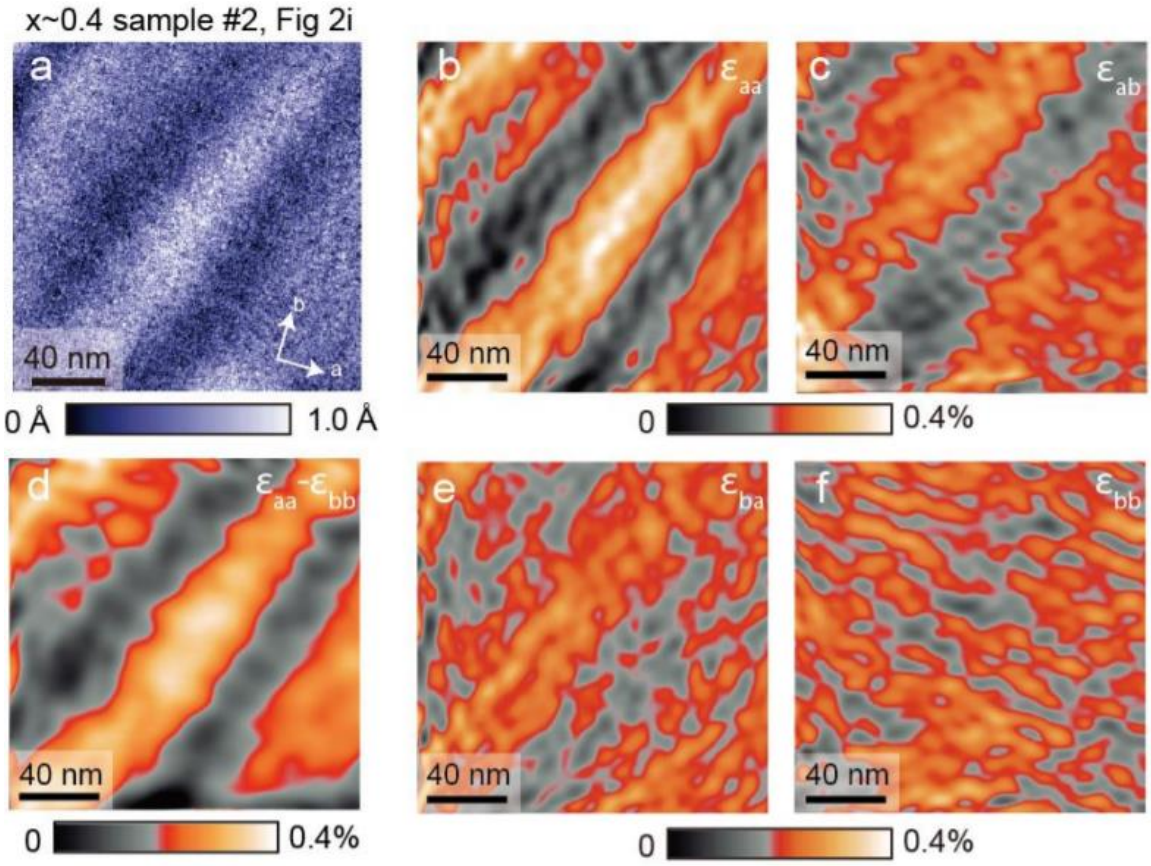

Figure 7. 3. 3 Strain analysis on Fe(Te, Se) at x~0.40. (a) STM topograph and (b) simultaneously acquired *L(*r, V=2 mV). (b-f) Strain tensor components, calculated in the same method as **Figure 7. 2. 6**. (d) Uniaxial strain map obtained by subtracting (b) and (c).

8 BIBLIOGRAPHY

1. De Gennes, P. G. Boundary effects in superconductors. *Rev. Mod. Phys.* **36**, 225–237 (1964).

2. Fu, L. & Kane, C. Superconducting Proximity Effect and Majorana Fermions at the Surface of a Topological Insulator. *Phys. Rev. Lett.* **100**, 096407 (2008).

3. Ogata, M. & Fukuyama, H. The t–J model for the oxide high-Tc superconductors. *Reports Prog. Phys.* **71**, 036501 (2008).

4. Moskvin, A. S. True charge-transfer gap in parent insulating cuprates. *Phys. Rev. B* **84**, 75116 (2011).

5. Hashimoto, M., Vishik, I. M., He, R. H., Devereaux, T. P. & Shen, Z. X. Energy gaps in high-transitionerature cuprate superconductors. *Nat. Phys.* **10**, 483–495 (2014).

6. McElroy, K. *et al.* Relating atomic-scale electronic phenomena to wave-like quasiparticle states in superconducting $Bi_2Sr_2CaCu_2O_{8+\delta}$. *Nature* **422**, 592–596 (2003).

7. Lee, W. S. *et al.* Abrupt onset of a second energy gap at the superconducting transition of underdoped Bi2212. *Nature* **450**, 81–84 (2007).

8. Tranquada, J. M., Sternllebt, B. J., Axe, J. D., Nakamurat, Y. & Uchldat, B. S. Evidence for stripe correlations of spins and holes in copper oxide superconductors. *Nature* **375**, 561–563(1995)

9. Hoffman, J. E. *et al.* A four-unit cell periodic pattern of quasi-particle states surrounding vortex cores in $Bi_2Sr_2CaCu_2O_{8+\delta}$. *Science.* **295**, 466–469 (2002).

10. Tranquada, J. M. *et al.* Coexistence of, and competition between, superconductivity and charge-stripe order in $La_{1.6-x}Nd_{0.4}Sr_xCuO_4$. *Phys. Rev. Lett.* **78**, 338–341 (1997).

11. Hoffman, J. E. *et al.* Imaging quasiparticle interference in $Bi_2Sr_2CaCu_2O_{8+\delta}$. *Science* **297**, 1148–1151 (2002).

12. Hanaguri, T. *et al.* A 'checkerboard' electronic crystal state in lightly hole-doped $Ca_{2-x}Na_xCuO_2Cl_2$. *Nature* **430**, 1001–1005 (2004).

13. Vershinin, M. *et al.* Local Ordering in the Pseudogap State of the High-Tc Superconductor $Bi_2Sr_2CaCu_2O_{8+\delta}$. *Science.* **303**, 1995–1998 (2004).

14. Wise, W. D. *et al.* Charge density wave origin of cuprate checkerboard visualized by scanning tunneling microscopy. *Nat. Phys.* **4**, 696–699 (2008).

15. Shen, K. M. *et al.* Nodal quasiparticles and antinodal charge ordering in $Ca_{2-x}NaxCuO_2Cl_2$. *Science.* **307**, 901–904 (2005).

16. Da Silva Neto, E. H. *et al.* Ubiquitous interplay between charge ordering and high-temperature superconductivity in cuprates. *Science.* **343**, 393–396 (2014).

17. Doiron-Leyraud, N. *et al.* Quantum oscillations and the Fermi surface in an underdoped high-T_c superconductor. *Nature* **447**, 565–568 (2007).

18. Hanaguri, T. *et al.* A 'checkerboard' electronic crystal state in lightly hole-doped $Ca_{2-x}Na_xCuO_2Cl_2$. *Nature* **430**, 1001–1005 (2004).

19. Tanabe, K., and Hosono, H. Frontiers of Research on Iron-Based Superconductors toward their Application Related content. *Jpn. J. Appl. Phys.* **51**.1R (2012).

20. Chen, X., Dai, P., Feng, D., Xiang, T. and Zhang, F. C. Iron-based high transition temperature superconductors. *National Science Review* **1**, 371–395 (2014).

21. Qing-Yan, W. *et al.* Interface-Induced High-Temperature Superconductivity in Single unit-cell FeSe Films on $SrTiO_3$. *Chinese Phys. Lett.* **29**, 037402 (2012).

22. Ge, J. F. *et al.* Superconductivity above 100 K in single-layer FeSe films on doped $SrTiO_3$. *Nat. Mater.* **14**, 285–289 (2015).

23. Hiramatsu, -Hidenori *et al.* Fe-based superconducting thin films-preparation and tuning of superconducting properties. *Supercond. Sci. Technol.* **32**, 93001 (2019).

24. Lee, P. A., Nagaosa, N. & Wen, X.-G. Doping a Mott Insulator: Physics of High-Temperature Superconductivity. *Rev. Mod. Phys.* **78**, 17 (2006).

25. Zhang, F. C. & Rice, T. M. Effective Hamiltonian for the superconducting Cu oxides. *Phys. Rev. B.* **37**, 3759 (1987).

26. Wang, F. & Lee, D. H. The electron-pairing mechanism of iron-based superconductors. *Science* **332**, 200–204 (2011).

27. Hanaguri, T., Niitaka, S., Kuroki, K. & Takagi, H. Unconventional *s*-wave superconductivity in Fe(Se, Te). *Science.* **328**, 474–476 (2010).

28. Mazin, I. I., Singh, D. J., Johannes, M. D. & Du, M. H. Unconventional superconductivity with a sign reversal in the order parameter of $LaFeAsO_{1-x}F_x$. *Phys. Rev. Lett.* **101**, 057003 (2008).

29. Christianson, A. D. *et al.* Unconventional superconductivity in $Ba_{0.6}K_{0.4}Fe_2As_2$ from inelastic neutron scattering. *Nature* **456**, 930–932 (2008).

30. Du, Z. *et al.* Sign reversal of the order parameter in $(Li_{1-x}Fe_x)OHFe_{1-y}Zn_ySe$. *Nat. Phys.* **14**, 134–139 (2018).

31. Basov, D. N. & Chubukov, A. V. Manifesto for a higher T_c. *Nat. Phys.* **7**, 272–276 (2011).

32. Chubukov, A. Pairing Mechanism in Fe-Based Superconductors. *Annu. Rev. Condens. Matter. Phys.* **3***,* 57-9*2* (2012).

33. Chen, X. *et al.* Influence of electron doping on the ground state of $(Sr_{1-x}La_x)_2IrO_4$. *Phys. Rev. B* **92**, 75125 (2015).

34. Ilakovac, V. *et al.* Oxygen states in La- and Rh-doped Sr_2IrO_4 probed by angle-resolved photoemission and O *K*-edge resonant inelastic x-ray scattering. *Phys. Rev. B* **99**, 35149 (2019).

35. Cao, G. & Schlottmann, P. The challenge of spin–orbit-tuned ground states in iridates: a key issue review. *Rep. Prog. Phys.* **81**, 042502 (2018).

36. Ye, F. *et al.* Magnetic and crystal structures of Sr_2IrO_4 : A neutron diffraction study. *Phys. Rev. B* **87**, 140406 (2013).

37. Bertinshaw, J., Kim, Y. K., Khaliullin, G. & Kim, B. J. Square Lattice Iridates. *Annu. Rev. Condens. Matter. Phys.* **10**, 315–336 (2019).

38. Rau, J. G., Lee, E. K.-H. & Kee, H.-Y. Spin-Orbit Physics Giving Rise to Novel Phases in Correlated Systems: Iridates and Related Materials. *Annu. Rev. Condens. Matter. Phys.* **7**, 195–221 (2016).

39. Xu, S.-Y. *et al.* Momentum-space imaging of Cooper pairing in a half-Dirac-gas topological superconductor. *Nat. Phys.* **10**, 943–950 (2014).

40. Wiesendanger, R. Spin mapping at the nanoscale and atomic scale. *Rev. Mod. Phys.* **81**, 1495–1550 (2009).

41. Slonczewski, J. C. Conductance and exchange coupling of two ferromagnets separated by a tunneling barrier. *Phys.Rev. B* **39**, 6995 (1989).

42. Tersoff, J. & Hamann, D. R. Theory and Application for the Scanning Tunneling Microscope. *Phys. Rev. Lett.* **50**, 1998 (1983).

43. Hasan, M. Z. & Kane, C. L. Colloquium: Topological insulators. *Rev. Mod. Phys.* **82**, 3045–3067 (2010).

44. Fu, L. & Kane, C. L. Superconducting Proximity Effect and Majorana Fermions at the Surface of a Topological Insulator. *Phys. Rev. Lett.* **100**, 096407 (2008).

45. Sun, H.-H. *et al.* Majorana Zero Mode Detected with Spin Selective Andreev Reflection in the Vortex of a Topological Superconductor. *Phys. Rev. Lett.* **116**, 257003 (2016).

46. Xu, J.-P. *et al.* Artificial Topological Superconductor by the Proximity Effect. *Phys. Rev. Lett.* **112**, 217001 (2014).

47. Sun, H.-H. & Jia, J.-F. Detection of Majorana zero mode in the vortex. *npj Quantum Mater.* **2**, 34 (2017).

48. Qu, F. *et al.* Strong superconducting proximity effect in Pb-Bi_2Te_3 hybrid structures. *Sci. Rep.* **2**, 1–5 (2012).

49. Yang, F. *et al.* Proximity effect at superconducting Sn-Bi_2Se_3 interface. *Phys. Rev. B.* **85**, 104508 (2012).

50. Yilmaz, T. *et al.* Absence of a Proximity Effect for a Thin-Films of a Bi_2Se_3 Topological Insulator Grown on Top of a $Bi_2Sr_2CaCu_2O_{8+\delta}$ Cuprate Superconductor. *Phys. Rev. Lett.* **113**, 067003 (2014).

51. Wang, E. *et al.* Fully gapped topological surface states in Bi_2Se_3 films induced by a *d*-wave high-temperature superconductor. *Nat. Phys.* **9**, 621–625 (2013).

52. Zareapour, P. *et al.* Proximity-induced high-temperature superconductivity in the topological insulators Bi_2Se_3 and Bi_2Te_3. *Nat. Commun.* **3**, 1–8 (2012).

53. Zhao, H. *et al.* Superconducting Proximity Effect in a Topological Insulator using Fe (Te, Se). *Phys. Rev. B* **97**. 224504 (2018).

54. Li, Y.-Y. *et al.* Intrinsic Topological Insulator Bi_2Te_3 Thin Films on Si and Their Thickness Limit. *Adv. Mater.* **22**, 4002–4007 (2010).

55. Maciejko, J., Hughes, T. L. & Zhang, S.-C. The Quantum Spin Hall Effect. *Annu. Rev. Condens. Matter. Phys.* **2**, 31–53 (2011).

56. Okada, Y. *et al.* Direct observation of broken time-reversal symmetry on the surface of a magnetically doped topological insulator. *Phys. Rev. Lett.* **106**, 206805 (2011).

57. Sessi, P. *et al.* Signatures of Dirac fermion-mediated magnetic order. *Nat. Commun.* **5**, 1–8 (2014).

58. Zhang, T. *et al.* Experimental demonstration of topological surface states protected by Time-Reversal symmetry. *Phys. Rev. Lett.* **103**, 266803 (2009).

59. Wang, M. X., *et al.* The coexistence of superconductivity and topological order in the Bi_2Se_3 thin films. *Science.* **335**, 52–55 (2012).

60. Dynes, R. C., Garno, J. P., Hertel, G. B. & Orlando, T. P. Tunneling Study of Superconductivity near the Metal-Insulator Transition. *Phys. Rev. Lett.* **53**, 2473 (1984).

61. Miao, H. *et al.* Isotropic superconducting gaps with enhanced pairing on electron Fermi surfaces in $FeTe_{0.55}Se_{0.45}$. *Phys. Rev. B.* **85**, 094506 (2012).

62. Sharoni, A., Asulin, I., Koren, G. & Millo, O. Proximity Effect in Gold-Coated $YBa_2Ca_3O_{7-\delta}$ Films Studied by Scanning Tunneling Spectroscopy. *Phys. Rev. Lett.* **92**, 4 (2004).

63. Fujita, M., Goka, H., Yamada, K. & Matsuda, M. Competition between Charge-and Spin-Density-Wave Order and Superconductivity in $La_{1.875}Ba_{0.125-x}Sr_xCuO_4$. *Phys. Rev. Lett.* **88**.167008 (2002)

64. Abbamonte, P. *et al.* Spatially modulated 'Mottness' in $La_{2-x}Ba_xCuO_4$. *Nat. Phys.* **1**, 155–158 (2005).

65. Wu, T. *et al.* Magnetic-field-induced charge-stripe order in the high-temperature superconductor $YBa_2Cu_3O_y$. *Nature* **477**, 191–194 (2011).

66. Comin, R. *et al.* Broken translational and rotational symmetry via charge stripe order in underdoped $YBa_2Cu_3O_{6+y}$. *Science.* **347**, 1335–1339 (2015).

67. Ghiringhelli, G. *et al.* Long-range incommensurate charge fluctuations in (Y, Nd)Ba $_2Cu_3O_{6+x}$. *Science.* **337**, 821–825 (2012).

68. Kivelson, S. A. *et al.* How to detect fluctuating stripes in the high-temperature superconductors. *Rev. Mod. Phys.* **75**, 1201–1241(2003).

69. Parker, C. V. *et al.* Fluctuating stripes at the onset of the pseudogap in the high-T_c superconductor $Bi_2Sr_2CaCu_2O_{8+x}$. *Nature* **468**, 677–680 (2010).

70. Cai, P. *et al.* Visualizing the evolution from the Mott insulator to a charge-ordered insulator in lightly doped cuprates. *Nat. Phys.* **12**, 1047–1051 (2016).

71. Pan, S. H. *et al.* Microscopic electronic inhomogeneity in the high- T_c superconductor $Bi_2Sr_2CaCu_2O_{8+x}$. *Nature* **413**, 282–285 (2001).

72. McElroy, K. *et al.* Atomic-scale sources and mechanism of nanoscale electronic disorder in $Bi_2Sr_2CaCu_2O_{8+\delta}$. *Science.* **309**, 1048–1052 (2005).

73. Zeljkovic, I. *et al.* Imaging the impact of single oxygen atoms on superconducting $Bi_{2+y}Sr_{2-y}CaCu_2O_{8+x}$. *Science.* **337**, 320–323 (2012).

74. Zhou, S., Ding, H. & Wang, Z. Correlating off-Stoichiometric doping and nanoscale electronic inhomogeneity in the high-T_c superconductor $Bi_2Sr_2CaCu_2O_{8+\delta}$. *Phys. Rev. Lett.* **98**, 076401 (2007).

75. Presland, M. R., Tallon, J. L., Buckley, R. G., Liu, R. S. & Flower, N. E. General trends in oxygen stoichiometry effects on T_c in Bi and Tl superconductors. *Phys. C Supercond. its Appl.* **176**, 95–105 (1991).

76. Fujita, K. *et al.* Simultaneous transitions in cuprate momentum-space topology and electronic symmetry breaking. *Science.* **344**, 612–616 (2014).

77. Mitzi, D. B., Lombardo, L. W., Kapitulnik, A., Laderman, S. S. & Jacowitz, R. D. Growth and properties of oxygen- and ion-doped $Bi_2Sr_2CaCu_2O_{8+\delta}$ single crystals. *Phys. Rev. B* **41**, 6564–6574 (1990).

78. Zhao, H. *et al.* Charge-stripe crystal phase in an insulating cuprate. *Nat. Mater.* **18**, 103–107 (2019).

79. Ruan, W. *et al.* Relationship between the parent charge transfer gap and maximum transition temperature in cuprates. *Sci. Bull.* **61**, 1826–1832 (2016).

80. Tranquada, J. M., Buttrey, D. J., Sachan, V. & Lorenzo, J. E. Simultaneous Ordering of Holes and Spins in $La_2Ni0_{4.125}$. *Phys. Rev. Lett.* **73**, 7 (1994).

81. Mesaros, A. *et al.* Commensurate 4a0-period charge density modulations throughout the $Bi_2Sr_2CaCu_2O_{8+x}$ pseudogap regime. *Proc. Natl. Acad. Sci. U. S. A.* **113**, 12661–12666 (2016).

82. Zeljkovic, I. *et al.* Nanoscale interplay of strain and doping in a high-temperature superconductor. *Nano Lett.* **14**, 6749–6753 (2014).

83. Li, Q. *et al.* Atomically resolved spectroscopic study of Sr_2IrO_4: Experiment and theory. *Sci. Rep.* **3**, 1–7 (2013).

84. Arita, R., Kuneš, J., Kozhevnikov, A. V, Eguiluz, A. G. & Imada, M. Ab initio Studies on the Interplay between Spin-Orbit Interaction and Coulomb Correlation in Sr_2IrO_4 and Ba_2IrO_4. *Phys. Rev. Lett.* **108**. 086403 (2012)

85. Moon, S. J. *et al.* Temperature dependence of the electronic structure of the J_{eff} = 1/2 Mott insulator Sr_2IrO_4 studied by optical spectroscopy. *Phys. Rev. B.* **80**. 195110 (2009).

86. Dai, J., Calleja, E., Cao, G. & McElroy, K. Local density of states study of a spin-orbit-coupling induced Mott insulator Sr_2IrO_4. *Phys. Rev. B* **90**, 041102 (2014).

87. Kim, B. J. *et al.* Novel J_{eff} = 1/2 mott state induced by relativistic spin-orbit coupling in

Sr_2IrO_4. *Phys. Rev. Lett.* **101**, 076402 (2008).

88. Battisti, I. *et al.* Universality of pseudogap and emergent order in lightly doped Mott insulators. *Nat. Phys.* **13**, 21-25 (2017).

89. Yan, Y. J. *et al.* Electron-Doped Sr_2IrO_4: An Analogue of Hole-Doped Cuprate Superconductors Demonstrated by Scanning Tunneling Microscopy. *Phys. Rev. X*. **5**.041018 (2015).

90. de la Torre, A. *et al.* Collapse of the Mott Gap and Emergence of a Nodal Liquid in Lightly Doped Sr_2IrO_4 *Phys. Rev. Lett.* **115**, 176402 (2015).

91. Kim, Y. K. *et al.* Fermi arcs in a doped pseudospin-1/2 Heisenberg antiferromagnet. *Science.* **345**, 187–190 (2014).

92. Chen, X. *et al.* Unidirectional spin density wave state in metallic $(Sr_{1-x}La_x)_2IrO_4$. *Nat. Commun*. **9**, 103 (2018).

93. Singh, U. R., Aluru, R., Liu, Y., Lin, C. & Wahl, P. Preparation of magnetic tips for spin-polarized scanning tunneling microscopy on $Fe_{1+y}Te$. *Phys. Rev. B* **91**, 161111 (2015).

94. Kim, J. *et al.* Magnetic Excitation Spectra of Sr_2IrO_4 Probed by Resonant Inelastic X-Ray Scattering: Establishing Links to Cuprate Superconductors. *Phys. Rev. Lett*. **108**.177003 (2012).

95. Lawler, M. J. *et al.* Intra-unit-cell electronic nematicity of the high-T_c copper-oxide pseudogap states. *Nature* **466**, 347–351 (2010).

96. Enayat, M. *et al.* Real-space imaging of the atomic-scale magnetic structure of $Fe_{1+y}Te$. *Science.* **345**, 653–656 (2014).

97. Zhou, S., Jiang, K., Chen, H. & Wang, Z. Correlation Effects and Hidden Spin-Orbit Entangled Electronic Order in Parent and Electron-Doped Iridates Sr_2IrO_4. *Phys. Rev. X* **7**, 41018 (2017).

98. Zhao, L. *et al.* Evidence of an odd-parity hidden order in a spin-orbit coupled correlated iridate. *Nat. Phys.* **12**, 32–36 (2016).

99. Moon, S. J. *et al.* Dimensionality-Controlled Insulator-Metal Transition and Correlated Metallic State in *5d* Transition Metal Oxides $Sr_{n+1}Ir_nO_{3n+1}$(n = 1, 2, and ∞). *Phys. Rev. Lett.* **101**, 226402 (2008).

100. Wang, Q. *et al.* Dimensionality-controlled Mott transition and correlation effects in single-layer and bilayer perovskite iridates. *Phys. Rev. B* **87**, 245109 (2013).

101. Kim, J. W. *et al.* Dimensionality Driven Spin-Flop Transition in Layered Iridates. *Phys. Rev. Lett*. **109**. 037204 (2012).

102. Carter, J. M. & Kee, H. Y. Microscopic theory of magnetism in $Sr_3Ir_2O_7$. *Phys. Rev. B* **87**, 014433 (2013).

103. Dhital, C. *et al.* Carrier localization and electronic phase separation in a doped spin-orbit-driven Mott phase in $Sr_3(Ir_{1-x}Ru_x)_2O_7$. *Nat. Commun.* **5**, 3377 (2014).

104. Wang Z. *et al.* Disorder induced power-law gaps in an insulator-metal Mott transition.

Proc. Natl. Acad. Sci. U. S. A. **115** (44) 11198-11202 (2018).

105. Wang, Z. *et al.* Doping induced Mott collapse and possible density wave instabilities in $Sr_3(Ir_{1-x}Ru_x)_2O_7$. *npj Quantum Mater.* **4**, 43 (2019).

106. Okada, Y. *et al.* Imaging the evolution of metallic states in a correlated iridate. *Nat. Mater.* **12**, 707–713 (2013).

107. Carter, J. M., Shankar, V. V., Zeb, M. A. & Kee, H. Y. Semimetal and topological insulator in perovskite iridates. *Phys. Rev. B* **85**, 115105 (2012).

108. Wang Z. *et al.* Disorder induced power-law gaps in an insulator-metal Mott transition. *Proc. Natl. Acad. Sci. U. S. A.* **115** (44) 11198-11202 (2018).

109. Zhao, H. *et al.* Atomic-scale fragmentation and collapse of antiferromagnetic order in a doped Mott insulator. *Nat. Phys.* **15,** 1267–1272 (2019).

110. Newman, M. Power laws, Pareto distributions, and Zipf's law. *Contemp. Phys.* **46**, 323–351 (2005)

111. Liu, J. *et al.* Heterointerface engineered electronic and magnetic phases of $NdNiO_3$ thin films. *Nat. Commun.* **4**, 1–11 (2013).

112. Li, J. *et al.* Scale-invariant magnetic textures in the strongly correlated oxide $NdNiO_3$. *Nat. Commun.* **10**, 1–7 (2019).

113. Post, K. W. *et al.* Coexisting first- and second-order electronic phase transitions in a correlated oxide. *Nat. Phys.* **14**, 1056–1061 (2018).

114. Phillabaum, B., Carlson, E. W. & Dahmen, K. A. Spatial complexity due to bulk electronic nematicity in a superconducting underdoped cuprate. *Nat. Commun.* **3**, 1–8 (2012).

115. Ando, Y., Segawa, K., Komiya, S. & Lavrov, A. N. Electrical Resistivity Anisotropy from Self-Organized One Dimensionality in High-Temperature Superconductors. *Phys. Rev. Lett.* **88**, 4 (2002).

116. Hinkov, V. *et al.* Electronic liquid crystal state in the high-temperature superconductor $YBa_2Cu_3O_{6.45}$. *Science.* **319**, 597–600 (2008).

117. Chuang, T.-M. *et al.* Nematic electronic structure in the 'parent' state of the iron-based superconductor $Ca(Fe_{1-x}Co_x)_2As_2$. *Science* **327**, 181–4 (2010).

118. Chu, J.-H., Kuo, H.-H., Analytis, J. G. & Fisher, I. R. Divergent nematic susceptibility in an iron arsenide superconductor. *Science* **337**, 710–2 (2012).

119. Fernandes, R. M. & Millis, A. J. Nematicity as a Probe of Superconducting Pairing in Iron-Based Superconductors. *Phys. Rev. Lett*. **111**.127001 (2013).

120. Rosenthal, E. P. *et al.* Visualization of electron nematicity and unidirectional antiferroic fluctuations at high temperatures in NaFeAs. *Nat. Phys.* **10**, 225–232 (2014).

121. Yi, M. *et al.* Nematic Energy Scale and the Missing Electron Pocket in FeSe. *Phys. Rev. X.* **9**. 041049 (2019).

122. Johnson, P. D. *et al.* Spin-Orbit Interactions and the Nematicity Observed in the Fe-Based

Superconductors. *Phys. Rev. Lett.* 114. 167001 (2015).

123. Kasahara, S. *et al.* Electronic nematicity above the structural and superconducting transition in $BaFe_2(As_{1-x}P_x)_2$. *Nature* **486**, 382–385 (2012).

124. Ruan, W. *et al.* Visualization of the periodic modulation of Cooper pairing in a cuprate superconductor. *Nat. Phys.* **14**, 1178–1182 (2018).

125. Krüger, F., Kumar, S., Zaanen, J. & Van Den Brink, J. Spin-orbital frustrations and anomalous metallic state in iron-pnictide superconductors. *Phys. Rev. B.* **79**, 054504 (2009).

126. Chen, C. C. *et al.* Orbital order and spontaneous orthorhombicity in iron pnictides. *Phys. Rev. B* **82**, 100504 (2010).

127. Fang, C., Yao, H., Tsai, W. F., Hu, J. & Kivelson, S. A. Theory of electron nematic order in LaFeAsO. *Phys. Rev. B* **77**, 224509 (2008).

128. Fernandes, R. M. *et al.* Effects of nematic fluctuations on the elastic properties of iron arsenide superconductors. *Phys. Rev. Lett.* **105**, 157003 (2010).

129. Si, Q. & Abrahams, E. Strong correlations and magnetic frustration in the high T_c iron pnictides. *Phys. Rev. Lett.* **101**, 076401 (2008).

130. Hu, J., Xu, B., Liu, W., Hao, N. N. & Wang, Y. Unified minimum effective model of magnetic properties of iron-based superconductors. *Phys. Rev. B* **85**, 144403 (2012).

131. Mazin, I. I. & Johannes, M. D. A key role for unusual spin dynamics in ferropnictides. *Nat. Phys.* **5**, 141–146 (2009).

132. Sprau, P. O. et al. Discovery of orbital-selective Cooper pairing in FeSe. *Science* **357**, (2017).

133. Yi, M. *et al.* Observation of universal strong orbital-dependent correlation effects in iron chalcogenides. *Nat. Commun.* **6**, (2015).

134. Watson, M. D. *et al.* Emergence of the nematic electronic state in FeSe. *Phys. Rev. B* **91**, 155106 (2015).

135. Hanaguri, T. *et al.* Two distinct superconducting pairing states divided by the nematic endpoint in $FeSe_{1-x}S_x$. *Sci. Adv.* **4**, (2018).

136. Licciardello, S. *et al.* Electrical resistivity across a nematic quantum critical point. *Nature* **567**, 213–217 (2019).

137. Mizuguchi, Y. & Takano, Y. Review of Fe Chalcogenides as the Simplest Fe-Based Superconductor. *J. Phys. Soc. Japan* **79**, 102001 (2010).

138. Kuo, H.-H., Chu, J.-H., Palmstrom, J. C., Kivelson, S. A. & Fisher, I. R. Ubiquitous signatures of nematic quantum criticality in optimally doped Fe-based superconductors. *Science* **352**, 958–962 (2016).

139. Chu, J.-H. *et al.* In-plane resistivity anisotropy in an underdoped iron arsenide superconductor. *Science* **329**, 824–6 (2010).

140. Yim, C. M. *et al.* Discovery of a strain-stabilized smectic electronic order in LiFeAs. *Nat. Commun.* **9**, 2602 (2018).

141. Wang, P. S. *et al.* Robust short-range-ordered nematicity in FeSe evidenced by high-pressure NMR. *Phys. Rev. B* **96**, 094528 (2017).

142. Reiss, P. *et al.* Quenched nematic criticality and two superconducting domes in an iron-based superconductor. *Nat. Phys.* **16**, 89–94 (2020).

143. Zhang, P. *et al.* Multiple topological states in iron-based superconductors. *Nat. Phys.* **15**, 41–47 (2019).

144. Zhang, P. *et al.* Observation of topological superconductivity on the surface of an iron-based superconductor. *Science.* **360**, 182–186 (2018).

145. Kong, L. *et al.* Half-integer level shift of vortex bound states in an iron-based superconductor. *Nat. Phys.* **15**, 1181–1187 (2019).

146. Machida, T. *et al.* Zero-energy vortex bound state in the superconducting topological surface state of Fe(Se, Te). *Nat. Mater.* **18**, 811–815 (2019).

147. Wang, D. *et al.* Evidence for Majorana bound states in an iron-based superconductor. *Science* **362**, 333–335 (2018).

148. Terao, K., Kashiwagi, T., Shizu, T., Klemm, R. A. & Kadowaki, K. Superconducting and tetragonal-to-orthorhombic transitions in single crystals of $FeSe_{1-x}Te_x$ ($0 \le x \le 0.61$). *Phys. Rev. B* **100**, 224516 (2019).

149. Miao, H. *et al.* Isotropic superconducting gaps with enhanced pairing on electron Fermi surfaces in $FeTe_{0.55}Se_{0.45}$. *Phys. Rev. B* **85**, 094506 (2012).

150. Rinott, S. *et al.* Tuning across the BCS-BEC crossover in the multiband superconductor $Fe_{1+y}Se_xTe_{1-x}$: An angle-resolved photoemission study. *Sci. Adv.* **3**. 4 (2017).

151. Kostin, A. *et al.* Imaging orbital-selective quasiparticles in the Hund's metal state of FeSe. *Nat. Mater.* **17**, 869–874 (2018).

152. Gao, S. *et al.* Atomic-scale strain manipulation of a charge density wave. *Proc. Natl. Acad. Sci. U. S. A.* **115**, 6986–6990 (2018).

9 PUBLICATIONS LIST

He Zhao, Sujit Manna, Zach Porter, Xiang Chen, Andrew Uzdejczyk, Jagadeesh Moodera, Ziqiang Wang, Stephen D Wilson, Ilija Zeljkovic. Atomic-scale fragmentation and collapse of antiferromagnetic order in a doped Mott insulator. *Nat. Phys.* **15**, 1267-1272 (2019)(Chapter 5) .

He Zhao, Zheng Ren, Bryan Rachmilowitz, John Schneeloch, Ruidan Zhong, Genda Gu, Ziqiang Wang, Ilija Zeljkovic. Charge-stripe crystal phase in an insulating cuprate*, Nat. Mater.* **18**, 103-107 (2019) (Chapter 4).

He Zhao, Bryan Rachmilowitz, Zheng Ren, Robin Han, J Schneeloch, Ruidan Zhong, Genda Gu, Ziqiang Wang, Ilija Zeljkovic. Superconducting proximity effect in a topological insulator using Fe (Te, Se). *Phys. Rev. B* **97**, 224504 (2018) (Chapter 3).

Bryan Rachmilowitz*, **He Zhao***, Hong Li, Alexander LaFleur, J. Schneeloch, Ruidan Zhong, Genda Gu, Ilija Zeljkovic. Proximity-Induced Superconductivity in a Topological Crystalline Insulator. *Phys. Rev. B* **100**, 241402(R) (2019).

Shang Gao, Felix Flicker, Raman Sankar, **He Zhao**, Zheng Ren, Bryan Rachmilowitz, Sidhika Balachandar, Fangcheng Chou, Kenneth S Burch, Ziqiang Wang, Jasper Van Wezel, Ilija Zeljkovic. Atomic-scale strain manipulation of a charge density wave. *Proc. Natl. Acad. Sci.* **115**, 6986-6990 (2018).

Lianyang Dong, **He Zhao**, Ilija Zeljkovic, Stephen D Wilson, John W Harter. Bulk superconductivity in via physicochemical pumping of excess iron. *Phys. Rev. Materials* **3**, 114801(2019).

*These authors contribute equally

10 ACKNOWLEDGMENTS

This should be, without any doubt, the most important part of my thesis. I started doing my first STM project at the beginning of May 2017. In the past three years and 4 months, I finished five projects involving High-T_c superconductor family (cuprates, iron-based superconductors), topological quantum materials (Fe(Te, Se), TI/iron-based superconductor heterostructure), and spin-orbit Mott insulator (iridates), but I'm one hundred percent sure none of them can be done without the support from a group of great people.

First and foremost, I'd like to thank my advisor, Ilija Zeljkovic. I'm honored to be his first Ph.D. student and going to be his first postdoc. I learned so much from him in the past five years, including not only how to do excellent research in the lab but also personal development outside. It's you introduced me to the STM community and taught me all the experimental skills from taking the top-level data, doing analysis to finally writing a paper, and presenting the result. Even two years passed, I still clearly remember how excited I was when Ilija emailed me that our group's first top-level work—charge stripe on cuprate paper published on Nature Materials. As every experimental colleague knows, 99% of the time in the research is not so exciting, maybe even boring when scanning samples with no intrinsic interesting properties. But every time I want to give up on a seemingly hopeless project, Ilija just kept encouraging me to be more patient and step forward, and we finally figured out the nematicity on Fe(Te, Se), the longest project expanding over three years, which is under review when I'm writing this chapter. Hope for the best! And you always remind me not to struggle too much to be perfect on everything but just focus on the few staff that matter. Our discussions about physics, decision making, personal career development will definitely be an unforgettable experience for me.

I would like to express my sincere gratitude to my lab colleagues, it's a real pleasure to be part of this team. Bryan Rachmilowitz, who is always generous to give me a hand. Without your help in cutting the cleaving rod, our sample preparation would be more time consuming and boring. And we used to have a perfect collaboration in timing: you came to the lab at very early morning to grow the sample, while I always woke up late in the noon and transferred the prepared sample into STM and scanned. We usually talk about some political and cultural difference between China and America, I'm sure that both of us enjoyed the chatting and learned more about each other's country. And thanks Zheng Ren, my roommate in the past three years as well, we used to play basketball with Xu Yang, Lidong Ma, and Shenghan Jiang for fun and that helps me away from heavy lab work for a short time. We used to work on the thin film FeSe/STO, though no exciting result came out back then, I'm glad to see the partial phase separation between strain and nematicity project finally submitted. Thanks, Sujit Manna, though you're not

officially our postdoc, we became a friend during our single layered iridates project. I mastered the spin-polarized STM technique from zero under his patient teaching. We used to eat lunch together and share our personal experience, and your optimism and endless encouragement help me out when my feeling disappointed about the measurements. For the younger members, thanks to Hong Li for bearing my being impatient when teaching you STM, and without your hard work on scanning samples during my annual vacation, our Fe(Te, Se) project progress would be much slower. And of course all other members of Zeljkovic lab: Alexander LaFleur, Nastaran Alamgir Tehrani, and Shrinkhala Sharmaa, it's you told me that professor is a high salary job in India. Also thanks to our former undergraduate students: Andrew Uzdejczyk, for your helping etch the spin-polarized tips, Hanyi Lu, for your introducing American party culture to me, Justin Joss, for your standing on hand show, Noah Barnett, for your hilarious movement in the lab, Nicholas Stubblefield, for your copying the former guy's movement, Maxwell Lavey for your smile and Tia Qiying Lim for your teaching me how to play squash four years ago and it has been one of my favorite sports now and hopefully we can play for a real game someday.

Thanks for all the professors in the Boston College physics department. Kenneth Burch, thanks for admitting me into the physics department 6 years ago, though we didn't work together due to my eye health issue, you opened the fascinating world of experimental physics. Prof. Pradip Bakshi, Prof. David Broido, Prof. Gabor, J. Kalman, Prof. Ying Ran, and Prof. Fazel Tafti, thanks for your teaching us physics in the class. Thanks, Prof. Michael Graf for being my committee member. Thanks for Prof. Brian B Zhou sharing your postdoc application experience with me, which helps reduce my anxiety a lot. Many thanks to Prof. Ziqiang Wang, for your patience when we asked some naïve questions related to theory, and your deep knowledge and enthusiasm for strongly correlated electron systems excellently placed our measurement results into the right perspective. I heard from Kun Jiang that you are professional in playing table tennis, maybe someday we can have a game.

Thanks our department office staff, Jane Carter, for reminding me to clean my office when I mess it up, Nancy Chevry, Sile Ni Scanlain, and Scott Bortolotto. You provide the best working environment for our international students from outside the lab. With your effort, our department cannot run so smoothly.

Many thanks to all my colleagues in the BC physics department, who all contribute to making my life more colorful in many different ways. Our graduate students, Kun Jiang, Sheng Han, Mengliang Yao, and Xueyuan Wu, thanks for your driving me for lunch and dinner, teaching me the life-work balance in my early time in BC. Yiping Wang, Lidong Ma, Xu Yang, Xiaodong Hu, Yiqiu Han, Faranak Bahrami, Tyler Dodge, Mark Schiller, Victoria Gabriele, Mason Gray, Gavin Osterhoudt, Vincent Plisson, and Joshuah Heath thanks for your accompany. Thanks, Juan Merlo for your sharing me about the culture of Mexico and encouraging me to keep moving. Thanks, Jiantao Kong for bearing my

bothering whenever I want to find a friend to chat to beat the boring time, especially in this difficult year.

Thanks, John O' Grady, Fabia Denaro, Moira Smith, Kiel Smith, Chris Cardoso, and Walter, for your help in running our lab efficiently without worrying about ordering liquid nitrogen, helium, delivery of the shipment, and lab/office cleaning. Richard Pijar, thanks for making our etching circuit back to work whenever there is some wire burning.

I want to give my gratitude to my friends outside BC. Thanks, Yao Tian, who used to give me instruction when I was in Burch's lab and our friendship continues after you leaving. Thanks for sharing those funny videos and emoji. Many thanks for my high school classmates and also my friend, Haojie Jiao, for your constant spiritual support, sharing your life off work, introducing your friends to me, and encouraging me to find work-life balance, which is always hard for me if I want to gain something. My friend Yao Song, thanks for your treating me when I traveled to California and the travel with your five days full-time driving in Yellowstone national park helped me deiced to get my driver's license after coming back to Boston. 'Quick fall asleep in the car, but pee immediately after getting off' is one of the funniest experiences in my past 6 years. Thanks Jian Wang, a nontypical but versatile theorist, for your enthusiasm for research and life. Wenping Cui, whom I spent long free time with outside the lab (I'm glad that your girlfriend doesn't get me wrong), thanks for your patience on playing squash with me. Thanks for bearing me always arriving late for our games. I miss those days you lost to me with 0-20. Let's pick up the rackets after the COVID period passed. Congratulations to you and your girlfriend will have a baby in a few months. Only treat me more free meals can help me feel better with those jokes you played about my being single (I'm kidding~). Stay safe and healthy.

Last but not the least, I want to express the heartfelt thanks to my family members and close friends. My uncle, though with no blood relationship, Shifang Liu, thanks for treating my cousin and me lunches and dinners on Chinese conventional festivals which makes us feel at home. My uncle, Desheng Liu, a professor but in a different field than me, thanks for your consistent support on the turning-point of my life since I was a child. In the past three years, one of my hardworking driving forces is to share with you the progress of our project. My cousin, Wencong Liu, thanks for your constant assistance in my life and your sharing funny videos of my nephew, Chengyuan Liu. Finally, I wanna give thanks to my parents, Chaomin Zhao, Dejuan Liu, for your upbringing. Video chat and sharing my daily life in America with you help me through countless sleepless nights.

Thank you all!